

# Pattern Formation in a New Class of Precipitation Reactions

THÈSE

présentée à la Faculté des sciences de l'Université de Genève  
pour obtenir le grade de Docteur ès Sciences, mention physique

par

**Péter HANTZ**  
de  
Cluj/Kolozsvár (Roumanie)

Thèse N°. 3747

GENÈVE  
Atelier de reproduction de la Section de physique  
2006





**UNIVERSITÉ  
DE GENÈVE**

FACULTÉ DES SCIENCES

**Doctorat ès sciences  
mention physique**

Thèse de *Monsieur Péter HANTZ*

intitulée :

**" Pattern Formation in a New Class of Precipitation Reactions "**

La Faculté des sciences, sur le préavis de Messieurs M. DROZ, professeur titulaire et directeur de thèse (Département de physique théorique), X. CHILLIER, docteur (Département de chimie physique), et Madame F. BARAS, docteur (Université de Bourgogne – Centre National de la Recherche Scientifique UMR 5613 – Laboratoire de recherche sur la réactivité des solides – Dijon, France), autorise l'impression de la présente thèse, sans exprimer d'opinion sur les propositions qui y sont énoncées.

Genève, le 9 juin 2006

**Thèse - 3747 -**

**Le Doyen, Pierre SPIERER**

N.B.- La thèse doit porter la déclaration précédente et remplir les conditions énumérées dans les "Informations relatives aux thèses de doctorat à l'Université de Genève".

Nombre d'exemplaires à livrer par colis séparé à la Faculté : - 7 -

## Acknowledgements

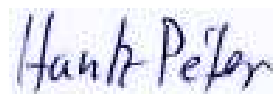
I am indebted to a large group of scientists and sponsors who helped me during the PhD process.

First of all I would like to acknowledge the support of my supervisor, Professor **Zoltán Rácz**, and that of Professor **Michel Droz** who made me possible to defend my thesis at the University of Geneva. I also got a substantial amount of help from Szilárd András, Markus Antonietti, Gyula Bene, Ágnes Buka, Efim Brener, András Büki, Ferenc Csikor, Michael C. Cross, Gyula Dávid, Ben De Lacy Costello, Peter Dobson, Michel Droz, Kati Evans, Gyula Faigel, Vincent Fleury, István Forgács, András Kristóf Fülöp, Stoyan Gisbert, Pierre-Gilles de Gennes, László Gránásy, Géza Györgyi, Zsuzsa Hódi, Szabolcs Horvát, Dezső Horváth, Zoltán György Horváth, Zalán Horváth, Zoltán Hórvölgyi, László Hunyadvári, Thomas Ihle, György Inzelt, István Jalsovszky, David Juncker, Mads Kaern, Tibor Kalapos, János Kertész, Ernő Keszei, György Kéri, Ádám Kiss, István Zoltán Kiss, Katharina Krisher, Margit Koós, Tamás Kovács, Endre Kőrös<sup>†</sup>, Zoltán Kristóf, Győző Láng, Xiang-Yang Liu, Zsófia Maglóczky, Attila Magyar, András Málnási-Csizmadia, Nicholas R. Moloney, Alexander Nepomnyashchy, Zoltán Noszticziusz, Gabriella Nettig, Hans Meinhardt, Imre Oláh, Miklós Orbán, Julian Partridge, Tamás Perger, József Rábay, Miklós Sass, László Sasvári, Răzvan Satnoianu, István Scheuring, Friedmann Schneider, Kenneth Showalter, Péter Simon, Péter Somogyi, Eörs Szathmáry, Emese Noémi Szász, László Szilágyi, Kálmán Szabó, Péter Tasnádi, Tamás Turányi, Tamás Tél, Géza Tichy, Katalin Tóth, Ida Tóth, Anita Varga, Vladimir Vanag, Géza Zboray.

I thank the support of grant OTKA T029792, OTKA T038071, OTKA T037588, NKFP 3A/0036/2002, Sapientia-KPI Foundation, Domus Hungarica Foundation of the Hungarian Academy of Sciences, Agora Foundation, ESF Reactor Programme, Ösztöndíj Foundation, Orbán Balázs Foundation, Hungarian Ministry of Education, György Kéri, Tamás Kornay, György Marosi and Eörs Szathmáry.

Last but not least I thank the help of my family and my friends.

Péter HANTZ



# Contents

<b>1</b>	<b>Résumé</b>	<b>vii</b>
<b>2</b>	<b>Introduction</b>	<b>1</b>
2.1	Reaction-diffusion Patterns in Active Media . . . . .	1
2.1.1	Classification . . . . .	2
	Linear Stability Analysis . . . . .	2
	Oscillating Chemical Reactions . . . . .	4
	Turing Mechanism . . . . .	9
	Packet Waves and Standing Waves . . . . .	11
2.1.2	Traveling Fronts, Pulses and Wavetrains . . . . .	12
	Fronts in Multistationary Media . . . . .	13
	Pulses and Wavetrains in Excitable Media . . . . .	17
	Wavetrains in Oscillatory Media . . . . .	20
2.2	Precipitation and Solidification Processes . . . . .	21
2.2.1	The Liesegang Phenomenon . . . . .	21
	Supersaturation Theories . . . . .	23
	Sol Coagulation Theories . . . . .	25
	Phase Separation Theories . . . . .	29
2.2.2	Dendritic and Seaweed Solidification . . . . .	30
2.3	Other Growth Processes . . . . .	33
2.4	Sea Shell Patterns . . . . .	34
<b>3</b>	<b>Experimental Investigation of Primary Patterns</b>	<b>37</b>
3.1	Preparation of the Experiments . . . . .	37
3.1.1	Sample Preparation . . . . .	37
	The PVA Gel . . . . .	37
	The Agarose Gel . . . . .	37
3.1.2	The Experimental Setup . . . . .	38
3.2	Formation of Primary Patterns in Gel Sheets . . . . .	40
3.2.1	The Sequence of Pattern Formation . . . . .	40
3.2.2	A Qualitative Explanation . . . . .	44
3.2.3	Experimental Results Supporting the Qualitative Explanation . . . . .	45
	Ion-selectivity of the Passive Borders . . . . .	47

---

	Microspectrophotometric Measurements . . . . .	50
	Other Experimental Findings . . . . .	52
3.3	Formation of Primary Patterns in Gel Columns . . . . .	53
3.3.1	Rhythmic Banding . . . . .	54
3.3.2	Homogeneous Precipitation . . . . .	55
3.3.3	Helicoids, Spirals . . . . .	55
3.3.4	Cardioid-like Patterns . . . . .	57
3.3.5	Target-like Patterns . . . . .	58
3.3.6	Cabbage-like Patterns . . . . .	60
3.4	Voronoi Diagrams . . . . .	61
3.4.1	Concept and Generation of Voronoi Diagrams . . . . .	61
3.4.2	Voronoi Diagrams Generated by Regressing Edges of Precipitation Fronts . . . . .	62
<b>4</b>	<b>Primary Patterns: Theory and Computer Simulations</b>	<b>65</b>
4.1	The Mathematical Model . . . . .	65
4.2	Simulation Results . . . . .	68
4.2.1	Digression: The Chemical Needle Effect . . . . .	69
4.3	Discussion and Open Questions . . . . .	72
<b>5</b>	<b>Secondary Patterns: Experiments and a Hypothesis</b>	<b>73</b>
5.1	The Scenario of the Formation of Secondary Patterns . . . . .	73
5.2	Defects in the Secondary Patterns . . . . .	78
5.3	Oblique Striping . . . . .	78
5.4	Experiments in Gel Columns . . . . .	79
5.5	Hypothesis and Computer Simulations . . . . .	81
5.5.1	Modeling the pattern formation in the wake of source fronts . . .	82
5.5.2	Simulation results: source fronts traveling with constant speed . .	83
5.5.3	Rotating source fronts . . . . .	85
5.5.4	Studies on Quenching Fronts . . . . .	86
5.6	Conclusions . . . . .	89
<b>6</b>	<b>Afterword</b>	<b>91</b>
6.1	Publications . . . . .	91
6.2	Perspectives for Further Research . . . . .	91
	<b>Index</b>	<b>92</b>
	<b>Bibliography</b>	<b>93</b>

# Chapter 1

## Résumé

### Formation de structures dans une nouvelle classe de réactions de précipitation

En étudiant le phénomène de Liesegang, j'ai observé un comportement inhabituel pour la réaction  $NaOH$  (l'électrolyte extérieur) +  $CuCl_2$  (l'électrolyte intérieur) dans un gel de polyvinylalcool (PVA). Au lieu de la formation attendue d'une structure lamellaire de type Liesegang, des structures très étranges sont apparues, nommées "structures en choux" [13]. L'étude systématique des réactions  $NaOH + CuCl_2$  dans du PVA et du gel d'agarose ainsi que l'étude de réactions telles que  $NaOH + Cu(NO_3)_2$ ,  $NaOH + AgNO_3$  [157], et  $CoCl_2 + K_3[Fe(Cn)_6]$ ,  $CuCl_2 + K_3[Fe(Cn)_6]$  [159], montrant des caractéristiques similaires, m'ont conduit à conclure que j'avais découvert une nouvelle classe de réactions chimiques "non-linéaires" formant des structures.

Les expériences dans ce domaine peuvent être conduites dans des géométries similaires à celles utilisées dans l'étude des structures de Liesegang. Les expériences ont été réalisées soit dans des gels de type PVA soit dans des gels d'agarose. Ces gels neutres, sont d'un emploi facile et leurs réticulations ne font pas appel à d'autres composés chimiques qui pourraient perturber les réactions de précipitation. L'électrolyte extérieur est déposé sur une feuille ou dans une colonne de gel qui contient l'électrolyte intérieur; une grande variété de structures peuvent se former dans le sillage du front de diffusion de l'électrolyte extérieur. Les structures qui résultent de ces réactions peuvent être divisées en deux classes principales: les structures primaires et les structures secondaires.

Les *structures primaires* (les plus simples) sont formées lorsque les réactions se déroulent dans des feuilles de gel. Leurs formes élémentaires sont constituées de régions trapézoïdales de précipité. Ces structures présentent deux types de surfaces limitrophes. La précipitation a lieu seulement sur les *bordures actives* tandis qu'aucun processus chimique n'a lieu le long des *bordures passives*. Nos expériences ont démontré que les bordures passives sont semi-perméables et limitent la diffusion de l'ion réactif contenu dans l'électrolyte extérieur. Lorsque ce dernier traverse les bordures actives, il va rencontrer et réagir avec l'électrolyte intérieur seulement à l'avant des bordures actives.

Nous avons aussi découvert que les réactions conduisent initialement à un composé intermédiaire diffusif (DC). Un des aspects les plus significatifs du modèle est l'apparition

d'une concentration critique, ou *seuil de croissance*, du composé intermédiaire diffusif, nécessaire pour qu'une précipitation continue puisse se développer [158, 161]. En raison de la semi-perméabilité des bordures passives, le composé intermédiaire diffusif sera présent essentiellement à l'avant des bordures actives. Si le seuil de croissance n'est pas atteint sur une portion du front de précipitation avant un certain temps  $\tau$  depuis de sa formation, on suppose que la portion de bordure active perd sa perméabilité et devient passive. Puisque la vitesse du front de précipitation diminue avec le temps, une valeur constante de  $\tau$  impliquerait que celui-ci s'arrêtera après un temps fini. Cependant, les résultats expérimentaux suggèrent qu'en ayant une concentration constante de l'électrolyte extérieur, on obtient une propagation du front durant un temps arbitrairement long [157]. Un tel comportement peut être reproduit par notre modèle en supposant que  $\tau = \tau(v)$  augmente lorsque la vitesse  $v$  du front diminue.

Dans le cas le plus simple, quand les réactions se déroulent dans des feuilles de gel minces, les caractéristiques qualitatives les plus importantes de la formation des structures primaires sont la contraction des segments des bordures actives qui laissent derrière elles une zone de précipité de forme trapézoïdale, zone qui à son tour évolue vers un triangle de précipité [157, 158, 161]. Pour expliquer ce comportement, nous avons supposé que la concentration du composé intermédiaire diffusif n'atteint pas le seuil de croissance autour des points extrêmes des segments de la bordure active durant le temps  $\tau(v)$ . Des simulations numériques ont démontré que cette situation est générique. L'apparition de bords des zones actives en mouvement est attribuée au fait que la concentration du composé intermédiaire diffusif est supérieure au seuil de nucléation qui, lui, est supposé être supérieur au seuil de croissance [166]. L'explication qualitative donnée ci-dessus est corroborée par plusieurs faits expérimentaux obtenus dans le cadre de diverses conditions expérimentales. Les observations les plus importantes sont les suivantes:

1. Un phénomène intéressant a lieu lorsqu'un front de précipitation, se déplaçant le long d'une bordure passive, atteint le sommet d'un triangle de précipité. Les figures 1.1 (b.) and (f.) représentent la situation où une des marges du front se déplace le long d'une zone de précipité. La bordure passive du précipité formé auparavant est supposée agir comme un obstacle dans lequel le composé intermédiaire diffusif ne peut pas pénétrer. Alors, la concentration du composé intermédiaire diffusif n'est pas diminuée sur cette marge du front. Lorsque le front approche le sommet du triangle de précipité, le composé intermédiaire diffusif au voisinage de la fin du front commence à diffuser dans un espace beaucoup plus grand que précédemment. Il en résulte que sa concentration diminuera. Si elle descend en dessous de la concentration critique requise pour la progression de la bordure active, pendant des temps supérieurs à  $\tau$ , alors le point extrême du front de précipitation peut devenir "ion-sélectif" et une transition "active-passive" peut alors avoir lieu (figs. 1.1 (c.) and (g.)). Plus tard, la portion de la bordure qui est toujours active va se contracter et évoluer de la manière décrite plus haut. Un scénario identique peut avoir lieu lorsqu'un front de précipité passe à travers un obstacle ayant des bords acérés.



2. Lorsqu'un segment d'un front de précipité rencontre un obstacle, tel une bulle d'air ou une esquille de verre de taille de l'ordre d'environ  $0.1 - 1 \text{ mm}$ , la vitesse de cette portion de front croît jusqu'à ce qu'elle touche la barrière (fig. 1.1 (h.)). L'accélération débute lorsque le front se trouve à environ  $60 \mu\text{m}$  de l'obstacle. Si le composé intermédiaire diffusif ne peut pas passer à travers la barrière, sa concentration peut croître entre l'obstacle et le front. Une plus grande concentration du composé intermédiaire diffusif est la raison la plus probable pour expliquer les plus grandes vitesses du front de précipité.

Comme déjà mentionné, la transition active-passive peut prendre place lorsque le front de précipité passe à travers un obstacle. Il en résulte que la bordure active se divise en deux segments.

3. Lorsque deux fronts de précipité se rencontrent et fusionnent, la vitesse du front résultante est fortement augmentée au voisinage du point de rencontre (fig. 1.1 (i.)). Cette accélération résulte des deux bordures actives possédant, devant elles, des régions riches en composé intermédiaire diffusif. Dans le voisinage immédiat de ces points, ces régions se recouvrent et donc la concentration du composé intermédiaire diffusif augmente. Les fronts sont supposés avoir une vitesse plus grande lorsqu'ils balayent de telles régions. Notons encore que la concavité du front engendre aussi une augmentation de sa vitesse.

Dans la réaction  $\text{NaOH} + \text{AgNO}_3$  le précipité ne redémarre pas à l'avant des bordures passives, alors que dans le système  $\text{NaOH} + \text{CuCl}_2$ , le redémarrage du précipité est aussi retardé. Dû au fait que dans ces systèmes le radical  $\text{OH}^-$  est le ion réactif de l'électrolyte extérieur, il est alors légitime de supposer que la précipitation s'arrête parce que les bordures passives bloquent le passage des ions  $\text{OH}^-$ . Pour confirmer cette hypothèse, des mesures de  $pH$  ont été effectuées des deux côtés des bordures passives environ  $14 \text{ h}$  après l'arrêt de la réaction. Comme le  $pH$  ne s'égalisa pas durant cette période, il est raisonnable de supposer que les bordures passives ralentissent de manière significative la diffusion des ions déterminant le  $pH$ . Des mesures similaires faites pour la réaction  $\text{NaOH} + \text{CuCl}_2$ , 4 heures après la formation de bordures passives, ont conduit à des conclusions similaires. Il est également plausible de supposer que dans le système  $\text{CuCl}_2 + \text{K}_3[\text{Fe}(\text{CN})_6]$ , le passage des ions cuivre est prohibé par les bordures passives (hypothèse soutenue par des observations visuelles). Cependant, il n'est actuellement pas clair si les bordures passives sont des membranes totalement isolantes ou provoquent une diffusion restreinte pour certains ions seulement. Les réponses à de telles questions peuvent être apportées par des mesures de résistance (ou de conductance) de segments appropriés de gel pour lesquels toute la section est formée par une bordure passive. Une haute résistance caractérise une membrane totalement isolante alors qu'une faible résistance indique que certains ions peuvent toujours traverser la bordure passive.

Nos mesures électrochimiques ont montré que les parties réelles des impédances étaient toujours relativement petites ( $< 7 \Omega$ ), et les valeurs mesurées à  $f = 10 \text{ kHz}$  et  $f = 788.5 \text{ Hz}$ , qui peuvent être univoquement identifiées avec la résistance de la

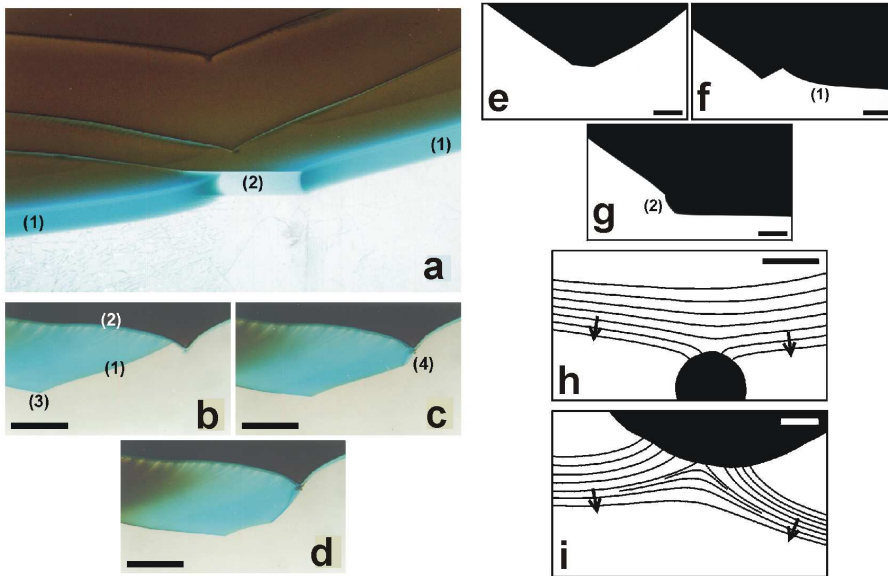


Figure 1.1: Expériences corroborant le modèle phénoménologique. (a.) Bordures active (1) et passive (2) pour le système  $NaOH + CuCl_2$  dans un gel de type PVA, vu d'une direction oblique. On notera la différence des opalescences des couleurs. La feuille de gel, d'une épaisseur de  $1.6\text{ mm}$  est située entre deux plaques de verre.  $a_0 = 8\text{ M NaOH}$ ,  $b_0 = 0.732\text{ M CuCl}_2$ . (b.)-(d.) Transition active-passive dans le système  $NaOH + CuCl_2$ . La réaction a lieu dans une feuille de gel d'agarose d'une épaisseur de  $1.6\text{ mm}$ , située entre deux plaques de verre.  $a_0 = 4\text{ M NaOH}$ ,  $b_0 = 0.586\text{ M CuCl}_2$ , l'étalon a une longueur de  $2\text{ mm}$ . Les figures (c.) et (d.) représentent la situation à  $871\text{ s}$  et à  $1398\text{ s}$  respectivement après celle de la figure (b.). La bordure active (1) est limitée d'un côté par la bordure passive de précipité formé précédemment (2), et de l'autre côté, par un bord régressif (3), point de rencontre des bordures active et passive du nouveau précipité [figure (b.)]. Lorsque la bordure active atteint le sommet du triangle de précipité, une nouvelle bordure passive va apparaître [figure (c.)]. Le front de précipité devient entouré par deux bords régressifs et va donc se contracter [figure (d.)], puis finalement disparaître. Notons la décroissance du précipité bleu-vert dans le précipité brun. (e.)-(g.) Transition active-passive dans le système  $NaOH + AgNO_3$ . La réaction a lieu dans un gel de type PVA situé entre une lame de microscope et un verre recouvrant.  $a_0 = 8\text{ M NaOH}$ ,  $b_0 = 0.412\text{ M AgNO}_3$ , l'étalon a une longueur de  $0.5\text{ mm}$ . Les figures (f.) et (g.) ont été prises à des temps de  $552\text{ s}$  et  $672\text{ s}$  respectivement après la figure (e.). La figure (e.) montre une bordure active se rétrécissant, laissant derrière elle une région de précipité de forme trapézoïdale. La figure (f.) montre une bordure active qui s'approche du sommet du triangle de précipité formé au cours du scénario précédent. Lorsqu'elle atteint le sommet, une transition active-passive a lieu et une nouvelle bordure passive apparaît (2) [figure (g.)]. (h.) Accélération d'un segment de front de précipité rencontrant un obstacle. La réaction a lieu dans un gel de type PVA entre une lame de microscope et un verre couvrant. Les lignes noires représentent le front de précipité à des intervalles de  $30\text{ s}$ , et la région noire représente l'obstacle. Les flèches indiquent la direction du front de précipitation.  $a_0 = 8\text{ M NaOH}$ ,  $b_0 = 0.732\text{ M CuCl}_2$ , et la longueur de l'étalon est  $150\text{ }\mu\text{m}$ . (i.) Fusion des fronts de précipitation dans le système  $NaOH + CuCl_2$ . La réaction a lieu dans un gel de type PVA entre une lame de microscope et un verre couvrant. Les lignes noires décrivent le front de précipité à des intervalles de  $30\text{ s}$ , excepté pour les deux petites courbes au milieu. Ces petites courbes indiquent la position du front fusionné,  $5$  et  $15\text{ s}$  après que les derniers des segments non connectés du front aient été tracés.  $a_0 = 8\text{ M NaOH}$ ,  $b_0 = 0.732\text{ M CuCl}_2$ , et l'étalon a une longueur de  $150\text{ }\mu\text{m}$ .

solution et de la phase précipité-gel entre les électrodes de référence, sont pratiquement indépendantes du temps durant l'évolution de la structure précipitée dans le gel. Des résultats similaires ont été obtenus pour le système  $NaOH + AgNO_3$ . En conséquence, nous en concluons que les bordures passives ne sont pas complètement isolantes, mais possèdent des propriétés sélectives pour les ions.

Quand la réaction  $NaOH + CuCl_2$  se déroule dans un gel PVA placé dans des tubes à essai et des boîtes de Petri, on observe la formation d'une structure lamellaire de Liesegang irrégulière, qui peut être de types cible, cardioïdale, spirale rotative et, aux concentrations plus élevées, une structure en choux irrégulière.

Les précipités formés dans les réactions  $NaOH + AgNO_3$  et  $CuCl_2 + K_3[Fe(CN)_6]$  qui ont lieu dans des boîtes de Petri peuvent mener à un diagramme de Voronoi. On rappelle qu'un diagramme de Voronoi planaire est donné par la carte des plus proches voisins pour un ensemble initial de points donnés.

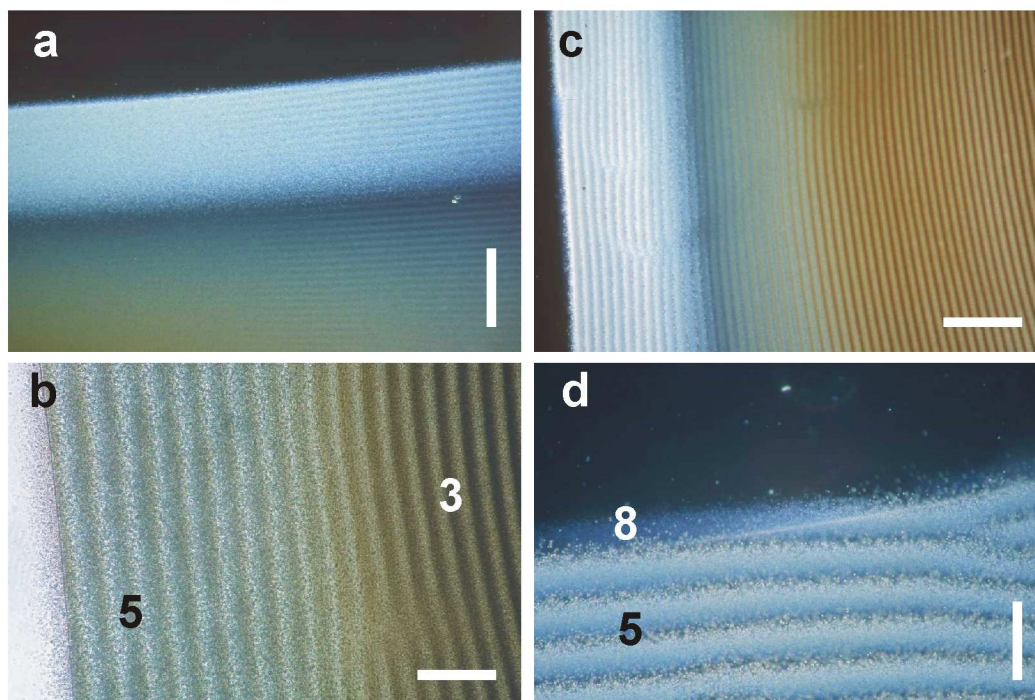


Figure 1.2: (a.) Examen sur fond noir de la structure juste après l'apparition du précipité colloïdal. L'étalon a une longueur de  $200 \mu m$ . (b.) Deux étapes importantes dans la formation des bandes de précipité. Le précipité colloïdal (5) se forme à l'avant de la bordure active et se transforme en un précipité de couleur brune (3). L'étalon est de  $100 \mu m$ . (c.) Structures similaires en examen sur fond noir. L'étalon a une longueur  $200 \mu m$ . (d.) Examen sur fond noir de la formation des bandes. Tout d'abord, une impureté de petite taille se forme (8) qui se développe pour former un gros grain colloïdal. L'étalon a une longueur  $100 \mu m$ .  $a_0 = 8.0 M NaOH$ ,  $b_0 = 0.732 M CuCl_2$ .

Notons que le composé qui forme les structures primaires n'est pas identifiable au

microscope optique. Des réactions telles que  $NaOH + CuCl_2$  et  $NaOH + AgNO_3$  dans un gel PVA peuvent également conduire à des structures microscopiques régulières [160]. Dans le cas du processus  $NaOH + CuCl_2$ , quand la vitesse d'une bordure active est inférieure à  $0,8 \mu m/s$  environ, un précipité colloïdal d'aspect granulaire, distribué de manière homogène, se forme à l'avant de la bordure active.

Quand la vitesse est encore plus faible, la formation de ce colloïde devient discontinue, formant des *structures secondaires* composées par des couches presque équidistantes. Ceci est très différent de la formation d'une structure lamellaire de type Liesegang. La longueur d'onde de ces structures régulières peut être aussi petite que  $20 \mu m$  et ces structures peuvent agir comme une grille optique. Les structures secondaires formées dans la réaction  $NaOH + AgNO_3$  peuvent avoir une longueur d'onde encore bien plus petite.

Les structures secondaires, formées par des bandes de particules colloïdales, ne sont pas sans défauts. Un aspect dynamique intéressant de la réaction est l'apparition des défauts qui interagissent entre eux. Ils apparaissent généralement lorsqu'il y a une légère différence de vitesses entre certaines parties de la bordure active. Bien que la longueur d'onde des structures dépende de la vitesse de progression des bordures actives, dans la majorité des cas les différences ne sont pas suffisantes pour générer des modifications significatives de la longueur d'onde de la grille. Toutefois, la partie du front ayant une vitesse supérieure, produit plus de bandes de précipité que la partie avec une plus petite vitesse. Si la longueur d'onde est approximativement constante, toutes les bandes ne peuvent pas être continues le long de la bordure active. A l'endroit du front ayant la plus grande vitesse, de nouvelles bandes sont insérées, et des défauts interstitiels de type fourche sont créés.

La formation des structures primaires a été modélisée en combinant une approche de type automate cellulaire à une approche de type équations de réaction-diffusion. La partie automate cellulaire modélise les phénomènes ayant lieu à une échelle plus petite que celle pertinente pour le phénomène de réaction-diffusion.

Les caractéristiques qualitatives les plus importantes des structures primaires ont été reproduites par simulations numériques [162]. Les équations ainsi que les règles d'automate cellulaire du modèle sous forme adimensionnelle sont les suivantes:

$$\begin{aligned} \frac{\partial a(x, y, t)}{\partial t} &= D_a(x, y) \cdot \Delta a(x, y, t) - r \cdot a(x, y, t) \cdot b(x, y, t) \\ \frac{\partial b(x, y, t)}{\partial t} &= D_b(x, y) \cdot \Delta b(x, y, t) - r \cdot a(x, y, t) \cdot b(x, y, t) \\ \frac{\partial c(x, y, t)}{\partial t} &= D_c(x, y) \cdot \Delta c(x, y, t) + r \cdot a(x, y, t) \cdot b(x, y, t) - [R] \end{aligned}$$

- 
- R0:  $[c(x, y, t) > c^{**}] \wedge [d(x, y, t) = \text{vide}] \rightarrow d(x, y, t + \Delta t) = \text{bordure active}$
- R1:  $[c(x, y, t) > c^*] \wedge [d(x, y, t) = \text{bordure active}] \wedge [d(x_{nn}, y_{nn}, t) = \text{vide}] \rightarrow$   
 $\rightarrow [d(x_{nn}, y_{nn}, t + \Delta t) = \text{bordure active}] \wedge [d(x, y, t + \Delta t) = \text{précipité volumique}] \wedge$   
 $[c(x, y, t + \Delta t) = 0]$
- R2:  $[c(x, y, t) < c^*] \wedge [d(x, y, t) = \text{bordure active}] \wedge [T(x, y, t) \leq \tau(v)] \rightarrow$   
 $\rightarrow T(x, y, t + \Delta t) = T(x, y, t) + \Delta t$
- R3:  $[c(x, y, t) < c^*] \wedge [d(x, y, t) = \text{bordure active}] \wedge [T(x, y, t) > \tau(v)] \rightarrow$   
 $\rightarrow d(x, y, t + \Delta t) = \text{bordure passive}$
- R4:  $[d(x, y, t) = \text{bordure active}] \wedge [d(x_{nn}, y_{nn}, t) = \text{non vide} \forall (x_{nn}, y_{nn})] \rightarrow$   
 $\rightarrow d(x, y, t + \Delta t) = \text{précipité volumique}$

$$D_a(x, y) = \begin{cases} 0, & \text{si } d(x, y) = \text{bordure passive ou obstacle} \\ D_a & \text{autrement} \end{cases}$$

$$D_{b,c}(x, y) = \begin{cases} 0, & \text{si } d(x, y) = \text{non vide} \\ D_{b,c} & \text{autrement} \end{cases}$$

Les coordonnées  $x$  and  $y$  localisent un point de la couche de gel.  $t$  est le temps et  $\Delta t$  est le pas d'intégration. Les termes  $a(x, y, t)$  et  $b(x, y, t)$  représentent les densités des ions en interactions pour, respectivement, l'électrolyte extérieur et intérieur;  $c(x, y, t)$  décrit le composé intermédiaire qui diffuse;  $c^{**}$  est le seuil de nucléation alors que  $c^*$  correspond au seuil de croissance. Le couplage avec les règles d'automate est donné par les règles  $[R]$ . Le terme  $d(x, y, t)$  décrit le précipité et n'est pas relié à une concentration. Il prend un nombre discret de valeurs, identifiant le précipité de volume, les bordures actives ou passives, ainsi que les régions sans précipité. Les obstacles sont des sites inertes dans lesquels aucun des composants ne peut entrer par diffusion.  $T(x, y, t)$  représente l'âge alors que  $\tau(v)$  décrit le temps de vie maximum d'une cellule.  $v$  est la vitesse du front de précipitation. En général, le temps de vie maximum est supposé dépendre de  $v$ . Les sites plus proche voisins du point  $(x, y)$  sont dénotés par  $(x_{nn}, y_{nn})$ . Le symbole ' $\wedge$ ' représente la fonction logique "et".

Initialement, seul le composé  $b$  de concentration initiale  $b_0$ , et quelques obstacles inertes sont présents. Le composé  $a$  a une concentration  $a_0$  le long du bord  $x = 0$ . Les conditions aux bords sont telles que les flux sont nuls sur les autres bords du champ de réaction. Le Laplacien entrant dans le terme de diffusion est noté  $\Delta$  alors que les coefficients de diffusion des composés respectifs sont  $D_a$ ,  $D_b$ , et  $D_c$ . Dans notre modèle, le coefficient de diffusion de l'électrolyte extérieur est nul sur les bordures passives, ce qui veut dire qu'il ne peut pas traverser de telles surfaces. L'électrolyte intérieur ne peut pas diffuser dans le précipité. Cependant, des altérations de  $D_b$  sur les bordures passives ainsi que dans le précipité volumique ne modifient pas les résultats de la simulation. Le précipité ne peut pas diffuser du tout. La réaction, de taux de réaction constant  $r$ , est supposée linéaire dans les concentrations des réactants.

Les règles d'automate cellulaire ont la signification suivante. L'apparition d'un nouveau front de précipité est encodée par la règle "0". Si en un point du champ de réaction il n'y a ni précipité ni obstacle (site vide) et si la concentration de  $c$  est plus grande que le seuil de nucléation  $c^{**}$ , alors des nouveaux segments de front apparaissent (sites actifs). La règle 1 décrit l'évolution d'une bordure active. Si la concentration de DC est plus grande que le seuil  $c^*$  en un site d'une bordure active alors tous les sites plus proche voisins qui sont "vides" deviennent actifs. Le composé DC est supposé être consommé durant ce processus et, en conséquence, il disparaît du site source. Le modèle suppose que la précipitation ne peut avoir lieu qu'à la surface du précipité. Aussi, une cellule qui a activé son voisinage doit devenir passive. Ce fait est aussi encodé dans la règle 1. Les règles 2 et 3 expriment le fait que la concentration de DC doit atteindre le seuil  $c^*$ , dans le temps  $\tau(v)$ , mesuré à partir de l'apparition de la cellule active, pour rester actif, sinon l'élément va se trouver dans un état passif. Le vieillissement des cellules est décrit par la règle 3. Les diverses formes considérées pour la fonction  $\tau(v)$  sont discutées dans le paragraphe 4.2.

La règle 4 décrit un second mécanisme de "passivisation" qui peut être vu comme une extension de la règle 1. Les cellules d'une bordure active sont rendues passives pour toute configuration lorsqu'elles deviennent entourées par des cellules actives ou passives. Remarquons qu'une cellule active entourée de cellules de précipité ou de portions d'obstacles devient également passive. Dans l'implémentation numérique du modèle, on applique tout d'abord les équations différentielles puis les règles d'automate dans l'ordre R0-R1-R2-R3-R4.

Les structures secondaires ont été modélisées par une approche de type Cahn-Hilliard pour la décomposition spinodale du produit de réaction. Un ingrédient important de cette théorie est l'énergie libre de Ginzburg-Landau [202] entrant dans l'équation de Cahn-Hilliard. Par un changement de l'échelle pour les concentrations, on peut considérer que les minima de l'énergie libre correspondant aux densités des deux phases en équilibre sont égales à  $\pm 1$ . Afin de se concentrer sur l'aspect formation de structures, nous ne décrivons pas explicitement le processus de réaction-diffusion à l'origine du composé chimique qui entre dans l'équation de Cahn-Hilliard. La création de ce composé est modélisée par un terme source  $S(x, t; v)$ , gaussien. L'équation d'évolution pour la concentration  $c(x, y, t)$  de ce composé s'écrit:

$$\frac{\partial c(x, y, t)}{\partial t} = -\Delta[c(x, y, t) - c(x, y, t)^3 + \epsilon \Delta c(x, y, t)] + S(x, y, t; v) \quad (1.1)$$

où

$$S(x, y, t; v) = A \cdot \exp[-\alpha(x + \beta - vt)^2]; \quad (1.2)$$

Initialement, la concentration  $c$  du composé est choisie comme étant  $c_0(x, y, 0) = -1 + \eta$  dans tout le système, où  $\eta$  est un nombre aléatoire uniformément distribué entre  $-0.001$  et  $+0.001$  [200]. Ce bruit a été ajouté dans le but de rendre le modèle plus réaliste.

Le front qui se déplace à vitesse constante  $v$  laisse derrière lui une concentration constante  $c_f$  du composé. La vitesse  $v$  de la source, ainsi que la concentration  $c_f$  près du front de la source sont considérées comme des paramètres indépendants dans la

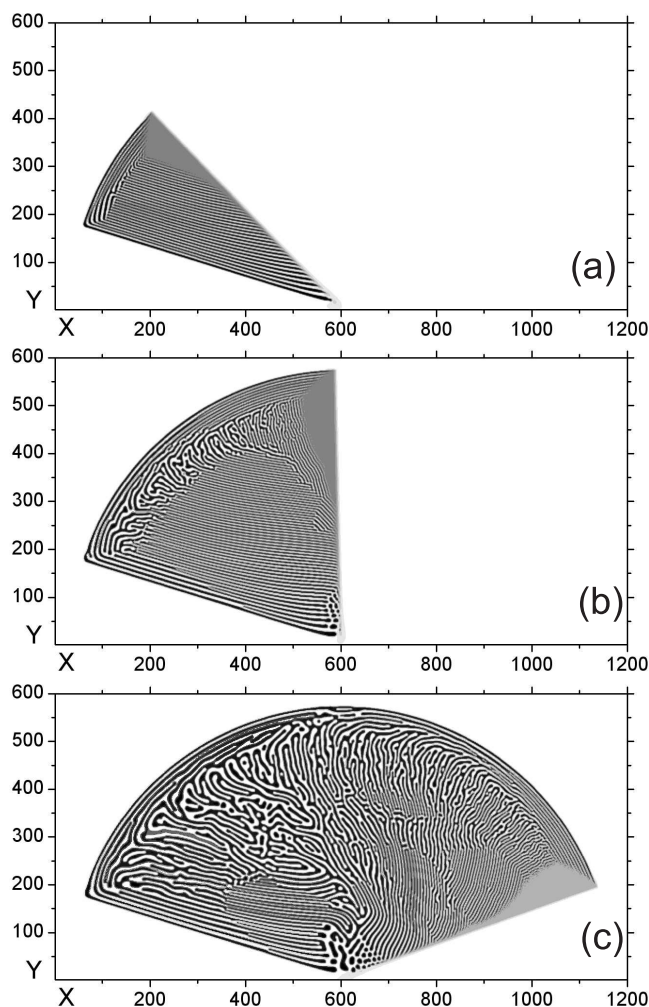


Figure 1.3: Formation de structure dans le sillage d'un front en rotation. La vitesse angulaire est  $\omega = 0.005$ . La simulation est faite sur une grille de taille  $1200 \times 600$ .  $\epsilon = 0.5$ ,  $x_0 = 600$ ,  $y_0 = 5$ ,  $A = 0.00089$ ,  $\alpha = 0.1$ ,  $c_f = 1$ ,  $c_0 = -1 + \eta$ . La région derrière le sillage du front où l'on observe: (a.) Formation de bandes obliques au temps  $t = 100$ . (b.) L'angle critique est atteint au temps  $t = 250$  et la croissance des bandes devient instable. (c.) Une morphologie oblique se développe dans le sillage du front au temps  $t = 500$ .

simulation. Ayant fixé la vitesse  $v$ , la valeur de  $c_f$  est déterminée par l'amplitude  $A$  et la largeur  $\alpha^{-1/2}$  du front de la source gaussienne. Si  $c_f$  se trouve entre les points spinodaux, c'est-à-dire,  $-1/\sqrt{3} < c_f < 1/\sqrt{3}$ , le système deviendra instable envers des perturbations, et la séparation de phases aura lieu dans le sillage du front. A mesure que le temps passe, le profil de la concentration  $c(x, y, t)$  tend vers des valeurs d'équilibre et une "maturation" des régions avec des concentrations stables a lieu simultanément. Les simulations numériques ont montré que les conditions initiales, ainsi que la dynamique du front, affectent fondamentalement les structures émergentes. L'équation (1.1) a été



résolue sur une grille rectangulaire utilisant la méthode des différences finies (méthode d'Euler) pour des conditions aux limites périodiques dans les deux directions.

Des simulations numériques ont reproduit des bandes parallèles et légèrement obliques par rapport au front. Des bandes obliques apparaissent lorsque le front change de direction, alors que les bandes nouvellement formées gardent l'orientation des bandes antérieures [202].

La formation de structures à l'arrière d'un front tournant de réaction-diffusion jouant le rôle de source a aussi été étudié. La dynamique de formation des bandes est la suivante: une première bande se forme approximativement en s'allignant avec la position initiale du front. Bien que l'orientation du front varie continuellement, les nouvelles bandes essayent de se former parallèlement aux précédentes. Il en résulte une morphologie de bandes obliques. Cependant, les simulations montrent que les bandes ne peuvent pas grandir perpendiculairement au front. Leur élongation devient instable lorsque l'angle entre les bandes et le front atteint environ 70 – 90 degrés. Dès lors, apparaissent juste derrière le front, des bandes obliques (avec un petit angle). Dans d'autres domaines, des domaines de morphologies irrégulières apparaissent. Le même scénario peut se répéter.

Un mécanisme alternatif conduisant aussi à une séparation de phases dans le sillage du front est le suivant. La concentration du composé se trouve à l'intérieur de la ligne spinodale et la température tombe au-dessous de la valeur critique à l'arrière du front. La formation des structures dans le sillage d'un front refroidi a aussi été examinée par ordinateur et comparée aux résultats précédents. Il a été démontré qu'en-dessous d'une certaine vitesse du front, des bandes perpendiculaires au front apparaissent. De plus, celles-ci vont se construire de manière à ce que leurs extrémités croissantes restent perpendiculaires même si le front change de direction. Cet effet nous permet de "créer" des bandes régulières sur une surface en suivant une courbe arbitraire.

Les résultats obtenus peuvent avoir d'importantes applications dans le cadre des nanotechnologies et la lithographie.



# Chapter 2

## Introduction

While many things around us are designed, most of them, such as living beings or snowflakes, are formed spontaneously. The science of pattern formation deals with the spontaneous processes that generate complex shapes and well-ordered structures, over the range of the molecular scale.

A great variety of pattern-forming phenomena in physical [1–6], chemical [7–13] and biological [14–18] systems are governed by reactions coupled with diffusion.

In the following sections a review of some important reaction-diffusion governed, physical and chemical pattern-forming processes is given. A special emphasis is put on the short presentation of the mathematical basis of these phenomena.

### 2.1 Reaction-diffusion Patterns in Active Media

Behavior of reaction-diffusion systems are various. If we restrict ourselves to spatially homogeneous systems (without the coupling represented by the diffusion term), their dynamics can be described by ordinary differential equations. Current investigations are centered on a few special classes of such models. *Excitable media* have a single stationary state that is stable under small perturbations, while perturbations above a certain threshold provoke a burst of activity before the system returns to rest. In the case of *oscillatory media* some physical or chemical parameters show spontaneous periodic changes in time. *Multistationary* media have several stable and unstable steady states. In the case of two stable (and some unstable) steady states these are called *bistable* systems; large enough perturbations can trigger transitions between the stable states. If the system has a stable and an unstable steady state, small perturbations are able to trigger the transition from the unstable state to the stable one [5, 15]. All of these types of *active media* will be discussed later in detail.

When different locations of spatially extended systems are coupled through diffusion, effects of a perturbation will spread, leading to various spatial and spatio-temporal patterns that can be modeled by partial differential equations and cellular automata [19–22]. The most important structures will be presented in the following chapters.

### 2.1.1 Classification

If the spatially homogeneous stable steady-state of a reaction-diffusion system becomes unstable as a *control parameter* is varied, the first stage of the pattern formation can usually be investigated by linear stability analysis. This method results in *dispersion relations*, that allow further classification of the phenomena [1, 15, 26, 27].

#### Linear Stability Analysis

Several reaction-diffusion systems build up nontrivial patterns when their stable steady-state loses stability, as one or more control parameters are changed. Depending on the character of the instability, various static and dynamic patterns that can be periodic in space (Turing structures), in time (homogeneous oscillations) or both in space and time (packet waves and standing waves) might arise.

In the following, we present some basics of the linear stability analysis that will lead us to the dispersion relations. Let us consider a two-component, one-dimensional, infinitely extended reaction-diffusion system. The components are denoted by  $U$  and  $V$ , while the control parameter(s) by  $\gamma$ .

$$\begin{aligned}\frac{\partial U(x,t)}{\partial t} &= D_U \Delta U(x,t) + f(U(x,t), V(x,t), \gamma) \\ \frac{\partial V(x,t)}{\partial t} &= D_V \Delta V(x,t) + g(U(x,t), V(x,t), \gamma)\end{aligned}\quad (2.1)$$

Assume that the system has a spatially uniform steady-state

$$U(x,t) = U_0, \quad V(x,t) = V_0 \quad (2.2)$$

where

$$f(U_0, V_0, \gamma) = 0, \quad g(U_0, V_0, \gamma) = 0 \quad (2.3)$$

The above solution can be either stable or unstable in respect to disturbances. In order to examine its stability, we add small perturbative terms to the steady-state values  $U_0$  and  $V_0$ :

$$\begin{aligned}U(x,t) &= U_0 + u(x,t) \\ V(x,t) &= V_0 + v(x,t)\end{aligned}\quad (2.4)$$

By replacing these expressions in (2.1), and linearizing the functions  $f$  and  $g$  around the steady state, we have

$$\begin{aligned}\frac{\partial u(x,t)}{\partial t} &= D_U \Delta u(x,t) + a_{11}u(x,t) + a_{12}v(x,t) \\ \frac{\partial v(x,t)}{\partial t} &= D_V \Delta v(x,t) + a_{21}u(x,t) + a_{22}v(x,t)\end{aligned}\quad (2.5)$$

Evolution of the perturbations around the steady state  $(U_0, V_0)$  can be explored by Fourier transforming in the  $x$  variable (here we assume that  $u(x, t)$  and  $v(x, t)$  decrease to zero faster than any polynomial function as  $x \rightarrow \pm\infty$ ):

$$\begin{aligned} u(x, t) &= \int_{-\infty}^{\infty} \tilde{u}(k, t) e^{ikx} \cdot dk \\ v(x, t) &= \int_{-\infty}^{\infty} \tilde{v}(k, t) e^{ikx} \cdot dk \end{aligned} \quad (2.6)$$

By inserting the above integrals into (2.5), and decomposing the modes with different wave numbers  $k$ , results

$$\begin{aligned} \frac{\partial \tilde{u}(k, t)}{\partial t} &= -D_U k^2 \tilde{u}(k, t) + a_{11} \tilde{u}(k, t) + a_{12} \tilde{v}(k, t) = (a_{11} - D_U k^2) \tilde{u}(k, t) + a_{12} \tilde{v}(k, t) \\ \frac{\partial \tilde{v}(k, t)}{\partial t} &= -D_V k^2 \tilde{v}(k, t) + a_{21} \tilde{u}(k, t) + a_{22} \tilde{v}(k, t) = a_{21} \tilde{u}(k, t) + (a_{22} - D_V k^2) \tilde{v}(k, t) \end{aligned} \quad (2.7)$$

This is a system of linear equations in  $\vec{W}(k, t) = (\tilde{u}(k, t), \tilde{v}(k, t))$ , that, in simple notations, can be written as

$$\dot{\vec{W}} = \mathbf{A} \vec{W} \quad (2.8)$$

This system has nontrivial solutions when

$$\begin{vmatrix} a_{11} - D_U k^2 - \Omega(k) & a_{12} \\ a_{21} & a_{22} - D_V k^2 - \Omega(k) \end{vmatrix} = 0$$

The resulting quadratic equation in the most general case has two complex roots for the eigenvalues  $\Omega(k)$ :

$$\Omega(k)_{1,2} = \text{Re}(\Omega(k)) \pm i \text{Im}(\Omega(k)) \quad (2.9)$$

These functions are called *dispersion relations*.

Let us to denote the left and right eigenvectors of the matrix  $\mathbf{A}$ , belonging to the eigenvalues  $\Omega(k)_{1,2}$  by  $\vec{l}_{1,2}(k)$  and  $\vec{r}_{1,2}(k)$ . As known from the elementary theory of differential equations, the solution of (2.7) reads as

$$\vec{W}(k, t) = \alpha(k) \exp(\Omega_1(k)t) \vec{r}_1(k) + \beta(k) \exp(\Omega_2(k)t) \vec{r}_2(k) \quad (2.10)$$

where  $\alpha(k) = (\vec{l}_1(k), \vec{W}(k, 0))$ ,  $\beta(k) = (\vec{l}_2(k), \vec{W}(k, 0))$ . Note that in the physics literature usually the exponent is multiplied by  $i$ , while in nonlinear science the above notation is common. The (real) solutions of the linearized equations (2.5) in the physical space can be written by using of (2.6).

Remember that the above results represent the case of an infinitely extended reaction field. In case of a reaction field with finite extent, the Fourier integrals are replaced with series, and special attention has to be paid to fulfill the boundary conditions.

As mentioned above, some periodic structures that appear in reaction-diffusion (RD) systems of the above type, can be classified on the basis of the dispersion relations. Let us denote by  $k_0$  the wave number where the real part of the dispersion relation becomes positive for the first time, as the parameter(s)  $\gamma$  are slightly varied. Let us assume that this value is unique for  $k \geq 0$ .

If  $Re(\Omega(k_0)) > 0$  only at  $k_0 = 0$  (no spatial patterns) and  $Im(\Omega(k_0)) \neq 0$  (temporal oscillations) then a Hopf bifurcation appears, leading to bulk oscillations [7, 11, 23, 40].

Stationary spatial patterns appear when  $Im(\Omega(k_0)) = 0$  (stationarity) and  $Re(\Omega(k_0)) > 0$  at  $k_0 \neq 0$  (condition for spatial patterns to appear), that will be referred to as Turing instability. However, in the majority of the literature, Turing instability is defined as  $Re(\Omega(0)) < 0$  (stability of the homogeneous steady-state) and  $Re(\Omega(k_0)) > 0$  at  $k_0 \neq 0$  (condition for spatial patterns to appear) [15, 28]. If we accept this definition, Turing patterns of reaction-diffusion systems with more than two components are not always stationary [28]. Note that in the case of a two-component reaction-diffusion system the latter definition entails  $Im(\Omega(k_0)) = 0$ , *i.e.* the stationarity. The degeneracy of the terminology can be assigned to the fact that there was no comprehensive definition in Turing's original paper [29].

If  $Re(\Omega(k_0)) > 0$  at  $k_0 \neq 0$  and  $Im(\Omega(k_0)) \neq 0$  then several types of spatio-temporal patterns can appear, like "packet waves" or "standing waves" [27, 30, 31].

In the following, we give a short overview of these types of instabilities.

## Oscillating Chemical Reactions

Chemical reactions in well-mixed closed vessels usually evolve in such a way that the concentration of reactants monotonically decrease, that of the products increase, while that of the intermediate compounds increases at the beginning of the process, but tends towards zero at the end [32–34].

However, there are some chemical processes like the famous *Belousov-Zhabotinsky (BZ)* reactions [10, 35–37], where the concentrations of the intermediate compounds oscillate (fig. 2.1), those of the reactants decrease, while those of the products increase in a step-like way as the reaction goes on. Such *bulk oscillations* can appear if instead of a simple reaction we have a set of parallel processes, at least one of them being autocatalytic, and one inhibitory.

The reactions can be run either in closed vessels ("batch reactors"), or in continuous-flow well-stirred tank reactors (CSTR). The latter are open systems that have a continuous inflow of fresh reactants, and a matching outflow of products. At these conditions the BZ reactions can exhibit more complex behavior than in closed vessels [37].

The two most widely used models of the oscillating reactions are the *Brusselator* and *Oregonator* models [7, 9–11, 15]. The two-variable Brusselator model has been developed for describing chemical dissipative structures in general. The Oregonator was elaborated later, being designed for characterizing the BZ reactions, *i.e.* catalyzed oxidation of malonic acid by bromate in the presence of Cerium as a catalyst. Note that the Oregonator gives a very rough description. The MBM (Marburg-Budapest-Missoula)

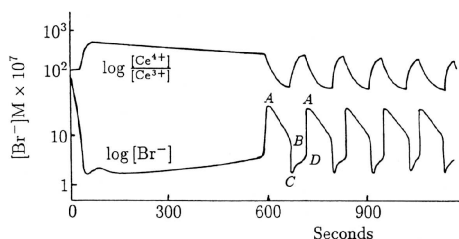


Figure 2.1: BZ reaction in a closed vessel showing oscillations in the concentrations of two intermediate compounds [15, 36].

model represents a more faithful approach [35].

The reagents of the BZ reaction are malonic acid ( $CH_2(COOH)_2$ ),  $Ce^{4+}$  (this ion is also an intermediate compound, since it is consumed and reproduced during the reaction; it is usually put in the reactor in the form of cerium sulphate) and  $BrO_3^-$  (applied usually as sodium bromate). The acidity of the hydrous environment is ensured by adding  $H_2SO_4$  to the system. The most important inorganic intermediate compounds are  $HBrO_2$ ,  $Br^-$  and  $Ce^{4+}$ , representing the variables of the Oregonator model. In the following, we give an overview of the batch (closed vessel) Oregonator model of the BZ reaction [9], for the case when the change in the reactant concentrations in the solution during a cycle is negligibly small.

The model reactions can be approximated by the sequence



where  $X = [HBrO_2]$  (bromous acid),  $Y = [Br^-]$  (bromide),  $Z = [Ce^{4+}]$ ,  $A = [BrO_3^-]$  (bromate),  $B = [Org]$  (organic species, basically the malonic acid [38]) and  $P = [HOBr]$  (hypobromous acid).

Reaction rate constants are denoted by  $k_i$ , while  $F$  is the number of  $Br^-$  ions produced as two  $Ce^{4+}$  ions are reduced to  $Ce^{3+}$ . The parameter  $F$  depends on the stoichiometry of the model. Since the Oregonator is a rough model of the reactions (that are not known in all details), the interpretation of parameter  $F$  strongly depends on the authors. In some models it has a constant value [39], but recent investigations suggest that it is proportional to the concentration of the organic species, mainly bromomalonic acid ( $BrCH(COOH)_2$ ) [9]. Note that reactions involving the bromomalonic acid are not included in the Oregonator model.

Due to the autocatalytic process  $A + X \xrightarrow{k_5} 2X + 2Z$ , concentration of  $X$  increases rapidly, when that of  $Y$  is small. However,  $Y$  inhibits  $X$ , representing delayed negative feedback. Thus, in principle, the system can be driven in oscillatory mode.

The rate equations of the Oregonator model are the following:

$$\begin{aligned}\frac{dX}{dt} &= k_3AY - k_2XY + k_5AX - 2k_4X^2 \\ \frac{dY}{dt} &= -k_3AY - k_2XY + \frac{1}{2}k_0FBZ \\ \frac{dZ}{dt} &= 2k_5AX - k_0BZ\end{aligned}\tag{2.16}$$

Diffusion terms are not included in the system. This is because we consider the well-mixed case, when there are no concentration gradients, and thus no diffusive transport is present. Concentration of the organic species ( $B$ ) as well as that of the bromate ( $A$ ) are considered to be constant.

The dimensionless equations of the model are the following:

$$\begin{aligned}\epsilon \frac{du}{dt} &= qw - uw + u(1 - u) \\ \delta \frac{dw}{dt} &= -qw - uw + Fv \\ \frac{dv}{dt} &= u - v\end{aligned}\tag{2.17}$$

Here  $u$ ,  $w$  and  $v$  are proportional to the concentrations of  $HBrO_2$ ,  $Br^-$  and  $Ce^{4+}$ , respectively.  $\epsilon = \frac{k_0B}{k_5A} \approx 4 \cdot 10^{-2}$  and  $\delta = \frac{2k_0k_4B}{k_2k_5A} \approx 4 \cdot 10^{-4}$ , while  $q = \frac{2k_3k_4}{k_2k_5} \approx 8 \cdot 10^{-4}$ .

Let us regard a positive steady-state of the model, where  $u = u_s$ ,  $w = w_s$  and  $v = v_s = u_s$ . By linearizing around this steady-state, we get a third order equation for the eigenvalues,

$$\lambda^3 + \alpha\lambda^2 + \beta\lambda + \gamma = 0\tag{2.18}$$

where the constants  $\alpha$ ,  $\beta$  and  $\gamma$  are functions of the parameters  $q$  and  $F$ , and also of the steady-state values  $u_s = v_s$  and  $w_s$ . The solution  $(u(t), w(t), v(t))$  is a linear combination of the three exponential terms  $exp(\lambda_i t)$ , plus a constant depending on initial conditions. Of course the solution is always real, but the linear combination constants can be complex.

It can be shown that the steady-state solution is linearly unstable when for a certain function  $\Phi$

$$\Phi(\delta, F, \epsilon) > 0\tag{2.19}$$

It can also be demonstrated that a supercritical Hopf bifurcation takes place when  $\Phi = 0$  [15, 23, 40]. Note that in reality other types of bifurcations can also occur [41]. As we penetrate into the unstable region, one of the eigenvalues is real and negative, while the other two are complex conjugated pairs, with a positive real part. As a consequence, the phase space trajectory shrinks to a plane where it will take the form of a small loop (fig. 2.2 (a.)). Thus,  $u(t)$ ,  $w(t)$  and  $v(t)$  begin to "oscillate". Since the bifurcation is Hopf-type, the amplitude of the oscillations is limited.

As we move into the interior of the oscillatory region, higher-order nonlinear effects become important and the Hopf approach for the phase space trajectory and the period

of oscillations cannot be used accurately. However, at these conditions, the *relaxation oscillator method* represents an effective way to study the oscillations. Since this scheme was developed for two-component systems, one of the variables has to be eliminated from the Oregonator model using the *quasi steady-state approach*. Both of these methods belong to singular perturbation theory [23, 42].

The quasi-steady-state approximation (QSSA) is a mathematical way of simplifying systems of differential equations describing some chemical processes, by replacing a part of the differential equations with algebraic ones [43–45].

Let us consider a system of ordinary differential equations:

$$\frac{du}{dt} = f_1(u, w, v) \quad (2.20)$$

$$\epsilon \frac{dw}{dt} = f_2(u, w, v) \quad (2.21)$$

$$\frac{dv}{dt} = f_3(u, w, v) \quad (2.22)$$

If the parameter  $\epsilon$  is very small and we are far from the surface  $f_2(u, w, v) = 0$ , the value of  $\frac{f_2}{\epsilon}$  is much higher than the values of the functions  $f_1$  and  $f_3$ . Thus, a phase space trajectory starting far from the surface  $f_2 = 0$  will have a high-valued  $\dot{w}$ , in comparison with  $\dot{u}$  and  $\dot{v}$ . As a consequence, the first segment of the phase space trajectory will be almost perpendicular to the plane  $(u, v)$ . Let us assume that the surface  $f_2 = 0$  attracts the phase space trajectories. When reaching the immediate vicinity of this surface, the amplitude of  $\dot{w}$  decreases, and after a while will be of the same order of magnitude as the other two speeds. Note that the reason why  $w$  is called *fast*, while  $u$  and  $v$  *slow* variables is that  $w$  relaxes much faster to  $f_2 = 0$  as the variables  $u$  and  $v$  vary.

When  $f_2 = 0$  has an arbitrary, but smooth shape and  $\epsilon$  is very small, the trajectory will run in the immediate vicinity of the surface. Therefore,  $\dot{w}$  will be small. The other components of the speed are determined by the dynamics of  $u$  and  $v$ . However, since the movement takes place in the very neighborhood of  $f_2 = 0$ , the resultant velocity vector has to be tangent to the surface.

What error would result if we performed the calculations as if the trajectory were *exactly* on the  $f_2 = 0$  surface? According to (2.21) this means  $\dot{w} = 0$ , which is obviously an unacceptable simplification. However, we can consider  $f_2 = 0$  in a different way, only as being a *geometric constraint*: although we disregard the dynamics of  $w$ , and only the dynamics of  $u$  and  $v$  shift the phase space point, the movement has to proceed *on*  $f_2 = 0$ . If this surface is not parallel to the  $(u, v)$  plane, the fact that the phase space point moves on  $f_2 = 0$  "causes" a nonzero speed  $\dot{w}$ . Rather than considering  $w$  to lie in the immediate vicinity of the surface  $f_2 = 0$ ,  $w$  may be expressed from  $f_2 = 0$  with  $u$  and  $v$  given, and the system 2.20-2.22 can be reduced (the QSSA approximation). Note that the constraint can be such that  $\dot{w}$  is even greater than  $\dot{u}$  or  $\dot{v}$ , and the QSSA still holds.

The error caused by this method is small when the QSSA trajectory (embedded in  $f_2 = 0$ ), and the corresponding "real" trajectory (that can be found by exact solutions,

or can be estimated by an accurate numerical integration), are close to each other. It can be shown that in the case when the partial derivative of  $f_2$  with respect to  $w$ , that is responsible for "pushing" the trajectory to  $f_2 = 0$ , is great at the points in the vicinity of  $f_2 = 0$ , the error of the QSSA will be small even if  $\dot{w}$  of the "real" trajectory is large at that point [45].

However, if the surface  $f_2 = 0$  is almost parallel to the  $(u, w)$  or  $(u, v)$  plane, the partial derivative of  $f_2$  with respect to  $w$  becomes so small that the trajectory will not reach the vicinity of the surface, and will not be governed by the dynamics of  $u$  and  $v$  and the geometry of the surface. Here the QSSA cannot be applied.

Let us turn back to the Oregonator model of the BZ reaction. Depending on the initial concentrations and the estimates of the rate constants, different values are obtained for  $\epsilon$  and  $\delta$ . We will follow the approach presented in [9], where  $\delta \ll \epsilon \ll 1$ , and thus the QSSA can be applied for the variable  $w$ . The functions  $f_i$  are shaped in such a way that the phase trajectory, besides moving along the surface  $f_2 = 0$ , sometimes performs jumps between two parts of this curved surface. When the phase space point moves far from the surfaces, the QSSA obviously cannot be applied. The QSSA approach is valid only when the trajectory moves in the immediate vicinity of  $f_2 = 0$ . However, we are interested only in sketching a phase space trajectory. The system spends the overwhelming majority of the cycle in the vicinity of  $f_2 = 0$  ("stable branches"), and the straight "jumps" connecting the stable branches are very short in time. Having noticed this, QSSA can formally be applied for the whole cycle.

Performing the quasi steady-state approximation, we obtain the following system of two equations:

$$\begin{aligned}\epsilon \frac{du}{dt} &= u(1-u) - \frac{u-q}{u+q} Fv = f(u, v) \\ \frac{dv}{dt} &= u - v = g(u, v)\end{aligned}\tag{2.23}$$

Further study of the oscillatory behavior of this system can be achieved by the *relaxation oscillator method* [1]. This approach describes, in an intuitive way, the trajectory of the system in the concentration phase space, and also gives an estimate for the period of the oscillation. It can be applied when the limit cycle is divided into distinct segments, some where the concentrations are varying slowly and others where there are sharp changes. Note, that this classification of fast and slow changes has nothing to do with the one performed in the QSSA. For a system having nullclines as in fig. 2.2, this holds if one of the derivatives is multiplied by a small constant term. All of these conditions hold for the system 2.23. The "fast" segment of the trajectory can be approximated by a straight line. When calculating the period of an oscillation, these segments are neglected, since the overwhelming majority of the time, the system is on the nullcline portions  $h_-$  and  $h_+$ . Using the first equation of 2.23, the estimate for the time period is

$$T = \int_{v^<}^{v^>} \frac{dv}{g(h_+(v), v)} + \int_{v^>}^{v^<} \frac{dv}{g(h_-(v), v)}\tag{2.24}$$



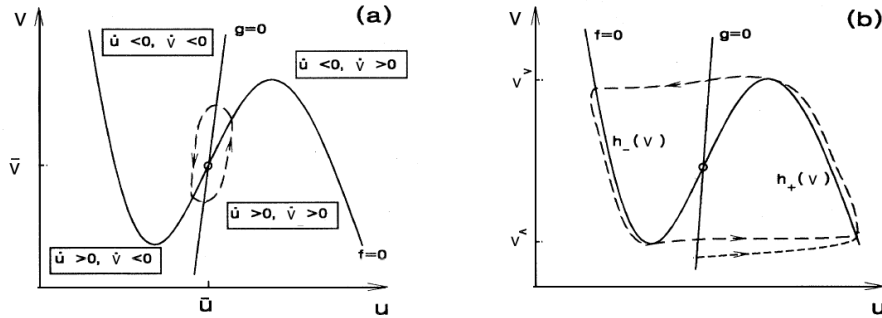


Figure 2.2: Approximate phase trajectories of the Oregonator model close to the Hopf boundary (a.) and in the relaxation oscillator approach (b.) [1].

Finally, we mention that by changing the parameter  $F$ , the reaction can be driven to oscillatory and excitable modes, but not to a bistable mode. In the case of the extended flow-Oregonator models that describe the reactions proceeding in a CSTR (continuous-flow well-stirred tank reactor), bistable modes can also be achieved [37].

### Turing Mechanism

Turing patterns are known as spatial structures having a characteristic wavelength. As mentioned above, the Turing bifurcation has not been defined in a unique way. We will adopt the definition that Turing instability leads to spatially periodic patterns that are stationary in time.

In the two-component case it can be proved that for the above instability to appear we must have

$$a_{11} + a_{22} < 0 \quad (2.25)$$

and

$$D_V a_{11} + D_U a_{22} > 0 \quad (2.26)$$

Having positive diffusion coefficients, these relations can hold only if the following conditions are satisfied [7]:

1. One of the diagonal elements of the Jacobian is positive, and the other negative. For specificity, let us suppose that  $a_{11} > 0$ . This means that the species  $U$  enhances the rate of its own production, while  $V$  diminishes this rate. Thus,  $U$  is involved in an autocatalytic process. Compound  $U$  is called the *activator*, while  $V$  is called the *inhibitor* [7, 14, 46, 47].

2. It is also required that

$$\frac{D_U}{D_V} < 1 \quad (2.27)$$

*i.e.* the inhibitor must diffuse more rapidly than the activator [7].

Note that after a certain time the amplitude of the periodic patterns are “growing out” from the linear regime, where they become limited by the nonlinearities of the

system. Obviously, the nonlinear effects are not taken into account in the linear stability analysis. A more detailed analysis of the Turing instability (*e.g.* deciding whether dot-like or labyrinth-like patterns will appear) can be performed using amplitude equations [48].

In his famous paper from 1952, A. M. Turing suggested that the above mechanism can account for the formation of various processes in biological morphogenesis [29]. Later, the ideas of Turing were improved, and today it is believed that the development of animal coat patterns (fig. 2.3), plant phyllotaxis and chicken feathers follows the Turing mechanism [17, 49, 50]. However, up to this time (2004) there is no experimental evidence that proves this hypothesis.



Figure 2.3: Marine angelfish *Pomacanthus semicirculatus* (juvenile). The patterns on the skin are supposed to be Turing patterns [49, 51].

We should mention that there are several other mechanisms that yield periodic structures in space. Moreover, according to some recent results, periodic patterns where the number of stripes is smaller than four, or where the pattern must be precisely defined, are assumed to be built up not by the Turing mechanism, but by a so-called hierarchical process [52].

Beginning from the 90's, several chemical systems have been developed in which the emergence of Turing patterns was observed. The main difficulty in the construction of such a system is the assurance of significantly high differences between the diffusion coefficients of the activator and the inhibitor [53, 55].

The first chemical process where Turing patterns were found was the CIMA (chlorite-iodide-malonic acid) reaction in polyacrylamide gel impregnated with starch. The big starch molecules are unable to diffuse in the gel, and by forming starch-triiodide complexes, the effective diffusivity of iodine and iodide molecules is slowed relative to the chlorite and chlorine dioxide [54].

A recent accomplishment is the development of the so-called BZ-AOT chemical system [55], where – among others – Turing patterns can also emerge (fig. 2.4). Here nanometer-sized droplets of water (the aqueous pseudo-phase), surrounded by a surfactant called AOT, are dispersed in octane (the oil phase). Communication between the droplets may occur via diffusion (nonpolar molecules) or as a result of mass exchange during droplet collision/fission/fusion (polar molecules). Thus, the diffusion of the non-polar species is  $2 \cdot 10^{-5} \text{cm}^2/\text{s}$ , while that of the polar species is one or two orders of

magnitude smaller.

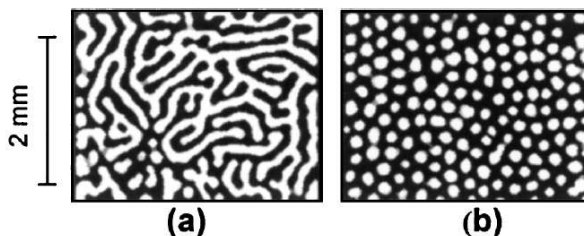


Figure 2.4: Turing patterns in the BZ-AOT system [55].

Initially, the BZ reagents are present in the aqueous phase, but the nonpolar compounds can diffuse into the oil phase. Highly hydrophilic ions and the polar compounds remain in the micelles. Although the inhibitor species  $Br^-$  cannot leave the micelles,  $Br_2$  (that is in dynamical equilibrium with  $Br^-$ ) can travel through the oil phase. The most important autocatalytic species,  $HBrO_2$ , is a polar molecule. Thus, the inhibitor has a large effective diffusion coefficient, while the activator  $HBrO_2$  is diffusing very slowly. In this way, the main condition for the appearance of the Turing patterns is fulfilled. Note that the above scenario is valid when the droplet fraction  $\Phi_d$  is smaller than 0.5, *i.e.* we are below the percolation threshold of the micelles.

### Packet Waves and Standing Waves

In the recently developed BZ-AOT chemical system, the formation of a new spatiotemporal structure, the *packet wave* [27, 30, 31], has been observed for certain parameter values. The emergence of these structures was previously predicted in theoretical works and computer simulations [58]. The modeling of this system shows that the stability is lost in such a way that  $Re(\Omega(k_0)) > 0$  at  $k_0 \neq 0$  and  $Im(\Omega(k_0)) \neq 0$ , leading to patterns that are periodic in space and time.

The amplitude of the packet waves is much smaller than that of the pulses or wave-trains in excitable media. It is important to mention that in linear stability analysis their amplitude (as well as the amplitude of Turing patterns) cannot be predicted. In a very short time they “grow out” from the linear region, and higher order terms limit their amplitude. The “component-waves” of a packet cannot exist alone, only as part of a wave packet that is slowly expanding in time. The collision of two packet waves leads to an increase in the amplitude of oscillations at the point of collision, and can be regarded as an example of ‘chemical interference’.

In order to characterize the dynamics of the packet waves, we have to use the concept of group and phase velocities. Let us regard the one-dimensional case. Group velocity (*i.e.* the speed of the maximum point of the packet’s envelope) is defined as

$$c_g(k_0) = \left. \frac{d \operatorname{Im}(\Omega(k))}{dk} \right|_{k=k_0} \quad (2.28)$$

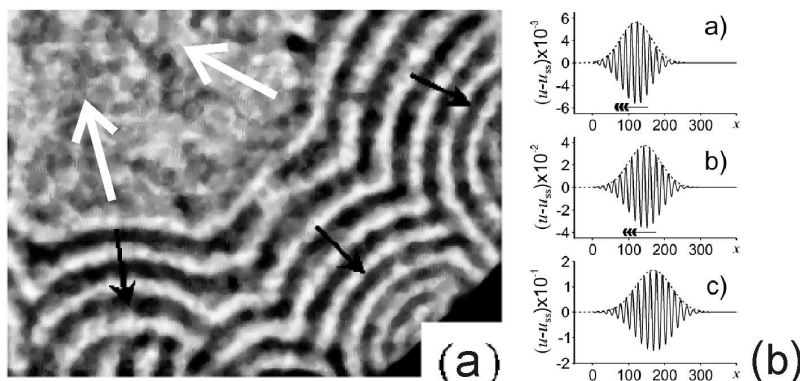


Figure 2.5: Propagation of chemical “packet waves” having the group and phase velocities of different signs (a.) Experiments in BZ-AOT system. The white arrows show the traveling direction of the packet, while the black arrows show the traveling direction of the “component-waves” [30]. (b.) Computer simulation of a “packet wave” [27]. The arrow marks the propagating direction of the “component-waves”.  $u$  represents the dimensionless concentration of the activator.

where  $k_0$  is the approximate wave number of the “component-waves”. The phase velocity of the ‘component-waves’ is

$$c_p(k_0) = \frac{\text{Im}(\Omega(k_0))}{k_0} \quad (2.29)$$

If the signs of the group and phase velocities are the same, the packet and the “component-waves” shift to the same direction. If the signs are different, they move in opposite directions, *i.e.* the ‘component-waves’ appear at the leading edge of the packet, and propagate toward its tail (fig. 2.5) <sup>1</sup>.

Another interesting feature of the packet waves is their ability to yield *standing waves*, *i.e.* a pattern having a constant wavelength that does not vary in space, but oscillates in time [27, 55]. When the group velocity is nonzero, the “component-waves” of the wave packet will reach the end of the experimental vessel. Here they are reflected and interfere with oncoming waves of the same amplitude, giving rise to standing waves.

### 2.1.2 Traveling Fronts, Pulses and Wavetrains

Chemical fronts, pulses and wavetrains are traveling variations of concentrations of some species. These structures occur in nonlinear reaction-diffusion systems far from equilibrium, and they *cannot* be investigated by the methods of the linear stability analysis outlined above. *Traveling fronts* convert the reactants to final products, so the compositions ahead and behind of it are different [8–10, 15, 59–61]. In *pulses* (“solitary chemical waves”), some intermediate species are produced by a front that are converted

<sup>1</sup>Note that in the case of one-dimensional systems it is a plausible convention to assign positive frequency ( $\text{Im}(\Omega(k)) > 0$ ) for each  $k \in \mathbf{R}$ . However, there are several other conventions in this field.

back by a recovery process [9, 33]. Wavetrains are comprised of a series of pulses which follow each other, being continuously initiated at a *pacemaker region* [9, 15, 62, 63].

Pulses and wavetrains are also called *trigger waves*. We do not deal with the "artificial" *kinematic waves*, that are strictly speaking "optical" illusions [62].

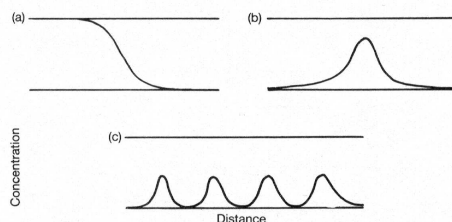


Figure 2.6: Front, pulse and wavetrain [9].

### Fronts in Multistationary Media

The spread of reaction-diffusion fronts is a characteristic of non-recoverable autocatalytic media (in which no physical or chemical processes occur after the front has swept through). In contrast to the diffusion fronts, these travel with a constant speed. The simplest (one-component) equation that describes such processes in one dimension, has the following form:

$$\frac{\partial u(x, t)}{\partial t} = D \frac{\partial^2 u(x, t)}{\partial x^2} + f(u) \quad (2.30)$$

where the function  $f(u)$  is defined in such a way that the above equation has at least two steady-states (fig. 2.7). A moving front represents a transition from one steady-state to another. Transitions can occur between two stable steady states, as well as between an unstable and a stable steady state.

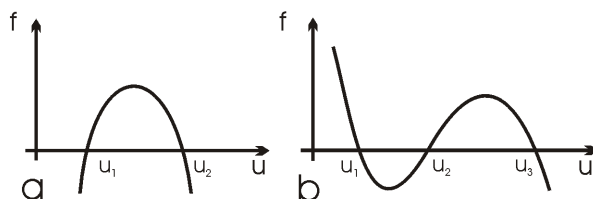


Figure 2.7: Possible functions  $f$  of (a.) Multistationary media having one stable ( $u_1$ ) and one unstable ( $u_2$ ) steady-states. (b.) Bistable media, having two stable ( $u_1$  and  $u_3$ ) and one unstable ( $u_2$ ) steady-states.

The most widely known model of fronts in media where a stable steady-state invades an unstable one, is given by the Fisher equation [23], having the form

$$\frac{\partial u(x, t)}{\partial t} = D \frac{\partial^2 u(x, t)}{\partial x^2} + ku(x, t)(1 - u(x, t)) \quad (2.31)$$

where  $k \in \mathbb{R}^+$  is a constant.

Originally it was proposed as a model for the propagation of an advantageous gene, but the same equation describes flame propagation, and spreading of some types of autocatalytic reaction fronts. Suppose, for example, that we have a long tube filled with compound  $A$ , where the  $A + B \rightarrow 2B$  reaction can take place at rate  $k[A][B]$ . If we put a small amount of  $B$  in one of the ends of the tube, its concentration will rise at that point, and also spread by diffusion along the tube, its autocatalytic growth starting at neighboring points. Thus,  $B$  will spread much faster than the speed of diffusion. The unstable state (the tube region filled with  $A$ ) can be maintained for an indefinitely long time, until the medium is not reached by the autocatalytic species  $B$ . Note that fronts invading an unstable state, where the leading edge is sufficient to catalyze its continued propagation, are called *pulled fronts* because they are "pulled" by their leading edge [64, 65].

As follows, we will look for traveling front solutions of the Fisher equation. First we observe that the equation is invariant for the  $x \rightarrow -x$  change of variable. Therefore, if we get a front solution  $F(x, t)$  propagating towards the positive direction, we also have a solution  $F(-x, t)$  propagating in the opposite direction.

The traveling front solutions will be investigated using the *phase-space method*. If such a solution exists, it can be written as  $g(z) = u(x, t)$ ,  $z = x - ct$ , ( $c > 0$ ). For the sake of simplicity, we will consider  $D = 1$  and  $k = 1$ . Thus, the equation (2.31) reduces to an ordinary differential equation:

$$g''(z) + cg'(z) + g(z)(1 - g(z)) = 0 \quad (2.32)$$

that can be transformed to a system of first-order differential equations:

$$\begin{aligned} g' &= \phi \\ \phi' &= -g(1 - g) - c\phi \end{aligned} \quad (2.33)$$

The above system has got two fixed points, namely  $(g = 0, \phi = 0)$  and  $(g = 1, \phi = 0)$ . Linearizing around  $(g = 0, \phi = 0)$ , we get the characteristic equation

$$\lambda^2 + c\lambda + 1 = 0 \quad (2.34)$$

having the roots

$$\lambda_{1,2} = \frac{-c \pm \sqrt{c^2 - 4}}{2} \quad (2.35)$$

As a consequence, this fixed point is a stable node for  $c \geq 2$ , and a stable focus for  $c \in (0, 2)$  [56, 57].

Linearizing around the fixed point  $(g = 1, \phi = 0)$ , we have

$$\lambda^2 + c\lambda - 1 = 0 \quad (2.36)$$

Regardless of the value of  $c$ , the roots of this equation are real, having opposite signs. Thus, this fixed point is a saddle.

The front solution is represented by a phase space trajectory that starts from  $(0, 0)$  and finally reaches  $(1, 0)$  (fig. 2.8). Note that having  $z = x - ct$ , as time  $t \rightarrow \infty$ ,  $z \rightarrow -\infty$ . Physically realistic are only those trajectories where  $g \geq 0$ , that is,  $c \geq 2$ . Here we mention that the above front solutions, propagating towards the positive direction, are compatible only with the boundary conditions

$$g(\infty) = 0, \quad g(-\infty) = 1 \quad (2.37)$$

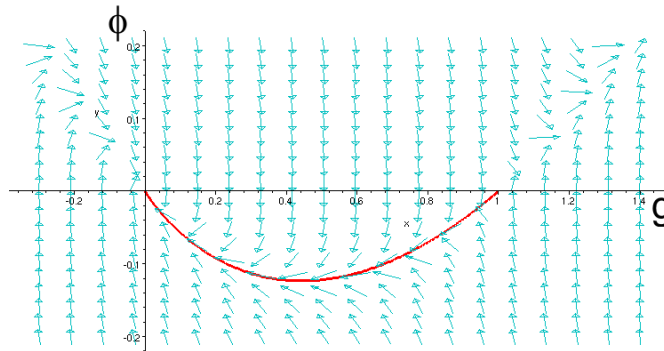


Figure 2.8: Phase space of the system of ODE resulting from the Fisher equation for the change of variable  $z = x - ct$ . The curve running from  $(0, 0)$  to  $(1, 0)$  as  $t$  increases represents the orbit corresponding to the traveling wave solution.

The problem of the front speed in the Fisher equation and its generalizations has been studied by Kolmogorov, Petrovsky and Piskunov. According to the classical “KPP” theorem, the above ‘node-saddle’ type problem where  $f'(u_1) > 0$ ,  $f'(u_2) < 0$ ,  $f(u) > 0$  for  $u \in (u_1, u_2)$ ,  $g(\infty) = u_1$ ,  $g(-\infty) = u_2$ , has traveling wave solutions above a certain front speed  $c^*$ . It is also demonstrated that the stable front has this smallest speed. The following estimate is given for speed of the stable front

$$\sqrt{4Df'(0)} \leq c^* \leq \sqrt{4D \cdot \sup \left( \frac{f(u)}{u} \right)} \quad (2.38)$$

where  $u \in (u_1, u_2)$  [20, 23]. When  $f'(u) < f'(u_1) \forall u \in (u_1, u_2)$  (that holds *e.g.* for the Fisher equation), the stable front speed can be exactly given [8],

$$c^* = \sqrt{4Df'(0)} \quad (2.39)$$

Note that the theorem holds only for sufficiently sharp initial conditions. Regarding the Fisher equation, it can be shown that for a broad class of initial conditions the asymptotic speed of the traveling front solution is  $c = 2$ , that is, the front with  $c = 2$  is stable. However, up to this time, the solution has not been found analytically [15].

As mentioned previously, the front solutions propagating in the opposite direction can be investigated by getting use of the symmetry of the Fisher equation (if  $F(x, t)$  is a

solution, than  $F(-x, t)$  is a solution too; note that changing of the boundary conditions is also required), as well as the subsequent ordinary differential equation (if  $G(z, c)$  is a solution, than  $G(-z, -c)$  is also a solution). However, they can also be studied by performing the  $g(z) = u(x, t)$ ,  $z = x + ct$ , ( $c > 0$ ) change of variable. The phase space for this case is represented in fig. 2.8.

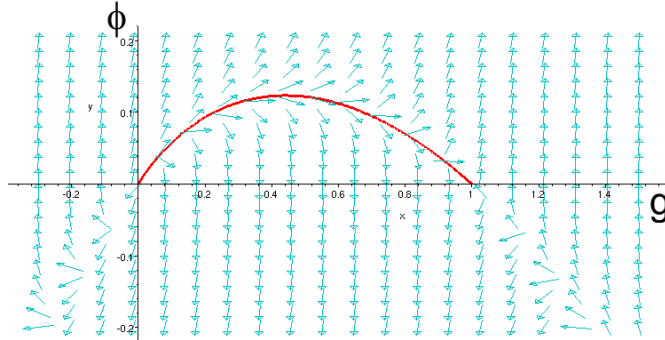


Figure 2.9: Phase space of the system of ODE resulting from the Fisher equation for the change of variable  $z = x + ct$ . The curve running from  $(0, 0)$  to  $(1, 0)$  as  $t$  increases represents the orbit corresponding to the traveling wave solution.

Note that the trajectories in the phase space, corresponding to the front solutions are unstable for both cases, but this is not related to the physical stability of the traveling fronts.

As an example, we mention the fronts propagating in the iodate-arsenite reaction in excess of iodate [66–68], having mixed quadratic and cubic autocatalysis [9]. In this reaction (fig. 2.10) the solution connects a saddle to a node, and the KPP theorem can be applied in order to estimate the speed of the front.

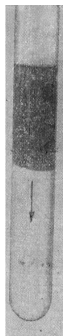


Figure 2.10: Chemical front of  $I_2$  in the iodate-arsenite reaction in excess of iodate [68].

The Fisher equation shows an example for front propagation in an active media having an unstable and a stable steady state. The phase space of fronts propagating in bistable media have two saddles and a node or focus in between. Traveling wave solutions can connect the saddles, as well as a saddle and a node. According to the



Kanel theorem, the saddle-saddle case has a traveling wave solution only for a single speed  $c^*$ , and this solution is stable [20]. However, the speed can be calculated only for some special cases of the function  $f$ .

Finally, we mention that under certain conditions fronts propagating in two-dimensional fields can show nontrivial front geometry [69, 70].

### Pulses and Wavetrains in Excitable Media

Another category of well studied active media represent the excitable systems, that are stable for small perturbations, but are temporarily "bursting" for perturbations above a certain limit. The role of such a perturbation can be played by a diffusional flow from the neighboring elements of the medium as well. This can result in the propagation of a traveling excitation pulse. Since an excitable medium goes back to (the neighborhood of) its initial state after the spreading of a pulse, the formation of traveling wavetrains is also possible. After a traveling pulse sweeps through, the recovery of the medium may either be incomplete (as in closed chemical systems), or roughly complete, but requiring an external source of energy (as in biological systems).

Many physical, chemical and biological systems can be driven into excitable states. The most well-known examples in Chemistry are the BZ reactions (fig. 2.11), that have been outlined in the preceding sections.



Figure 2.11: Wavetrains in a BZ system in excitable state. The diameter of the dish is 9 cm. The frames were taken at 1 min, 3 min 30 s, 7 min 15 s, 7 min 35 s and 16 min 20 s after the mixing of the solution [33].

Reactions on catalytic surfaces, like the oxidation of  $CO$  on Platinum(110) can exhibit excitable, bistable and oscillatory behavior as well. Modeling of pattern formation in such kind of excitable systems can be achieved by reaction-diffusion equations, having S-shaped nullclines [71–76].

Although most of the electrochemical systems exhibit oscillatory behavior, excitable ones, like corrosion of steel surfaces in the presence of nitric acid ( $Fe-HNO_3$  system) [79] have also been developed. Modeling of electrochemical systems differs from that of the reaction-diffusion processes, since they bear a nonlocal coupling through the potential drop in the electrolyte. When constant speed pulse propagation was observed, the geometry of the system (the size and positioning of the electrodes) was arranged in such a way that the coupling was almost local [77–80].

The speed of pulses (trigger waves) and wavetrains in excitable media can be estimated by methods of singular perturbation analysis [1, 10, 15, 23–25, 42]. This approach has been elaborated by Tyson and Fife for two-component reaction-diffusion models:

$$\begin{aligned}\frac{\partial u(x, t)}{\partial t} &= D_u \frac{\partial^2 u(x, t)}{\partial x^2} + \frac{1}{\epsilon} f(u, v) \\ \frac{\partial v(x, t)}{\partial t} &= D_v \frac{\partial^2 v(x, t)}{\partial x^2} + g(u, v)\end{aligned}\quad (2.40)$$

Here  $\epsilon$  is a small constant parameter, and the functions  $f$  and  $g$  have similar shapes as in fig. 2.12 (a.). Note that the fast growth of the compound  $u$  that starts when a disturbance overtakes the excitability limit, is attributed to its autocatalysis.

We can rescale the spatial variable in such a manner that the diffusion coefficient  $D_u$  transforms to unity:

$$\begin{aligned}x &\rightarrow \sqrt{\frac{D_u}{\epsilon}} x_1 \\ \frac{\partial^2}{\partial x^2} &\rightarrow \frac{\epsilon}{D_u} \frac{\partial^2}{\partial x_1^2}\end{aligned}\quad (2.41)$$

Thus, after multiplying the first equation by  $\epsilon$ , we get

$$\begin{aligned}\epsilon \frac{\partial u(x_1, t)}{\partial t} &= \epsilon^2 \frac{\partial^2 u(x_1, t)}{\partial x_1^2} + f(u, v) \\ \frac{\partial v(x_1, t)}{\partial t} &= \delta \epsilon \frac{\partial^2 v(x_1, t)}{\partial x_1^2} + g(u, v)\end{aligned}\quad (2.42)$$

where  $\delta = D_v/D_u$  is of the order of unity.

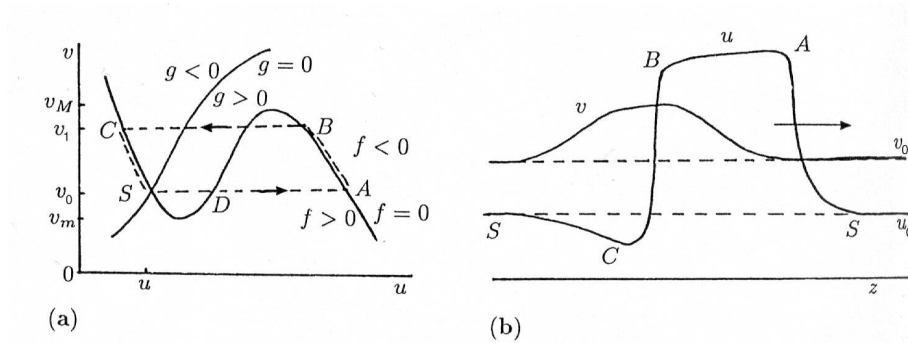


Figure 2.12: Pulse propagation in a two-component excitable system (singular perturbation approach). (a.) Phase-space of the concentrations. (b.) Concentration profiles [15].

The phase plane of the system shows that the concentration of  $u$  suffers more abrupt changes than  $v$  (fig. 2.12 (b.)). Moreover, if we perform the transformation

$$X = \frac{x_1 - ct}{\epsilon} \quad (2.43)$$

the change of  $v$  in the new coordinate  $X$  is so small, that it can be considered constant during the abrupt changes of  $u$ . As a consequence, its value  $v_0$  in the neighborhood of the frontal part of the pulse, where it begins to grow, can be regarded as being the same as far from the pulse,  $v_0 = v(X = \pm\infty)$ . The value of  $v$  can also be regarded constant around the 'front-back' where it reaches its maximum  $v_1$ . Thus, in these regions the diffusion coefficient of  $v$  can be neglected, and (2.42) reduces to

$$u''(X) + cu'(X) + f(u(X), v_0) = 0, \quad u(\pm\infty) = U_{\pm}(v_0) \quad (2.44)$$

By using Kanel's theorem, we obtain the relation plotted on fig. 2.13 between the concentration of  $v$  and the speed of the appropriate regions of the pulse. The 'back' of

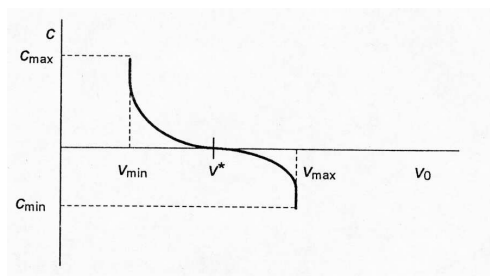


Figure 2.13: Speed of a pulse, as a function of  $v_0$ , in the singular perturbation approach [8].

the pulse can be regarded as a front that is "retreating" in the positive direction (a front having negative speed). By analyzing figs. 2.13 and 2.12 (b.), it can be shown that a pulse will have a constant thickness.

The initiation of a wave train built up by several pulses does not take place spontaneously. According to our present knowledge, most probably the pulses start from a pacemaker region where an external perturbation is present. This can be an impurity, or a deliberate disturbance. The  $T$  bursting period length of a pacemaker region does not depend on the properties of the excitable media, which determines only a lower cutoff  $T_{min}$ .

Note that in theoretical investigations of wavetrains we disregard the irreversible changes of the medium; the rising of the lowest value of  $v$  in between the "waves" of a wavetrain is not caused by the depletion of the reactants, but only by the lack of time for recovery. A relation similar to 2.24 can be deduced between the extremal concentration values  $v_0, v_1$  and the period  $T$ . The wavelength of the pattern can be calculated by the well-known formula  $\lambda = cT$ .

An interesting relation can be deduced between the speed  $c$  of the waves generated by a pacemaker, as a function of its bursting period  $T$ . Since the attrition of the media is neglected, the lowest value of the compound  $v$  in between the "waves" of a wavetrain will be determined by the period  $T$ . For higher  $T$  a more complete recovery (smaller value of  $v$ ) will be achieved that, according to fig. 2.13, leads to a higher speed.

Recently, the following relation has been deduced for systems like (2.40) [81, 82].

$$c(T) = c_0 \cdot \tanh\left(\frac{T}{T_*}\right) \quad (2.45)$$

where  $c_0$  is the speed of a single pulse traveling in an unperturbed media, and  $T_*$  is a chemical timescale that can be calculated from the model.

Chemical waves can also spread in two or three-dimensional excitable media. In these cases a new effect appears, namely the dependence of the wave velocity on the shape of the wave itself. The mathematical form of this coupling is given by the eikonal equation [19, 25]:

$$c_N(R) = c + D_u K \quad (2.46)$$

where  $c_N(R)$  is the normal component of the speed,  $c$  is the velocity of the plane wave,  $K$  the curvature and  $D_u$  the diffusion coefficient of the autocatalytic species  $u$ . Thus, a concave wave has greater speed than a convex one. The explanation of this phenomenon lies in the fact that the autocatalytic species of a convex front becomes more diluted [83], since it has to diffuse into a larger field than in the case of a straight or a concave front. This relation has great importance in the theoretical investigation of spiral waves.

The most common patterns in excitable media are the rotating spirals. Spiral waves are extremely stable patterns, their shape and rotation frequency are uniquely determined by the properties of a given excitable medium. In the middle of the spirals there is a region called the *core* where no front propagation takes place.

If we start with the initial conditions in the form of a front segment or broken circular pulse, the wave tips begins to sprout, simultaneously curling, and finally give rise to spiral waves [15]. Spiral waves will build up in the case of random initial conditions as well. They do not require the presence of a pacemaker region as the target patterns. Some examples of spiral waves are presented in figure (2.14).

### Wavetrains in Oscillatory Media

Trigger waves spreading in oscillatory media are called *phase diffusion waves* [62]. It is believed that they are also generated by foreign pacemaker regions, where the rate of reaction is accelerated compared to the immediate neighborhood. Due to this difference in reaction rates, there are established differences in the phase of oscillations, equivalent to differences in concentrations. The concentration differences spread through diffusion, and thus phase diffusion occurs [5].

There are several differences between waves in excitable and oscillatory media. The concentration gradients are much shallower in phase diffusion waves. Unlike in excitable systems, a single pulse cannot survive in oscillatory media: pulses in oscillatory media are erased by the background oscillation, *i.e.* each oscillatory cycle may "kill" one pulse. However, wavetrains generated by pacemakers, or autonomous rotating spirals are stable.

Because of experimental difficulties, phase diffusion waves are not as "popular" as waves in excitable media [85, 86]. We do not enter into the details of their theory.

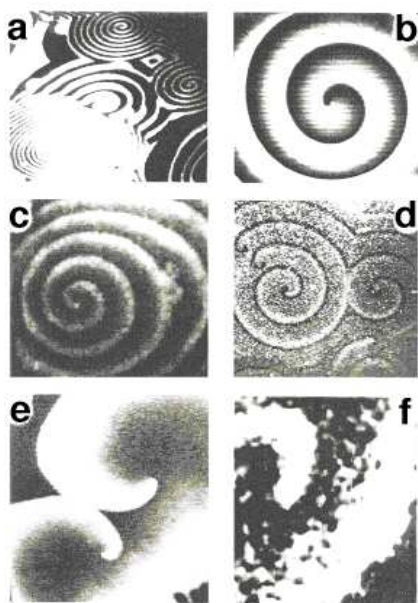


Figure 2.14: Examples of spiral waves in excitable media. (a.) Population of spiral waves with different rotation periods and wavelengths in the catalytic CO-oxidation on a platinum surface, visualized with photoemission electron microscopy (PEEM). Image area:  $450 \times 400 \mu\text{m}$ , rotation period of spirals with intermediate wavelength 20 s (from Nettesheim et al., 1993). (b.) Spiral wave in the Belousov-Zhabotinsky reaction. The distribution of light intensity reveals the front of oxidized cerium catalyst at 344 nm as a black band moving through a reduced solution layer of 0.7 mm thickness (bright background). Wave length: 2.1 mm; rotation period 40 s. (c.) Spiral  $\text{Ca}^{2+}$ -wave pattern observed in *Xenopus laevis* oocytes (wavelength 60  $\mu\text{m}$ , period 3 s). IP3-mediated  $\text{Ca}^{2+}$ -release is detected by confocal laser scanning microscopy (from Lechleiter and Clapham, 1992). (d.) Aggregation of social amoebae in the cellular slime mold *Dictyostelium discoideum* observed in dark field-optics. In bright areas cells move chemotactically towards the spiral core, while in dark bands no directed cell migration is found. Wavelength 2.5 mm; rotation period 7 min (taken from Foerster et al., 1990). (e.) Colliding spiral-shaped front in neural tissue: These "spreading depression" waves on chicken retina are visualized by white light scattered in zones of increased turbidity. (f.) Clock-wise rotating wave in a slice (20 x 20 x 0.5 mm) of isolated canine cardiac muscle. Visualized by use of a potentiometric dye (with fluorescence excited at 490 nm; measured at 645 nm). Rotation period: 180 ms (from Davidenko et al., 1992) [84].

Here we just mention that so-called *lambda-omega models* and *amplitude equations* are adequate for their handling [15, 21].

## 2.2 Precipitation and Solidification Processes

### 2.2.1 The Liesegang Phenomenon

Pattern formation can also emerge behind moving fronts that "activate" the field they sweep through. In the *Liesegang phenomenon* [117] a rhythmic precipitate forms in the wake of the diffusion front of electrolyte  $A$  that penetrates into a gel containing

electrolyte  $B$  [13, 118–121]. The observed precipitation patterns usually consist of a set of bands, rings or spherical shells (depending on the geometry of the system) clearly separated in the direction perpendicular to the motion of the front (fig. 2.15). Note that the gel is required in order to prevent convection and to keep the colloidal precipitate where formed. It can also affect the nucleation and growth processes [119, 122]. In most cases the empty space between consecutive bands increases (*normal banding*), but in some cases it decreases (*inverse banding*). However, up to this time (2004) no inverse Liesegang banding has been reproducibly obtained, although its emergence has been reported in several cases [13, 123–125]. Inverse banding of  $\text{NaOH} + \text{CuCl}_2$  in agarose gel described in [13] does not form via a Liesegang-like mechanism, while that of  $\text{NaOH} + \text{MgCl}_2$  in PVA gel could not be reproduced using very pure water supplied by Millipore and Labconco filter series. My attempts to reproduce the inverse bandings reported in [123] and [124] also failed. Finally we mention that *irregular banding* refers to the random distribution of precipitate regions.

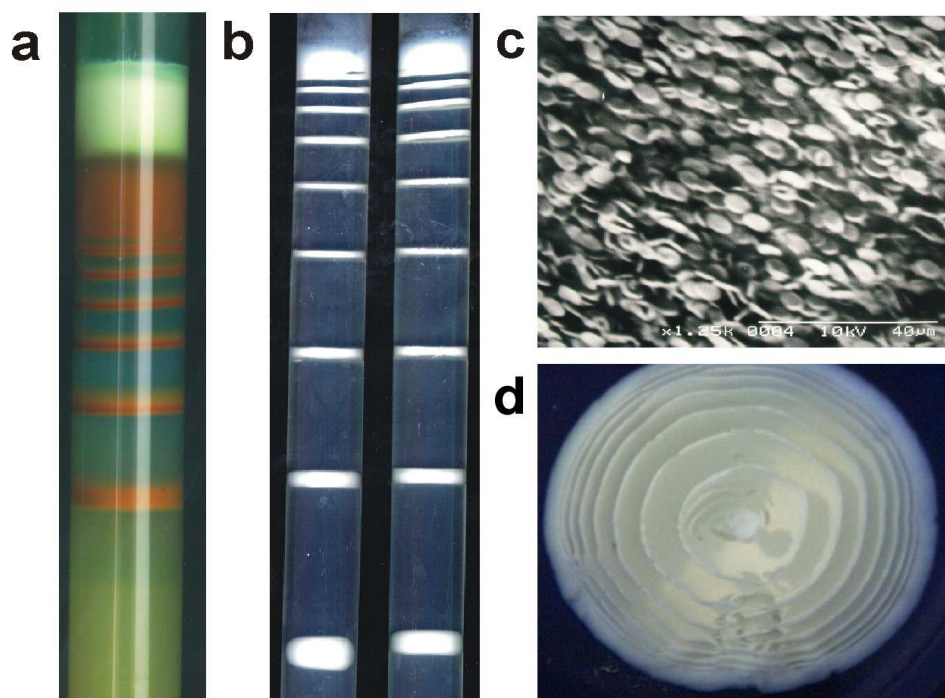


Figure 2.15: Liesegang banding of (a.)  $\text{CuCl}_2 + \text{K}_2\text{CrO}_4$  system in silica gel column, and (b.) that of  $\text{NH}_4\text{OH} + \text{MgCl}_2$  system in PVA gel column. (c.) Picture taken with Environmental Scanning Electron Microscopy of the colloidal particles that build up a Liesegang band formed in the experiment on panel (b.) [13]. (d., courtesy of Prof. M. Zrínyi) Cross-section of Liesegang shells of  $\text{NH}_4\text{OH} + \text{MgCl}_2$  system in PVA gel.

Although the Liesegang phenomenon has been studied for over a century since its discovery in 1896 [117], the mechanisms responsible for these structures are still under discussion. The models that try to explain the pattern formation can be divided

into three main classes: *supersaturation*, *sol coagulation* and *phase separation* theories. All of these theories can reproduce the most important macroscopic characteristics of the bandings, but none of them is able to explain all the experimental findings. It is reasonable to assume that several mechanisms account for the Liesegang banding.

### Supersaturation Theories

Supersaturation theories represent the simplest model of the Liesegang banding [118, 126, 139]. The basic idea of the supersaturation theories has been worked out by Wilhelm Ostwald around 1900, shortly after the discovery of the Liesegang phenomenon [126]. The model is based on the observation that saturated solutions do not precipitate. In order for precipitation to start, the concentration of the dissolved matter has to reach the so-called nucleation threshold, *i.e.* the solution has to be supersaturated.

According to the simplest version of these models, the formation of precipitate bands takes place as follows. When the *outer electrolyte A* penetrates into the gel containing the inner electrolyte *B*, the ion-product at the top of the gel column gradually grows, and finally reaches the critical value required for nucleation. At this point a large amount of colloidal particles are formed. Since the ion product is still high, and the growth of the particles requires only a very low value of the ion product, the particles will grow very fast. Thus, the growing particles deplete their surroundings where the ion product used to be about as high as the nucleation product. As the diffusion front of the outer electrolyte passes over the depleted domain, and moves into gel regions with high inner electrolyte concentration, the ion product in the wake of the front increases again. As a consequence, the precipitation process will restart in a new place. As it will be shown later, supersaturation theories are able to reproduce in a simple way the most important macroscopic characteristics of the normal banding.

This model was formulated mathematically, and investigated through approximative (semianalytic) methods for the first time by C. Wagner, who found that the model is able to reproduce the rhythmic banding [127]. Wagner's theory was improved and simplified by S. Prager [128], as well as T. Antal and Z. Rácz [118].

Here we present in detail some semianalytic results of the simplest supersaturation model presented in [118], where the outer electrolyte *A* and inner electrolyte *B* react to form precipitate *C* when the ion product  $ab$  reaches the nucleation product  $I_0$ . Initial concentrations of the reactants are  $a_0$  and  $b_0$ . It is also assumed that the critical ion product necessary for the growth of the already formed precipitate is negligible. The outer electrolyte is supposed to be of sufficiently high concentration that the effect of depletion due to band formation on its profile is negligible. Depletion of the inner electrolyte has been taken into consideration by fixing to zero its value at the last band. The precipitate *C* cannot diffuse at all.  $\lambda$  and  $\gamma$  are reaction rate constants having large values in order to deplete *B* when a precipitate band forms.

The equations of the model are the following [118]:

$$\begin{aligned}\frac{\partial a(x,t)}{\partial t} &= D_a \frac{\partial^2 a(x,t)}{\partial x^2} - \gamma \Theta(a(x,t)b(x,t) - I_0) - \lambda a(x,t)b(x,t)c(x,t) \\ \frac{\partial b(x,t)}{\partial t} &= D_b \frac{\partial^2 b(x,t)}{\partial x^2} - \gamma \Theta(a(x,t)b(x,t) - I_0) - \lambda a(x,t)b(x,t)c(x,t) \\ \frac{\partial c(x,t)}{\partial t} &= \gamma \Theta(a(x,t)b(x,t) - I_0) + \lambda a(x,t)b(x,t)c(x,t)\end{aligned}\quad (2.47)$$

The concentration profiles are approximated by

$$a(x,t) = a_0 \left( 1 - \frac{x}{\sqrt{2D_a t}} \right) \quad (2.48)$$

and

$$b(x,t) = \frac{b_0}{\sqrt{2D_b(t-t_N)}}(x - X_N) \quad (2.49)$$

where  $X_N$  is the position of the band  $N$ , and  $t_N$  is its time of appearance (fig. 2.16).

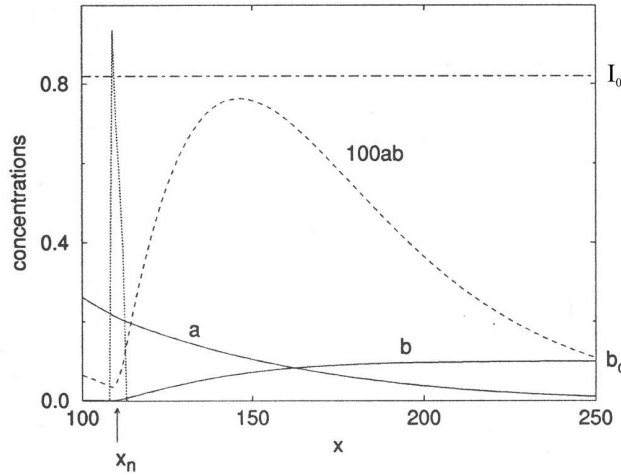


Figure 2.16: Concentration profiles in the supersaturation theory of the Liesegang banding (computer simulation, adopted from [118]).

The condition for the band  $N + 1$  to appear is

$$a(X_{N+1}, t_{N+1})b(X_{N+1}, t_{N+1}) = I_0 \quad (2.50)$$

After performing the calculations and applying the asymptotic approximation

$$\frac{X_{N+1}}{X_N} \approx \frac{X_N}{X_{N-1}} = 1 + p \quad (2.51)$$

we obtain the *spacing law* [131]

$$X_N \sim (1 + p)^N \sim \exp(N \ln(1 + p)) \quad (2.52)$$



as well as the *time law* [132]

$$K = \frac{X_N}{\sqrt{t_N}} \quad (2.53)$$

and an approximate form of the *Matalon-Packter law*, that connects the spacing constant  $p$  to the initial concentrations of the reactants [129, 130]

$$p \approx 0.02 + \frac{\alpha}{a_0 b_0} \quad (2.54)$$

where  $\alpha$  is a constant depending on the parameters of the model.

The theory at the next level of complexity assumes that the  $A + B$  reaction yields the precipitate  $C$  through an intermediate compound  $M$ . This compound is supposed to be produced continuously, with a certain rate proportional to the local concentration product of the reactants, and precipitates when its concentration exceeds a threshold  $M^*$ . The precipitate  $C$  is able to grow by collecting the neighboring  $M$  [118, 133]. Beside the time, spacing and Matalon-Packter laws, similar “nucleation and growth” models are able to reproduce the *width law*, giving the thickness of the rings, as well [133]:

$$W_n \sim X_N^\alpha, \quad \alpha > 0 \quad (2.55)$$

Here we mention that supersaturation theories were implemented by a cellular automata approach, that also led to the correct form of the time, spacing and width laws [134].

The above-mentioned theories do not allow the presence of the precipitate in the space in between the precipitate bands. However, rhythmic banding was observed in the experiments performed by E. Hatschek and S. Gosh, where, before starting the experiments, small crystallites of the precipitate were homogenized in the gel [135, 136]. According to the previous theories, these could prevent the reaching of the critical ion-product  $I_0$ , and the threshold  $M^*$ , respectively. Moreover, according to the experiments of M.E. LeVan and J. Ross, performed in the usual way, precipitate can exist in the region in between the bands as well [137].

An advanced “nucleation and growth”-type model, worked out by G.T. Dee is able to reproduce a small amount of precipitate in between the bands. In this approach, the threshold at  $M^*$  is not sharp any more, but it is deduced from the theory of nucleation [138]. The results of this model may also answer why pattern formation occurred in the experiments of Hatschek and Gosh: the number of the critical nuclei emerging when the nucleation threshold is reached, is huge in comparison with the amount of the crystallites present in the gel. Therefore, the overall surface of the crystallites may not be enough to initialize a considerable amount of heterogeneous nucleation.

### Sol Coagulation Theories

Albeit the successes of the supersaturation theories, there are a plenty of experimental findings, they are unable to explain. As follows, we present the most relevant of these results.

Hedges and Henley managed to obtain rhythmic banding by an unusual method. First a colloidal sol was prepared by reacting two electrolytes. This sol was homogenized in the gel phase of the experimental setup. Later, one of the electrolyte solutions was poured on the top of the gel column. In a certain concentration range, a series of precipitate bands emerged, although no chemical reactions were going on in the system (fig. 2.17). The experiment suggested that the formation of the precipitate bands may be concerned with a secondary process, occurring after the reaction [144]. Similar experiments have been performed by Flicker and Ross as well [145].

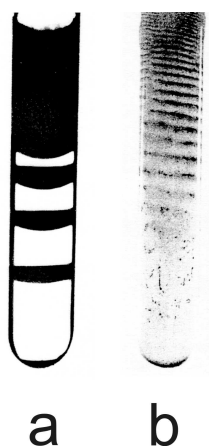


Figure 2.17: Precipitate bands resulting from sol coagulation without chemical reactions. (a.)  $PbI$  sol coagulated with  $Pb(NO_3)$  solution. (b.)  $Mg(OH)_2$  sol coagulated with  $NH_4OH$  solution [144].

Results of a series of experiments, performed by S. Kai, S.C. Müller and J. Ross, also supported the assumption that the precipitate bands build up from a previously formed colloidal sol [141]. In these investigations, the bands were produced by reacting  $NH_4OH$  highly basic outer electrolyte with  $MgCl_2$  inner electrolyte, the latter being previously homogenized in gelatine gels. The changes of the  $pH$ , indicating the advent of the outer electrolyte, were made optically observable by introducing an indicator solution into the gel phase. In order to investigate the precipitation processes going on in the gel, a laser beam was passed through the gel column at different locations after the reactions had been started. Scattering, transmission and deflection of the laser beam were all measured. According to the experimental results, the light scattering was enhanced in the wake of the diffusion front of the outer electrolyte, defined by the  $pH = 9$  front (fig. 2.18). This can be interpreted as a consequence of the appearance of a colloidal sol. Moreover, the deflection of the light beam can be assigned to the significant growth of the volume fraction of the colloidal particles at those regions where later the visible precipitate regions appear.

Several experiments were performed in order to explore the effect of gravity on the characteristics of Liesegang banding [141, 149]. The investigations where the gel columns were located in different orientations while the experiments were running, showed that

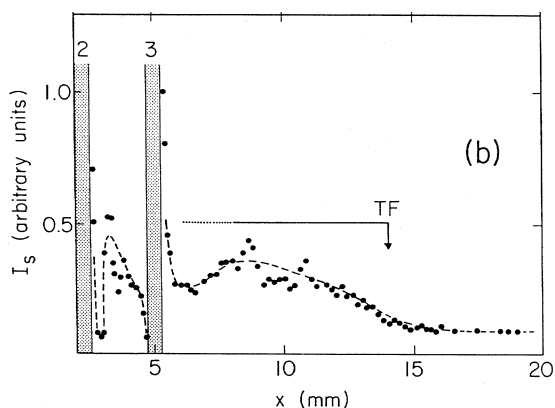


Figure 2.18: Plot of the scattered light intensity along the gel column [141].

the spacing coefficient  $p$  is greatest in the “normal” setup when the outer electrolyte diffuses downward, and it is smallest in the reverted position when it has to diffuse upwards. Since the effect of the gravitational force on the diffusion of the ions can be neglected, this experiment also indicates the presence of a colloidal material which acts as a precursor to precipitate bands.

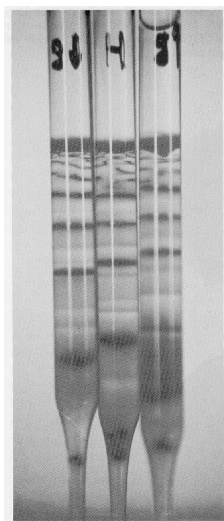


Figure 2.19: Effect of gravity on Liesegang band formation [119]

Sol coagulation models [118, 140, 141] assume that the formation of the colloidal bands takes place in two steps. First, a colloidal sol is formed that cannot be observed by the naked eye, and later the bands arise from the coagulation of the sol. Sol formation takes place when the outer electrolyte penetrates into the gel, and the nucleation threshold is reached. The size of the sol particles is assumed to be so small that the gel does not inhibit their diffusion. Theoretical predictions indicate that, for a broad class of reactions, the sol concentration has to be constant in the wake of the outer

electrolyte's diffusion front [142, 143]. Since the sol, after it has been formed, is electrostatically stabilized [166], it cannot coagulate into big colloidal particles. However, as the outer electrolyte concentration increases at certain points in the gel column, the overall ionic strength of the electrolytes at that point also increases. The model assumes that the coagulation of the sol, and thus the formation of the visible precipitate bands, takes place when the ionic strength reaches the *critical coagulation concentration*, and the sol concentration is also above a critical value. Once a precipitate band is formed, the sol particles are carried by diffusion and incorporated into it. Thus a depleted zone is formed, where the amount of sol particles is significantly reduced. In order to start the formation of a new band, the diffusion front of the outer electrolyte has to overtake the depleted region.

Earliest versions of the sol coagulation theories have been elaborated by N.R. Dahr and A.C. Chatterjee at the beginning of 1920's [146, 147]. They were investigated using computer simulations first time by A. Büki [140], and it turned out that they correctly reproduce the time and spacing laws. This has also been demonstrated by semianalytic calculations [118].

However, there are several experimental findings that cannot be satisfactory explained either by supersaturation, or by sol coagulation approaches. According to the computer simulations of the above models, only one precipitate region develops at a time. Experiments performed by H. Higuchi and R. Matura indicated the contrary [148]. In their experiments,  $NH_4OH$  outer electrolyte was reacted with  $MnCl_2$  or  $Mg(SO)_4$  inner electrolytes homogenized in agar-agar gels. Several maxima of the metal ion concentrations were found ahead of the last precipitate band that appeared, in those places where precipitate regions appeared later in the experiment (fig. 2.20). We emphasise that here the *overall* ion concentration was measured, that is, the proportion of the ions in precipitate and in solution is unknown.

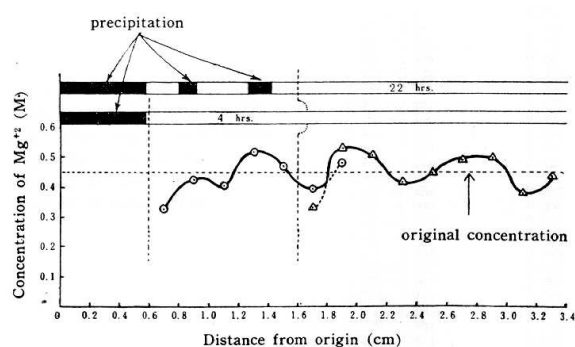


Figure 2.20: Distribution of  $Mg^{2+}$  ions in the gel at 4h and 22h after the starting or the experiment [148].

Thus, we can drive the conclusion that all the aspects of Liesegang band formation are not clarified. It's likely that most of the chemical systems have got particular properties. At this time, experimental data necessary for the construction of more

powerful theories is missing as well.

### Phase Separation Theories

Recently a new scenario has been proposed by Z. Rácz and co-workers for modeling the formation of Liesegang patterns [153]. In this approach, the formation of bands is explained by a spinodal decomposition scenario.

The model assumes that, due to the reaction of the outer electrolyte  $A$  and the inner electrolyte  $B$ , an intermediate compound  $M$  is formed. For a broad class of reactions [143], this compound has a constant density  $m_0$  behind the diffusion front of the outer electrolyte. Furthermore, it is assumed that that the compound  $M$  can undergo phase separation [150, 151]. The pattern formation is described by the Cahn-Hilliard equations plus a source term  $S$  representing the production rate of the compound  $M$  by chemical reactions:

$$\frac{\partial m(x, t)}{\partial t} = -\lambda \frac{\partial^2}{\partial x^2} [\epsilon(m(x, t) - m_*) - \gamma(m(x, t) - m_*)^3 + \sigma \frac{\partial^2}{\partial x^2} (m(x, t) - m_*)] + S(x, t) \quad (2.56)$$

Note that the parameter  $m_*$  can be included into  $\epsilon$ . In numerical simulations, the source term can be supplied by the simultaneous solving of the  $A + B \rightarrow M$  reaction with appropriate initial and boundary conditions.

If the concentration  $m_0$  is in the unstable regime (in between the  $m_s$  “spinodal point” and  $m^*$ ), some time after the front has swept over a certain point, the separation of  $M$  into high  $m_+$  and low  $m_-$  density phases will take place. The high density regions appear as precipitate bands, while the low density ones as empty spaces in between. The model yields by simple semianalytic calculations to the time, spacing, Matalon-Packter and width laws as well [153].

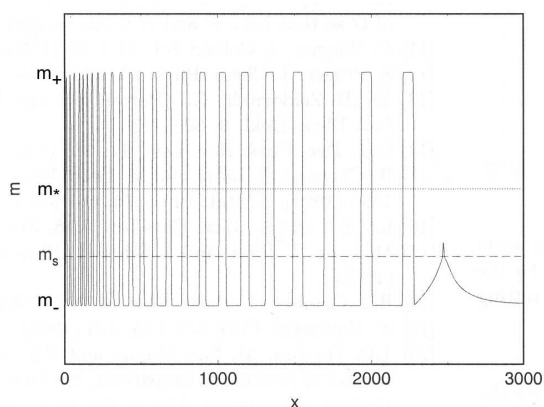


Figure 2.21: Liesegang banding produced by a phase separation model (computer simulation, adopted from [152]).

Since three of the parameters (*e.g.*  $\lambda$ ,  $\gamma$  and  $\sigma$ ) can be used to set the time and length scales, as well as the concentration scale, only one free parameter,  $\epsilon$  remains in the model, apart from  $m_0$ , the initial concentrations  $a_0, b_0$  and diffusion constants  $D_A, D_B$ . Consequently, one has a theory with a small number of parameters<sup>2</sup> in comparison with previous ones dedicated to model the Liesegang banding (fig. 2.21).

More advanced versions of the model include noise effects as well. Beside the main laws of the Liesegang banding, these also show the presence of precipitate grains in between the bands [154].

## 2.2.2 Dendritic and Seaweed Solidification

Several forms of crystallization lead to nontrivial and beautiful shapes. Some of the crystals are *faceted* resembling a polyhedral structure, but more complex *dendritic* and *seaweed* structures can also emerge [4, 87–90]. Dendrites are anisotropic ramified structures with nearly paraboloidal growing tips, while seaweed-like morphologies are more isotropic, composed (in 2D) of *doublons* that are double-finger like structures separated by narrow channels [91]. A combination of dendritic and faceted growth are the snow crystals [92, 93].

Solidification proceeds in the following sequences: (1.) Atoms to be crystallized are transported to the crystal surface. This process is important when the crystal grows from a solution [94], since in the case when the growth occurs in an undercooled melt, no chemical transport processes are required. (2.) Atoms are incorporated in the crystal. (3.) The released latent heat is transported away from the surface. The growth as a whole is governed by the slowest process [4].

Faceted crystals are formed when the surface nucleation (*i.e.* formation of undissociable atom clusters on the surface of the solid) occurs with a very low probability, and therefore the surface of the crystal is smooth on molecular level. In this case the kinetic process is the slowest, and the growth is limited by the kinetics of incorporating new elements. The shape of a growing faceted crystal can be estimated by a modified Wulff construction, where the orientation-dependent growth rate should be used instead of the surface free energy of the respective planes [95, 96].

The situation changes if the surface becomes rough on the molecular level, that is when the *roughening transition* occurs [4, 87, 97]. Two kinds of such transitions are known. In the case of *thermal (thermodynamical) roughening* the surface undergoes a phase transition at a roughening temperature  $T_r$ . The growth can be driven in the "rough" region by increasing the temperature. *Kinetic roughening* occurs when the driving force is very high (that is the undercooling is high when the crystals are grown from melts, and the supersaturation is high when they are grown from a solution), even if the temperature of the surface is below  $T_r$  [97–99]. In the following, we will regard only the case when the crystals are grown from a melt.

---

<sup>2</sup>In the framework of this theory, we cannot assign the compound  $M$  with a diffusion coefficient in the classical sense.

After the roughening transition there is practically no nucleation barrier, there are a lot of surface fluctuations and the interface is rough at the molecular level. It can be shown that the kinetics are very fast, and that the growth is limited by the transport of latent heat and also on chemical diffusion in the case of growth from solutions. There are no facets, but dendritic and seaweed-like crystallization occurs, that will be our concern in the following paragraphs.

The first analytical results in this field were obtained by Ivantsov in 1947, when it was proved that in the case of zero surface tension, for any value of the undercooling,  $\Delta$ , a continuous family of steady state solutions exists, having parabolic shape [4, 100]. The product of the tip radius  $R$  and the velocity  $v$  is constant, *i.e.*  $Rv = f(\Delta)$ . However, in real systems, more complex dendrites and seaweed structures are observed (fig. 2.22).

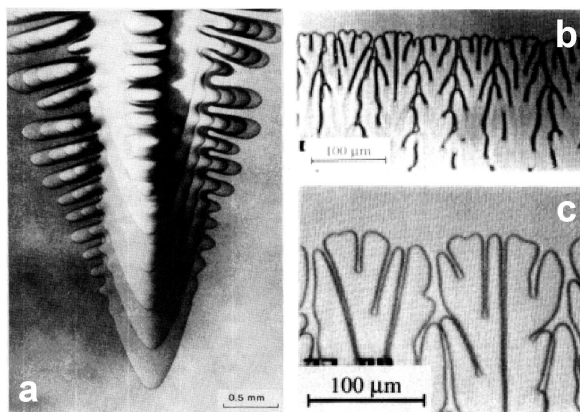


Figure 2.22: (a.) Multi-exposure photograph of a succinonitrile dendrite [1] (b.) Seaweed pattern of  $CBr_4 - 8\%C_2Cl_6$ , in a nearly  $[1,1,1]$ -oriented crystal. (c.) Enlarged view of a seaweed pattern [106].

The problem of dendritic growth has been solved after significant experimental and theoretical research. Experimental investigations showed that for a given undercooling, the same dendrite (*i.e.* same tip velocity and radius of curvature) is reproducibly observed. This implied a “selection problem”: for a certain undercooling, the Ivantsov solution allows a continuous family of parabolic solutions, but for specified conditions, only one shape is observed.

In addition, the Ivantsov solution is linearly unstable, and it ceases to exist if surface tension is switched on, even if this surface tension is very small [4, 100]. In the mid 80’s experimental and theoretical procedures demonstrated that surface tension anisotropy was the missing ingredient in the formulation. For a given anisotropy, instead of a continuous family of parabolas, only a discrete set of solutions (with close to parabolic shape) are selected, giving rise to a “microscopic solvability” criterion. It turned out that only the fastest needle of this discrete set is linearly stable, *i.e.* the one that is observed in experiments and dynamical computer simulations [4, 91, 100, 101]. Later it was demonstrated that the anisotropy of the so-called kinetic coefficient can also determine the selection of dendrites [102].

Small fluctuations, which are unavoidably present because of random molecular motion or small inhomogeneities, cause small sidebumps to become selectively amplified by a Mullins-Sekerka like mechanism (the Mullins-Sekerka instability will be discussed below). Shortly after birth, daughter needles compete for nourishment and only a finite fraction survive to grow into larger needles that can themselves generate other offsprings. Thus, a highly hierarchical branched structure, a dendrite, will form.

In the mid 90's it was demonstrated that there is a stable stationary solution even at isotropic surface tension, being not a needle, but a double finger called a doublon [103–106]. Doublons are the basic elements of the seaweed structures.

Here we mention that in some cases the formation of fractal structures is expected. In order to anticipate these conditions, two characteristic lengths have to be introduced, namely the capillary and the diffusion length. The capillary length is  $l_c = \frac{\sigma T_M C_p}{L^2}$  ( $\sigma$  is the surface tension,  $T_M$  the melting temperature of a flat interface,  $C_p$  the heat capacity of the liquid phase, and  $L$  the latent heat). The diffusion length is  $l_D = \frac{2D_l}{v}$  where  $D_l$  is the heat diffusion of the liquid, while  $v$  is the growing speed of the solidification front. Large capillary length inhibits small protrusions from growing, whilst a small diffusion length means that the growth is not diffusion-limited, and heat gradients (the driving forces) are not much higher at the top of the protrusions. As a rough estimate we can say that fractal structures form when the size of the growing object is between the capillary and diffusion length,  $l_c \ll l \ll l_d$ , there is some noise in the system, and the anisotropy of the surface tension is very small [105, 107]. The diffusion length has to be much greater than the capillary length, since the scaling relation  $N(\epsilon) \sim \epsilon^{-d}$ , where  $d$  is the fractal dimension and  $N(\epsilon)$  the smallest number of balls with radius  $\epsilon$  that is necessary to cover the object, has to be valid over several orders of magnitude. Note that sidebranches of dendrites may also have some scaling properties [108, 109].

In the following, the simplest approach is briefly introduced, which includes surface tension, an effect having a strong influence on pattern formation (Mullins-Sekerka Instability) [4, 91].

In this calculation the stability of a planar solidification interface is analyzed, traveling with an arbitrary constant speed  $v_0$  into a undercooled melt, where the magnitude of the dimensionless undercooling  $\Delta = \frac{T - T_M}{L/C_p} = 1$ . Let us also assume that the surface of the growing crystal is rough. The equations of this model are the following:

$$\begin{aligned}
 \left. \frac{\partial u(x, y, t)}{\partial t} \right|_l &= D_l \Delta u(x, y, t)|_l \\
 \left. \frac{\partial u(x, y, t)}{\partial t} \right|_s &= D_s \Delta u(x, y, t)|_s \\
 u(x, y, t)|_{front} &= -l_c \kappa \\
 v_n &= D_l [\beta (\nabla u(x, y, t))_s - (\nabla u(x, y, t))_l] \cdot \vec{n}
 \end{aligned} \tag{2.57}$$

Here  $u(x, y, t)$  is the dimensionless temperature field,  $D_l$  and  $D_s$  the thermal diffusivities in the liquid and the solid phases, and  $v_n$  is the normal velocity of the interface that can differ from the average front propagation velocity  $v_0$ . The capillary length is denoted



by  $l_c$ ,  $\kappa$  is the curvature of the interface and  $\beta$  is a constant related to heat capacities and heat diffusion coefficients of the liquid and solid phases.

After carrying out a linear stability analysis of the above equations, the dispersion relation of the instability has the form of

$$\Omega(k) = v_0 k \left( 1 - \frac{D_l}{v} l_c k^2 (1 + \beta) \right) \quad (2.58)$$

*i.e.* the interface is unstable to sinusoidal perturbations at all length scales above a critical wavelength [110].

It has to be mentioned that at high undercooling when  $\Delta > 1$  the local equilibrium is not valid, one has to add a kinetic term in the description restricting the speed [111]. At  $\Delta < 1$  there is no stationary flat solution, the front slows down as the square root of time, but the Mullins-Sekerka dispersion relation with the current front speed can still be used.

Note that in the case of the quasi-steady growth of a sphere into an undercooled liquid with an arbitrary undercooling  $\Delta$ , a unique speed  $v = \frac{\partial R}{\partial t}$  is selected, which is a function of the radius [4].

## 2.3 Other Growth Processes

Several other types of growth phenomena can also yield nontrivial patterns. Destabilization of the growing surface, due to the Mullins-Sekerka mechanism in crystal growth, can also be caused by several other effects that enhance the growth of small protrusions of the surface. The most well-known examples are electrochemical deposition, and some polymerization processes (fig. 2.23) [107, 112–114].

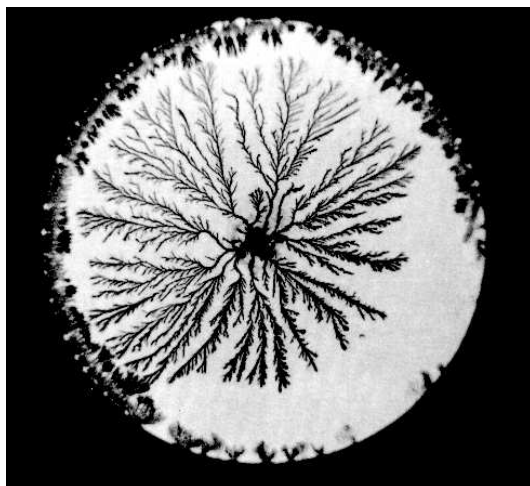


Figure 2.23: Polypyrrole aggregate grown through diffusion-limited polymerization [113].

Growth processes can be characterized by the mean of the number of collisions that occur before a particle can be added to the cluster. When it is almost certain that a

particle sticks to the cluster at the first collision, then the growth is limited only by the amount of material that is carried by a transport process to the growing cluster. This case will be referred to as *transport-limited growth*. If the situation is opposite, *i.e.* that particles are free to collide with so many sites that growth occurs at those places which are most favored by a low free-energy for deposition, the accretion is called *reaction (kinetics) limited growth* [107].

If the chemical diffusion is the relevant transport process of the system, the concentration field can be described by

$$D\Delta c(x, t) = \frac{\partial c(x, t)}{\partial t} \quad (2.59)$$

This kind of accretion is called *Laplacian growth* when it is very slow, and the time derivative term can be neglected, and it is termed *diffusion-limited growth* when the particle sticks to the cluster at the first hit.

A widely studied approach to the diffusion-limited growth processes represent the diffusion-limited aggregation (DLA) models. Here the cluster grows by the discrete aggregation of random walkers. In the so-called Witten-Sander DLA models only one diffusing particle is present in the system, introduced far from the cluster. If the particle collides with the cluster, it sticks and a new particle is introduced in the system [91]. In Finite Gas Density models the aggregate grows from a mother phase having a nonzero density  $n$  of particles, *i.e.* not only one diffusing particle is present in the system [4].

Diffusion-limited growth phenomena have been widely studied in the last decades because in some cases they yield fractal structures. The instability of the growth is caused by the fact that the gradient of the concentration field, and thus the probability of growth is enhanced at the tips, which screen the “fjords” of the cluster [113, 115]. Roughly speaking fractals grow when the surface tension is very small [112, 116], the anisotropy in the system is small [107], and the concentration in the mother phase is small [4]. All of these conditions hold for the Witten-Sander models. However, Finite Gas Density models lead to fractal structures only below the diffusion length  $l_D = \frac{2D}{v}$ , where  $D$  is the diffusion coefficient and  $v$  is the speed of growth.

Finally, we mention that in several electrodepositional patterning phenomena the electric field is relevant only very close to the cluster, and the problem can be considered as being limited by chemical diffusion. Fractal crystallization processes can also be regarded as diffusion-limited problems, where the temperature field obeys the Laplace equation outside the crystal, and new particles are added with greatest flux where the temperature is lowest.

## 2.4 Sea Shell Patterns

Pigmented mollusc shells show an enormous diversity of patterns (fig. 2.24). Since many molluscs live buried in the ground, perhaps no selective pressure on pigmentation exists and simply “Nature is allowed to play” [46].

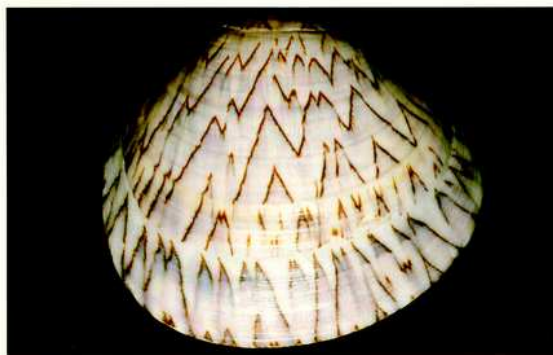


Figure 2.24: Shell patterns of *Lioconcha lorenziana* [46].

Shells consist of calcified material that is secreted by a specialized structure, the mantle. Animals increase the size of their shells by accretion of new material at the margin, the so-called *growing edge* of the shell [46].

Three types of models have been put forward to explain the formation of sea shell pigmentation patterns. *Cellular automata models* reproduce several patterns, but they make a minimal connection to the biological processes involved in pattern formation [15, 22]. *Neural models* assume that the neural net of the mantle has a determining role in the development of the pigmentation [15, 155]. *Reaction-diffusion models* suppose that a reaction-diffusion system governs the formation of the patterns [46, 156]. In the following paragraphs a short presentation of these latter models is given.

As mentioned above, the shell enlarges at the growing edge by the formation of a new layer of calcified material. The decorations of the shells result from the incorporation of pigments during the growth. Thus, the pattern is a time record of a process in the (more or less linearly arranged) cells of the mantle edge. According to the reaction-diffusion models the pattern-forming process in the pigmentation of the growing edge can be described by an activator-inhibitor or activator-substrate reaction-diffusion system.

One of the activator-substrate systems, studied in detail in [46], is:

$$\begin{aligned}\frac{\partial a(x, t)}{\partial t} &= D_a \frac{\partial^2 a(x, t)}{\partial x^2} + sba^2 - r_a a \\ \frac{\partial b(x, t)}{\partial t} &= D_b \frac{\partial^2 b(x, t)}{\partial x^2} + b_b(x) - sba^2 - r_b b\end{aligned}\tag{2.60}$$

where  $a$  is the activator,  $b$  is the substrate,  $D_a$  and  $D_b$  are their diffusion coefficients,  $r_a$  and  $r_b$  are the removal rates,  $s$  is the rate constant of the autocatalytic term and  $b_b$  is a production rate constant.

The model can exhibit a great variety of dynamics even without the diffusion terms: depending on the parameters, concentrations of the activator and substrate can periodically oscillate. Switching between two stable steady states due to a short temporary concentration change (bistability) can also be achieved. At certain parameter values, only a single stable steady-state exists.

If the diffusion coefficients  $D_a$  and  $D_b$  are nonzero, and some random noise is included in the initial conditions, then under certain parameters traveling waves (fig. 2.25), and stripes parallel or perpendicular to the growing edge can also emerge.

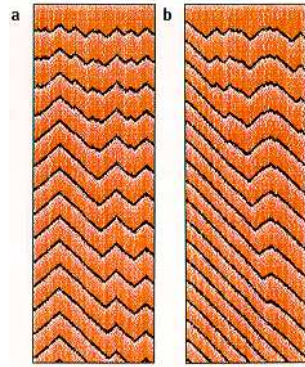


Figure 2.25: Traveling waves generated by the activator - depleted substrate system [46].

# Chapter 3

## Experimental Investigation of Primary Patterns

### 3.1 Preparation of the Experiments

#### 3.1.1 Sample Preparation

The experiments were performed either in poly(vinyl)alcohol (PVA) or in agarose hydrogels. These gels are neutral and easy to handle, and their cross-linking does not require any chemicals that could disturb the precipitation reactions.

##### The PVA Gel

PVA solution of 8.6  $w/w$  % was prepared by adding PVA powder (PVA 72000, Merck Z.S.) to high-purity water (supplied by Labconco and Millipore filter series) under continuous stirring at 70–80°C for 4 h, and then it was allowed to cool to room temperature.

The inner electrolyte concentration was set by adding to 100  $mL$  of the resulting PVA solution an appropriate amount of concentrated inner electrolyte solution. The acidity and degree of cross-linking of the gel were set by adding 2.00  $mL$  acid and 1.00  $mL$  of 1.0  $M$  glutaraldehyde (Merck Z.S.) to the above mixtures. Gels containing inner electrolyte  $CuCl_2$  were acidified with 18.50  $w/w$  %  $HCl$  (Reanal A.R.), while gels containing  $AgNO_3$  or  $Cu(NO_3)_2$  with 16.25  $w/w$  %  $HNO_3$ , respectively. High-purity water was used to top off the solution to 200.0  $mL$ . After strong mixing, the air bubbles were driven out by ultrasonication for 10 – 20  $s$ . The solution had to be placed in the experimental setup within 1 – 2 minutes, where the cross-linking took place (fig. 3.1). Note that the mesh size of 4.3  $m/m$ % PVA gel is about 150 Å.

##### The Agarose Gel

Agarose gel of 2  $w/w$  % was prepared by adding agarose powder (SeaKen low EEO or Sigma, low EEO) to high-purity water at room temperature (fig. 3.2). Solubilization was achieved by stirring for 1-2 min at 70 – 80°C. The inner electrolyte concentration

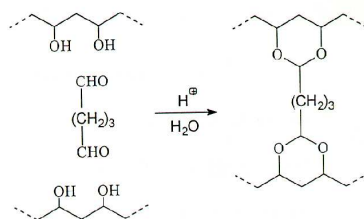


Figure 3.1: Cross-linking of the PVA gel.

was set by adding an appropriate amount of concentrated inner electrolyte solution of  $30 - 40^{\circ}\text{C}$  to  $100\text{ mL}$  of agarose solution. The amount of mixture was increased to  $200\text{ mL}$  using high-purity water at  $50 - 60^{\circ}\text{C}$ . Gelation took place when the mixtures were placed in the experimental setup, where they cooled down to room temperature. The mesh size of  $2\text{ m/m}\%$  agarose gel is about  $500\text{ \AA}$ . Note that in the case when the inner electrolyte was  $\text{AgNO}_3$ , the gelation process took longer, and at concentrations above  $1\text{ M}$ , did not take place at all [159].

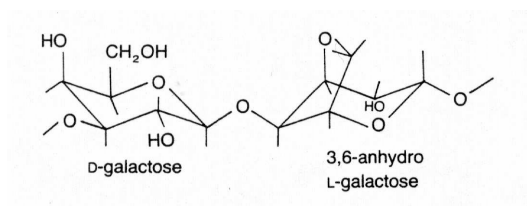


Figure 3.2: Monomer of the Agarose gel.

### 3.1.2 The Experimental Setup

Pattern formation has been investigated in gel sheets and gel columns in four main experimental arrangements. Two setups were found to be effective for doing experiments in gel sheets, and another two for investigations in gel columns (fig. 3.3).

For the first setup with gel sheets, the poly(vinyl)alcohol or agarose hydrogel having a thickness of  $0.2 - 0.3\text{ mm}$  and containing the inner electrolyte was located horizontally, between a microscope slide and a cover glass. Preparation of these samples was achieved by putting  $2 - 3$  droplets of the “gel solution” on a microscope slide and covering with a cover glass of about  $22 \times 32\text{ mm}$ . After  $1 - 3\text{ h}$  while the gelation took place, the reactions were started by placing  $4 - 5$  droplets of  $\text{NaOH}$  outer electrolyte solution (Reanal A.R.) on one of the edges of the gel sheet, and then covered with a cover glass to avoid evaporation.

In the second setup, the gel sheet was located vertically, between two glass plates being part of a protein electrophoresis device. For these types of experiments, the “gel solution” was poured between the plates to a height of  $40\text{ mm}$ . The  $83 \times 102\text{ mm}$  plates were previously purified with hot peroxy-sulphuric acid and fixed parallel to each other

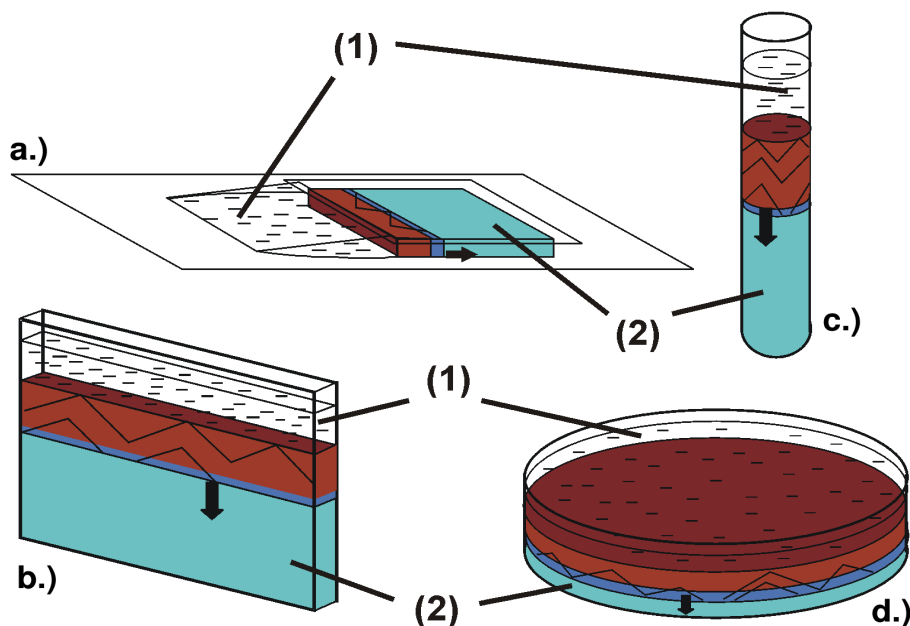


Figure 3.3: Experimental setups. The outer electrolyte is denoted by (1), while the inner electrolyte by (2). The arrows mark the direction of propagation of the precipitation fronts. (a.) The gel sheet containing the inner electrolyte is located between a microscope slide and a cover glass. The outer electrolyte is dropped to an edge of the gel sheet, and protected by another glass. (b.) The gel sheet is located between two glass plates (that belong to a protein electrophoresis device). The outer electrolyte is layered on the gel. (c.) The gel column is located in a test tube, and the outer electrolyte is poured on the top. (d.) The gel is located in a Petri dish, and the outer electrolyte is layered on the top. Note that in (c.) and (d.) (experiments in gel columns) the diffusion front of the outer electrolyte has the form of a disk.

at a distance of  $1.6 \text{ mm}$ . After  $10 - 20 \text{ h}$  the reaction was started by pouring  $3.00 \text{ mL}$  of  $\text{NaOH}$  outer electrolyte on the top of the gel.

In order to study the pattern formation when the outer electrolyte diffuses into a column-like setup, two arrangements have been developed. The gel is either located in test tubes having different inner diameters from  $d = 1 \text{ mm}$  to  $d = 40 \text{ mm}$ , or in Petri dishes. Most of the experiments have been performed in test tubes of  $d = 14.2 \text{ mm}$  and in Petri dishes of  $d = 87 \text{ mm}$  inner diameter. For the experiments in Petri dishes a  $5 - 7 \text{ mm}$ -high column of “gel solution” was poured and let to gelate in the dish. After  $10 - 30 \text{ h}$  the reactions were started by pouring a layer of about  $5 \text{ mm}$  of outer electrolyte on the gel. Due to the small height of the gel column, the reactions terminate in about 15 minutes. Samples in test tubes were prepared by pouring the “gel solution” in glass test tubes previously purified with hot peroxy-sulphuric acid. The experiments were started after  $10 - 30 \text{ h}$  by layering the outer electrolyte on the top of the gel. In order to avoid the depletion of the outer electrolyte during the experiment, its amount

(height) had to be at least 20 % of that of the gel column.

## 3.2 Formation of Primary Patterns in Gel Sheets

### 3.2.1 The Sequence of Pattern Formation

In this section the formation of the so-called *primary patterns* is investigated. Primary patterns in gel sheets are built up of some basic elements. By understanding the development of these constituents, we can also interpret the formation of the more complex shapes which emerge in gel columns.

In the usual case, pattern formation in the  $NaOH + CuCl_2$  reaction in gel sheets evolves in the following way (the concentration of the outer electrolyte will be denoted by  $a_0$ , while that of the inner electrolyte with  $b_0$ ):

The diffusion front of the  $NaOH$  outer electrolyte is followed by a sharp precipitation front (fig. 3.4 (a)). The precipitate that forms at this front looks blue in reflected and green in transmitted light, and shows no structure when investigated with optical microscopy; it is assumed to be mainly  $Cu(OH)_2$  [163–165]. Although there can be a large field behind the diffusion front of the  $NaOH$ , formation of the solid phase is taking place only at the sharp precipitation front, that will be referred also to as the *active border* of the precipitate area. Note that the active borders are permanently renewing surfaces.

If some impurities or inhomogenities are present on the gel surface or inside the gel, the precipitation may not start or may cease at these points. As the staggered precipitation front proceeds, these centers expand into wedge-like regions free of precipitate (fig. 3.4 (b.)). The reaction does not proceed on the oblique borders that separate the already formed precipitate from the wedge-like empty regions. These stationary surfaces are referred to as the *passive borders* of the precipitate region.

As the precipitation front segments sweep through the gel sheet, their length diminishes. Therefore, their margins are referred to as regressing edges (fig. 3.4 (b.)). At the end of this process, when an active border vanishes, the trapezoid-shaped precipitate region is completed into a triangle-like one, with a small cusp on the top in some cases (fig. 3.4 (c.)). Due to the similarity of this cusp with some elements of sea shell patterns presented in [46], this formation will be referred to as the Meinhardt peak.

The angle of the passive borders is determined by two perpendicular velocities: the speed of the precipitation front (which is approximately equal to the speed of the diffusion front), and that of the precipitation front's regressing edges. The passive borders -except the region of the Meinhardt peaks and some transients at the split of precipitation fronts- are straight lines, especially in the "macroscopic" experiments, having a longer duration (in the order of 24 h). Thus, the ratio of the above mentioned speeds, except for some transients, must be constant during the experiments. At the present stage of research, the reason for this effect, as well as the factors which determine the speed of the regressing edges, are unknown.



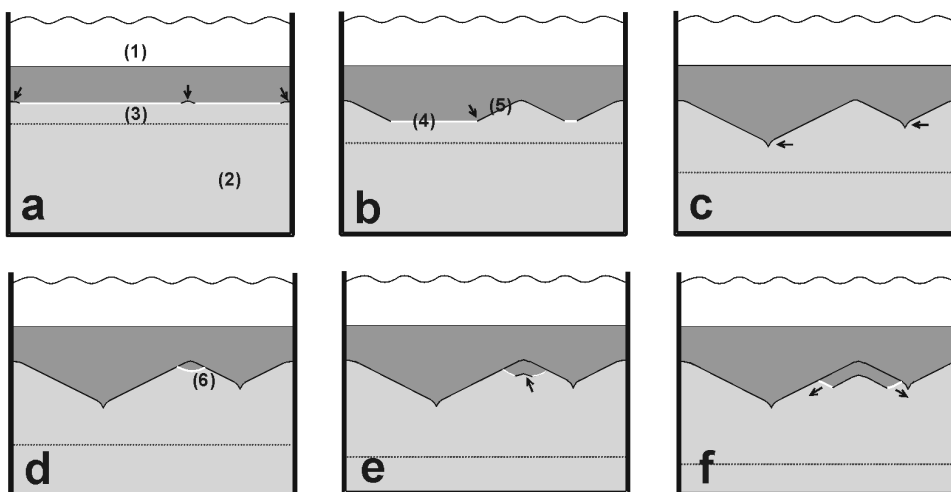


Figure 3.4: Schematic diagram of the sequence of pattern formation in gel sheets: (1) outer electrolyte having concentration  $a_0$ , (2) gel sheet containing the inner electrolyte with concentration  $b_0$ , (3) diffusion front of the outer electrolyte (dashed line), (4) shrinking precipitation fronts, (5) passive borders, (6) new precipitation front. The primary precipitate formed in the reaction is drawn in dark gray, while the precipitate-free gel with light gray. The passive borders are marked with black, while the active ones with white curves. Note, that in [157] the gray color represented the colloidal  $CuO$  precipitate, which is not marked here. (a.) Progressing of the precipitation front and that of the diffusion front. The formation of the precipitate is halted in three points, marked by arrows. (b.) Shrinking precipitation fronts leave behind trapezoid-shaped precipitate regions. A regressing edge is marked by an arrow. (c.) The precipitation fronts disappear, the triangle-like regions are completed. The Meinhardt peaks at the top of the triangle-like regions are marked by arrows. (d.) A new precipitation front emerges in the top of the wedge-like empty region. (e.) A precipitation front that emerges in the top of a wedge-like empty region, has just split. The point where the formation of the precipitate is halted, is marked by an arrow. (f.) Evolution of the new precipitation fronts formed by “pair-production”. Their direction of propagation is marked by arrows.

The velocity of the outer electrolyte’s diffusion front in agarose gel can be estimated by Fick’s law. However, in the case of PVA it is strongly influenced by the syneresis of the gel: about 2 mm behind the region where the precipitate has already formed, the gel starts to shrink and does not adhere any more to the glass [157]. Thus, the outer electrolyte is close to the active borders all the time, and is carried by diffusion only in the last few millimeters. However, the syneresis does not play an essential role in primary pattern formation. In agarose gel where no syneresis takes place, or in Petri dishes where the consequences of this effect can be neglected, the same types of patterns appear.

In case of the  $NaOH + CuCl_2$  system, the reactions do not stop at the stage when

the lower limit of the precipitate became a passive border. However, reactions such as  $NaOH + AgNO_3$  and  $CuCl_2 + K_3[Fe(CN)_6]$ , running in gel layers thicker than about 1 mm, stop after the development of the first complete layer of the passive border. As shown in fig. 3.4 (d.), new precipitation fronts in the  $NaOH + CuCl_2$  system can emerge somewhere along the passive borders (usually at the top of the wedge-like empty regions). Later, the new fronts may also be split. Thus, besides a new empty region, two precipitation fronts are also formed (figs. 3.4 (e.)-(f.) and 3.6 (a.)-(c.)). They produce precipitate bands below the already completed passive borders. The chemical constituent created by the new precipitation fronts is limited from above by the passive borders of the preceding precipitate, and from below by the passive borders formed in the wake of the new regressing edges. At a later stage, the new active borders are no longer parallel with the diffusion front (figs. 3.6 (b.)-(d.)). When two approaching active borders meet, they annihilate each other, and Meinhardt-peak forms at the annihilation point (fig. 3.6 (e.)).

The blue-green precipitate is not the final reaction product. About seven minutes after it has been formed, it starts to convert into a brown colloidal compound. Investigations with X-ray scattering [157] proved that this colloidal compound is  $CuO$  (fig. 3.5). Thermoanalytic measurements also support this result [13].

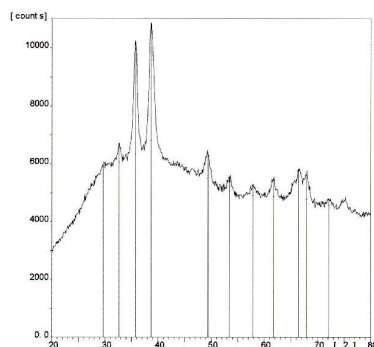


Figure 3.5: Powder spectrum of the brown precipitate.

The ripening process does not take place in a band of approximately  $100 \mu m$  thickness below the passive border of the preceding precipitate region. Thus, between the regions filled with  $CuO$ , a thin band remains free of this precipitate any time (3.6 f.). These *blind bands* are the black oblique lines that can be observed on the experiments. Note that the primary precipitate formed in the  $CuCl_2 + K_3[Fe(CN)_6]$  system seems to be stable, and does not convert into another compound.

Although the thermochemistry of the process is not known, it is assumed that thermal effects do not contribute significantly to the pattern formation. Precipitation after the first 30 min is very slow, and therefore local temperature changes in the precipitation front are probably insignificant. Note that the results are quite temperature-insensitive: the primary patterns observed in gel columns at room temperature also form between at  $10^\circ C$  and  $55^\circ C$ .

We finally mention an interesting effect that takes place when the outer electrolyte

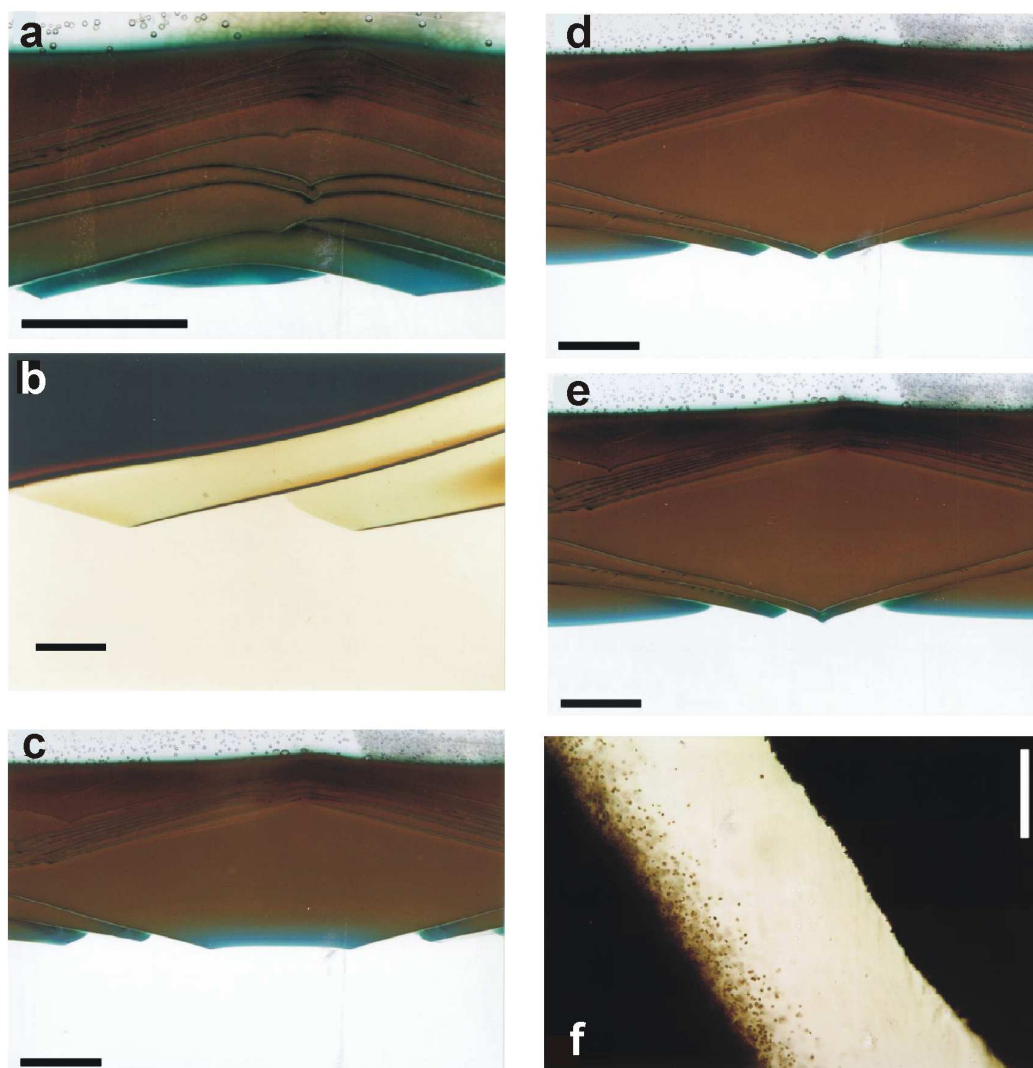


Figure 3.6: Patterns in gel sheets ( $a_0 = 8 M NaOH$ ,  $b_0 = 0.732 M CuCl_2$ ). Figures (a.), (c.), (d.) and (e.) represent experiments performed in gel sheets of  $1.6 mm$  thickness, located between two glass plates, and the pictures were taken using reflected light. Figure b. represents a pattern formed in a gel sheet located between a microscope slide and a cover glass, photographed in transmitted light. The sample shown in (f.) was prepared by sectioning a gel column after the reactions finished and the picture was taken in transmitted light. (a.) New front emerges at the top of an empty region (scale bar =  $2.5 mm$ ). (b.) Thin precipitate regions produced by traveling precipitation fronts. They are limited from above by the passive border of an elder precipitate and from below by the new passive border. (c.)-(e.) Three consecutive stages of the pattern development. Elapsed time from the beginning of the experiment was  $97 min$ ,  $131 min$  and  $137 min$ , respectively (scale bar =  $2.5 mm$ ). (c.) The precipitation front in the middle, limited by two regressing edges, shrinks. (d.) The regressing edges meet, and therefore this active border vanishes. Two small precipitation fronts can also be seen just before their annihilation. (e.) The pattern after the annihilation of the above small fronts. (f.) The blind band free of colloidal  $CuO$  precipitate, between an older (right) and a younger (left) precipitate.

diffuses into a gel where the concentration of the inner electrolyte is not homogeneous. If a gel located between two glass plates consists of two vertical domains having different inner electrolyte concentrations, the angle of the regressing edges changes as they pass through the border of the domains: they became more steep in the less concentrated gel region. This effect has not been studied in detail [13].

### 3.2.2 A Qualitative Explanation

First, a qualitative explanation of the pattern forming process is outlined. The experimental results that led to this picture, will be treated in detail later.

Let us assume first that we already have a progressing active border. Conditions of its appearance will be reexamined later. Several experiments suggest that the reactions first lead to the formation of a diffusive intermediary compound (DC), and a critical concentration of this compound is required in order for the precipitation to proceed [158, 161]. This concentration will be referred to as the *growth threshold*.

In a previous work, it was supposed that the reagents react and the DC forms only on the active border with catalytic properties [158]. In the present model, this supposition is not necessary. The experimental results showed that the passive border of a precipitate region is an ion-selective (semipermeable) surface, that restrains the passage of the reacting ions contained by the outer electrolyte [161]. DC forms in the whole region where the reagents meet, that is, due to the restraining properties of the passive borders, mainly the region ahead of the precipitation fronts.

Emergence of passive borders is explained as follows. If the growth threshold is not reached in a certain time  $\tau$  on a portion of the precipitation front, the front portion is assumed to lose its permeability, and becomes passivized. Since the speed of the precipitation front decreases in time, a constant value of  $\tau$  would entail its stoppage in a finite time. However, experimental results suggest that, having a constant outer electrolyte concentration, arbitrarily long front propagation can take place [157]. This can be reproduced by assuming that  $\tau$  is a function of the front speed  $v$ , and  $\tau = \tau(v)$  increases as  $v$  decreases.

The most important qualitative feature of the formation of primary patterns is the shrinking of active border segments that leave behind a trapezoid-shaped precipitate area, finally evolving to a triangle of precipitate [157, 158, 161]. In order to explain this feature, we have to assume that the concentration of the DC does not reach the growth threshold around the end point of the active border segment within time  $\tau(v)$ . Computer simulations showed, that this situation is typical. If the critical concentration of the DC is smaller than the value in the middle, but larger than the value near the end points of the active border, the next layer of precipitate (the new precipitation front) will be shorter than the actual front.

Initiation of traveling active borders is attributed to DC concentrations above the *nucleation threshold*, that is assumed to be higher than the growth threshold [162, 166]. In reactions like  $NaOH + AgNO_3$  and  $CuCl_2 + K_3[Fe(CN)_6]$  in gel columns or gel layers thicker than about 1 mm, new active borders appear almost exclusively at the beginning

of the experiment, when the outer electrolyte is layered on the gel. In the  $NaOH + CuCl_2$  system, front initiation can happen in the top of the wedge-like empty regions, some time after the passive border formed and reagent concentrations are recovered by diffusion. Since the reason of this latter effect is unknown, and simple assumptions did not lead to the expected simulation results, it is not included in the present model.

The development of a small cusp that may appear at the top of the triangle-like precipitate regions cannot be explained by qualitative arguments. This question will be reexamined when the computer simulation results are presented.

### 3.2.3 Experimental Results Supporting the Qualitative Explanation

The qualitative explanation presented above is supported by several experimental findings that were obtained in various setups. The most important observations are enumerated below:

(i) Active and passive borders have different shades of colors in the  $NaOH + CuCl_2$  system (fig. 3.7 (a.)). The passive border has an opalescent shade, unlike the growing, active one. This difference also suggests that active and passive borders have different structures.

(ii) An interesting phenomenon occurs when a precipitation front moving along a passive border reaches the top of a precipitate triangle. Figures 3.7 (b.) and (f.) represent the stage when one of the margins of the front moves along a precipitate area. The passive border of a previously formed precipitate is assumed to act as an obstacle into which the diffusive intermediary compound cannot penetrate. Therefore, the concentration of the DC is not diminished at this front margin. As the front approaches the top of the precipitate triangle, the DC around the end of the front starts to diffuse in a much larger area than previously. As a consequence, its concentration will diminish. If it drops below the critical concentration required for the progression of the active border for longer than  $\tau$ , the end point of the precipitation front may become ion-selective, and an *active-passive transition* may take place (figs. 3.7 (c.) and (g.)). Later, the portion of the border that is still active will shrink and evolve as described in the previous paragraphs. The same scenario can take place when a precipitation front passes through an obstacle with sharp edges.

(iii) When a segment of a precipitation front faces an obstacle such as an air bubble or a splint of glass of about  $0.1 - 1 \text{ mm}$ , the speed of that front portion increases before it touches the barrier (fig. 3.7 (h.)). The speed-up begins when the front is about  $60 \mu\text{m}$  from the obstacle. If the DC cannot pass through the barrier, its concentration may increase between the obstacle and the front. The higher concentration of the DC may be the most probable reason for the higher velocity of the precipitation front.

As mentioned previously, active-passive transition may take place if the precipitation front passes through an obstacle. As a result, the active border is splitting into two segments. Note that such breaks in the fronts have some common aspects with those reported in [167].

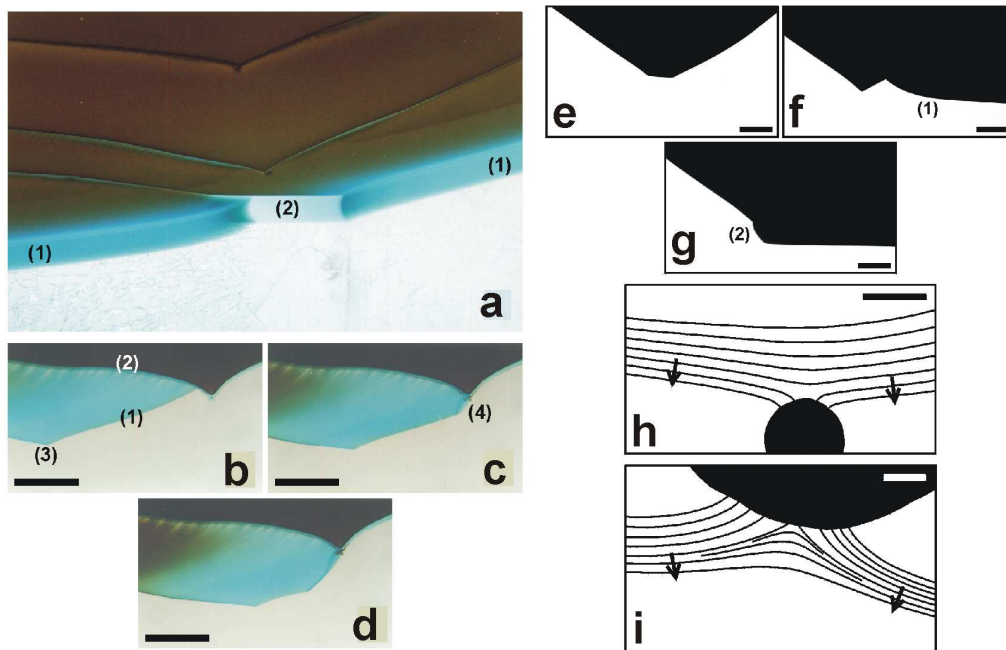


Figure 3.7: Experiments supporting the phenomenological model. (a.) Active (1) and passive (2) borders in the  $NaOH + CuCl_2$  system in PVA gel, from an oblique point of view. Note their difference with respect to the shade of the colors. The  $1.6\text{ mm}$  thick gel sheet is located between two glass plates.  $a_0 = 8\text{ M } NaOH$ ,  $b_0 = 0.732\text{ M } CuCl_2$ . (b.)-(d.) Active-passive transition in the  $NaOH + CuCl_2$  system. The reaction is taking place in an agarose gel sheet of  $1.6\text{ mm}$  thickness, located between two glass plates.  $a_0 = 4\text{ M } NaOH$ ,  $b_0 = 0.586\text{ M } CuCl_2$ , scale bar =  $2\text{ mm}$ . Panels (c.) and (d.) are taken  $871\text{ s}$  and  $1398\text{ s}$ , respectively, after panel (b.). The active border (1) is bounded on one side by the passive border of a previously formed precipitate (2), and on the other side by a regressing edge (3), which is the meeting point of the active and passive borders of the novel precipitate [panel (b.)]. When the active border reaches the top of the precipitate triangle, a new passive border will appear [panel (c.)]. The precipitation front becomes bordered by two regressing edges and will therefore shrink [panel (d.)], later disappearing. Note the decay of the blue-green precipitate in the brown precipitate. (e.)-(g.) Active-passive transition in the  $NaOH + AgNO_3$  system. The reaction takes place in PVA gel located between a microscope slide and a cover glass.  $a_0 = 8\text{ M } NaOH$ ,  $b_0 = 0.412\text{ M } AgNO_3$ , scale bar =  $0.5\text{ mm}$ . Panels (f.) and (g.) are taken  $552\text{ s}$  and  $672\text{ s}$ , respectively, after panel (e.). Panel (e.) shows a shrinking active border that leaves behind a trapezoid-shaped precipitate region. Panel (f.) displays an active border (1) that approaches the top of the precipitate triangle formed in the previous scenario. When it reaches the top, an active-passive transition takes place, and a new passive border (2) appears [panel (g.)]. (h.) Speed-up of a precipitation front segment facing an obstacle. The reaction takes place in PVA gel located between a microscope slide and a cover glass. The black lines represent the precipitation front every  $30\text{ s}$ , and the black region represents the obstacle itself. The arrows indicate the direction of the precipitation front.  $a_0 = 8\text{ M } NaOH$ ,  $b_0 = 0.732\text{ M } CuCl_2$ , and the scale bar =  $150\text{ }\mu\text{m}$ . (i) Fusing of precipitation fronts in the  $NaOH + CuCl_2$  chemical system. The reaction takes place in PVA gel located between a microscope slide and a cover glass. The black lines represent the precipitation front(s) every  $30\text{ s}$ , except for the two short curves in the middle. These short curves indicate the position of the fused front  $5$  and  $15\text{ s}$  after the last unconnected front segments were plotted.  $a_0 = 8\text{ M } NaOH$ ,  $b_0 = 0.732\text{ M } CuCl_2$ , and the scale bar =  $150\text{ }\mu\text{m}$ .

(iv) When two precipitation fronts meet and fuse together, the front speed is highly increased around the meeting point (fig. 3.7 (i.)). This speed-up is a result of both active borders having regions of DC ahead of them. In the immediate neighborhood of the meeting point these regions overlap, and thus the concentration of DC increases. Fronts are assumed to have greater velocity while sweeping through this area. Note that the concavity of the front causes an increase in velocity.

The survival of the short precipitation fronts traveling along a previously formed passive precipitate (figs. 3.6 (b.)-(d.)), as well as their annihilation (fig. 3.6 (e.)), can be explained by the above assumptions. Since the DC cannot penetrate into the already formed precipitate having an oblique passive border, its concentration is not diminished around the front margin that meets the passive precipitate. The other front margin is a regressing one, but the amount of regression is usually the same as the amount of front prolongation due to the obliqueness of the upper passive border. The quantitative study of this feature is under progress. Annihilation at the meeting point of two such traveling precipitation fronts takes place because a single active border forms after they fuse together. This active border will be limited by two regressing edges and shrink as described in section 2.2.2. However, in some exceptional cases the concentration of the diffusive intermediary compound at the meeting point can become so high that an “overflow” takes place leading to the rise of a growing, semicircular active border.

## Ion-selectivity of the Passive Borders

### A. Restraining properties

As mentioned previously, in the  $NaOH + AgNO_3$  reaction the precipitation does not restart ahead of the passive borders, while in the  $NaOH + CuCl_2$  system, the restarting of the precipitation is also delayed.

Because in the  $NaOH + AgNO_3$  and the  $NaOH + CuCl_2$  system the  $OH^-$  radical is the reacting ion of the outer electrolyte, it is plausible to assume that the precipitation ceases because the passive border restrains the passage of the  $OH^-$  ions. To confirm this hypothesis, simultaneous measurements of  $pH$  on both sides of the passive border were performed in the following experimental setup. The gel containing the inner electrolyte was located between two  $83 \times 102$  mm glass plates held 3 mm apart, the inner part of the first plate being covered by a polyethylene film. The outer electrolyte was layered on the gel (fig.3.8).

In a certain stage of the experiment, after removing the outer electrolyte, the first plate could easily be taken away. By gentle stripping the plastic foil, the surface of the gel could be revealed, and indicator paper was placed on the naked gel surface in such a manner that it touched both sides of the passive border. Drying of the gel is not significant in the time scale of the of the  $pH$  measurements (about 5 min).

In case of the  $NaOH + AgNO_3$  reaction precipitation ceases after the passive border covers the entire lower surface of the precipitate. The  $pH$  measurement was performed about 14 h after the reaction stopped (fig. 3.8 b). Since the  $pH$  did not equalize during this time, it is reasonable to assume that the passive border slows significantly the

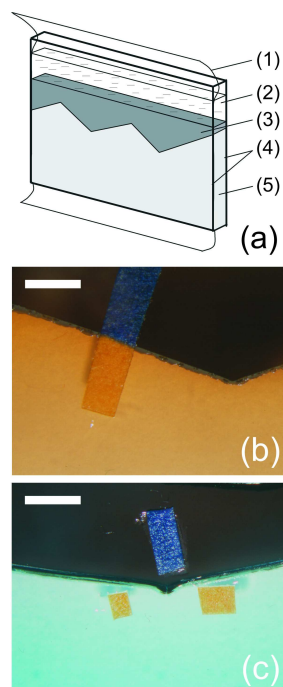


Figure 3.8: Measuring the  $pH$  difference between different sides of passive borders. The outer electrolyte is highly basic, while the inner electrolyte is slightly acidic. (a.) Experimental setup: (1) polyethylene film, (2) outer electrolyte, (3) precipitate, (4) glass plates, and (5) gel containing the inner electrolyte. The investigated reactions were  $8\text{ M NaOH} + 0.647\text{ M AgNO}_3$  in agarose gel (b.), as well as  $4\text{ M NaOH} + 0.586\text{ M CuCl}_2$  in agarose gel (c). The indicator paper has an orange color at slightly acidic, and a dark blue color at strongly basic  $pH$ . It is shown that the strongly basic  $\text{NaOH}$  solution impregnates the precipitate, but cannot pass the passive border that 'protects' the gel region containing the inner electrolyte. Scale bars =  $3\text{ mm}$ .

diffusion of the  $pH$ -determining ions. Note that in the course of revealing the passive border it may have been damaged and the precipitation process can restart along it, but this has a minor effect on the results of the, relatively quick,  $pH$  measurements.

The  $\text{NaOH} + \text{CuCl}_2$  reaction does not stop after the first complete layer of the passive border is formed. The reason why new precipitation fronts can arise below the passive borders is presently unknown, perhaps the passive borders are slightly leaky, or become damaged at some points. In the first hour of the reaction, precipitation restarts along the passive borders in ca.  $10\text{ mins}$ . Approximately three hours later long segments of passive borders were present in the gel, and these remain free of precipitate for several hours. The  $pH$  measurements performed on this system showed as well that a  $pH$  gradient between the two sides of the passive border lasted for at least 4 hours (fig. 3.8 c).

### B. Permeability of the Passive Borders

The above experiments indicated that the passive borders should restrain further passage of at least the  $pH$ -determining ions in the case of the  $\text{NaOH} + \text{AgNO}_3$  system. It is plausible to assume that, in the case of the  $\text{CuCl}_2 + \text{K}_3[\text{Fe}(\text{CN})_6]$  system, passage of copper ions is prohibited by the passive border (visual observations also support



this assumption). However, it is unclear at this point whether the passive borders are completely insulating membranes or restrain the diffusion of some kinds of ions only. Such questions can be answered by measuring the resistance (or conductance) of an appropriate gel segment with a passive border occupying the whole cross section of it: a high resistance indicates a completely insulating membrane; a low resistance indicates that some ions can cross the passive border. For the electrochemical experiments those chemical systems ( $NaOH + AgNO_3$  and  $CuCl_2 + K_3[Fe(CN)_6]$ ) were selected where the reactions stop as the passive border cover the entire bottom surface of the precipitate.

The experimental setup for the electrochemical measurements was built up as follows. The gel column, having a height of about 2 cm, was located in a Petri dish of 5 cm diameter, made of transparent plastic. Special care was taken in cleaning of the plastic Petri dish. The bottom of the dish contained a hole with a diameter of 3 cm. When the initial mixture was poured into the dish, the hole was closed with a polyethylene film. After the cross-linking took place, the film was removed, and the dish containing the gel was settled into a pot with larger diameter that contained an inner electrolyte solution with the same concentration as in the gel. In fig. 3.9 a, a typical experimental setup used for impedance measurements in the case of the  $CuCl_2 + K_3[Fe(CN)_6]$  system is shown. In most experiments an electrochemical cell consisting of a working electrode (W), a counter electrode (C), and a reference electrode (R) connected to an Autolab PGSTAT 20 electrochemical system (potentiostat + FRA module) was used. However, in some cases the reference electrode was directly connected to the counter electrode (in order to check the results also in the “2 electrodes” mode). In the 3 electrode arrangement a disk-shaped copper plate with a diameter of 3 cm was used for the working electrode, a platinum disk for the counter electrode, and a saturated calomel electrode (SCE) served as a reference.

It can be seen in fig. 3.9 a, that gel layers with and without the precipitate, the corresponding active and passive borders, and solution layers are located between the working electrode and the reference electrode. Using the above setup, the “total” impedance of the system (the impedance of the working electrode + the impedance of the different layers, borders and conducting phases between the working and the reference electrode) can be measured as a function of the frequency of a sinusoidal perturbing signal [170, 171].

The equivalent circuit representing the impedance of the above system is presented in fig. 3.9 b. According to this model a charging current and a current corresponding to the “faradaic” processes at the working electrode pass the metal/solution interface, while the total current is conducted by the electrolyte in the adjoining phases. The impedance elements corresponding to these processes are the double-layer capacitance ( $C_{dl}$ ), the charge transfer impedance ( $Z_c$ ), and the impedance of the conduction process ( $Z_s$ ). In most simple cases  $Z_s$  and  $Z_c$  are pure ohmic resistances ( $R_s$  is the “solution resistance” and  $R_c$  is the “charge transfer” or “polarisation” resistance). On the basis of the above consideration one can realize immediately that the resistance of the precipitate membranes are included in  $R_s$  in the equivalent circuit. In fig. 3.9 c, results of impedance measurements carried out at the equilibrium potential of the  $Cu$  working electrode are presented. By repeating the frequency scans continuously (and sufficiently fast), the

time evolution of the impedance after contacting the reacting solutions could also be followed. The frequency scans were started immediately after the outer electrolyte was layered on top of the gel, and finished when the passive border covered the entire lower surface of the precipitate. The impedance was measured during each scan at 6 discrete frequencies over a frequency range from  $f = 0.5 \text{ Hz}$  to  $f = 20 \text{ kHz}$ , applying a sinusoidal perturbing signal (amplitude:  $10 \text{ mV}$ ). It can be seen, that the  $Z'$  real parts of impedances are always relatively small ( $< 7 \Omega$ ), and the values measured at  $f = 10 \text{ kHz}$  and  $f = 788.5 \text{ Hz}$ , which can be identified unequivocally with the  $R_s$  resistance of the solution and precipitation/gel phases between the working and the reference electrode, are practically independent of time during the evolution of the precipitation patterns in the gel.

Similar results were also obtained for the  $\text{NaOH} + \text{AgNO}_3$  system. Thus, we can drive the conclusion that the passive borders are not completely insulating, but they bear ion-selective properties.

### Microspectrophotometric Measurements

In this section, results of microspectrophotometric measurements are presented demonstrating the existence of a chemical ahead of the active borders, that is supposed to be the diffusive intermediary compound. Spectral absorption measurements were made from small areas at small spatial intervals across the active border. The measurements were performed with the  $\text{NaOH} + \text{CuCl}_2$  reaction in PVA gel, since the hypothetical diffusive intermediary compound in this reaction was assumed to have an absorbance in the visible range [172].

First a gel layer of about  $0.2 \text{ mm}$  thickness was prepared between a microscope slide and a cover glass. This was achieved by putting some droplets of the gel mixture on the slide, covered by a cover glass and let to cross-link in this setup. In between the slide and the cover glass two splinters of a cover glass were placed as spacers. The reaction was started by putting some droplets of  $\text{NaOH}$  at the edge of the gel sheet. The droplet was covered by another cover glass to avoid its evaporation.

The measurement system consisted of an Olympus BHB compound microscope fitted with a camera port. The sample was mounted on the microscope stage and illuminated using standard bright field illumination. The sample was viewed with a  $10X$  NA 0.25 Olympus PL10 objective which enabled the advancing precipitation front to be imaged via  $10X$  eyepieces, one of which was fitted with a graticule. The ocular graticule allowed the user to determine the position on the preparation of the projected image of a  $500 \mu\text{m}$  diameter fibre optic which was mounted in the centre of the camera port. Light from a  $50 \mu\text{m}$  diameter area of the precipitation front was thus collected by the fibre optic which terminated in an Ocean Optics USB2000 miniature spectrometer. Spectral measurements were made in the range  $400 \text{ nm}$  to  $800 \text{ nm}$ , data being recorded with Ocean Optics' OOIBase32 software. Spectral measurements were made of the system dark current by occluding the fibre optic ('dark' measurements), a reagent-free area of the preparation (the 'baseline'), as well as the sample itself. Absorbance data were cal-

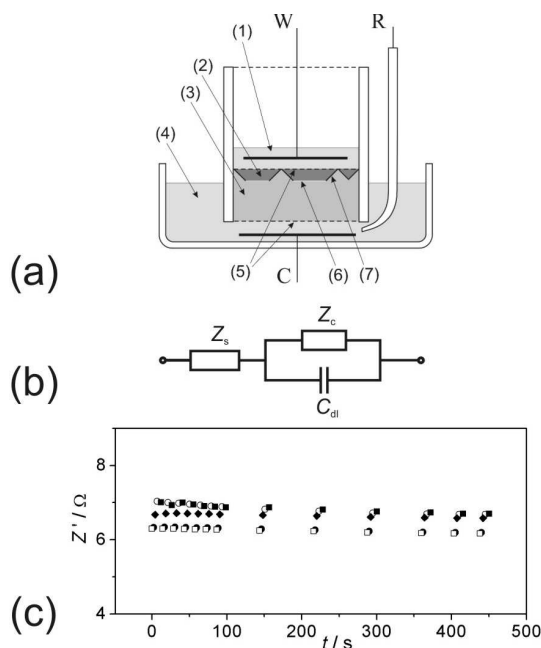


Figure 3.9: (a.) Schematic picture of the experimental setup used for impedance measurements. W: working electrode; R: reference electrode; C: counter electrode; (1) solution of the outer electrolyte, (2) precipitate, (3) gel containing the inner electrolyte, (4) solution of the inner electrolyte; (5) boundaries of the gel, (6) active border, (7) passive border. (b.) Equivalent circuit representing the impedance of the system.  $C_{dl}$ : double-layer capacitance;  $Z_c$ : charge transfer impedance;  $Z_s$ : the impedance corresponding to the conduction process. Results of impedance measurements carried out at the equilibrium potential of the Cu working electrode on  $2.93 M CuCl_2 + 0.12 M K_3[Fe(CN)_6]$  in agarose gel.  $Z'$ : real part of the complex impedance at different frequencies:  $\square$  : 10.09 kHz;  $\bullet$  : 788.5 Hz;  $\blacklozenge$  : 65.71 Hz;  $\circ$  : 5.97 Hz;  $\blacksquare$  : 0.5 Hz. The duration of a single frequency scan was 14.4 s, and each impedance value is assigned to the time of the completion of the measurement at the corresponding frequency.

culated as the negative decadic logarithm of the spectral transmission, the latter being calculated at each wavelength as (sample-dark)/(baseline-dark).

Spectral absorbance measurements were started when the precipitation front (the active border of the precipitate region) was at about  $200\mu m$  distance from the measuring light beam. At this point only the spectra of the  $CuCl_2$  could be observed (fig. 3.10). The front was approaching the measuring area at a speed of about  $0.7 \mu/s$  and thus, its distance from the beam decreased with time. The spectrum changed significantly when the distance decreased below about  $80\mu$ . Although the spectrum is too simple for determining the character of the underlying chemical compound, it clearly indicates the presence of a compound that is different from the reagents. Here we mention that no precipitation (formation of secondary patterns [160]) took place ahead of the active border.

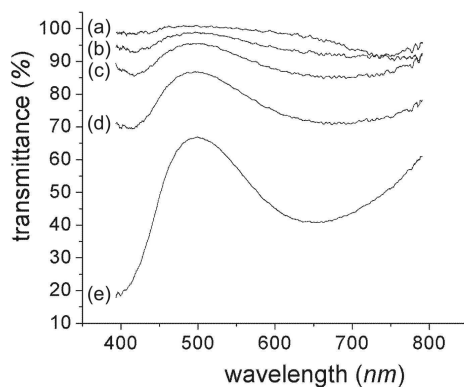


Figure 3.10: Microspectrophotometric measurements on  $8\text{ M NaOH} + 0.586\text{ M CuCl}_2$  in PVA gel. Curve (a) represents the spectrum of regions far from the precipitation front, where the limit of the measuring beam was at of  $180\ \mu$  from the front itself. Here only the inner electrolyte is present. Curves (b), (c) and (d) were measured closer of the precipitation front ( $75$ ,  $45$  and  $24\ \mu$  respectively), where traces of a new chemical compound can be observed. Curve (e) is the spectrum of the blue-green precipitate in the wake of the precipitation front.

As the front overtook the measuring light beam, the spectrum of the precipitate, having a blue-green color and assumed to be mainly  $\text{Cu}(\text{OH})_2$ , could be recorded. This spectrum shows similarity with that one measured ahead of the front. Note that  $7-8\ \text{min}$  after it has been formed, the blue-green precipitate decays to brown  $\text{CuO}$ , but this last step has no influence on the process of pattern formation [157]. This experiment also confirmed the hypothesis that the bulk precipitate does not halt the diffusion of the outer electrolyte's reacting ion, and neither does the active border.

### Other Experimental Findings

Two further experimental findings also support the tightly closed structure of the passive borders. Dissolving by EDTA (ethylene-diamine-tetraacetate) the final  $\text{CuO}$  precipitate formed in the  $\text{NaOH} + \text{CuCl}_2$  reaction in PVA gel, the trace of the passive borders can be observed even by naked eye as opalescent surfaces. This indicates that the gel structure is getting damaged when the passive borders build up. In addition, when the reactions are over, the gel breaks more easily along the trace of the passive borders. Consequences of damaging the passive edge while the reaction is running were also examined. When the passive edge was mechanically cut, or destroyed by a strong laser beam, new precipitation fronts started but were quickly passivized, probably because the inhomogeneities generated during the damaging act as centers where new passive borders can start. When a small gel segment, crossed by a passive border, was replaced by a piece of gel containing only the inner electrolyte, a new precipitation front started at that region.

It should to be mentioned that our findings are supported by some classical results of colloid science. It is well known that copper-ferrocyanide precipitate was used in osmotic studies in the 19<sup>th</sup> century. According to the experiments of Traube [173], when a drop of copper sulfate solution is brought into contact with a drop of potassium ferrocyanide solution, a thin layer of reddish-brown copper-ferrocyanide precipitate forms at, and blankets, the entire boundary. After that, no further formation of precipitate occurs. Thus the thin layer of precipitated material formed between the two drops of solutions has halted further passage to the other side of the copper ion as well as the ferrocyanide ion. By allowing the copper ferrocyanide precipitate to form within the wall of an unglazed porcelain cylinder, Pfeffer transformed Traube's fragile layer of copper-ferrocyanide precipitate into a membrane strong enough to withstand not only routine handling but even unilateral application of mechanical pressure [174]. This membrane was permeable to water, but not to sugar, therefore it was named a semipermeable membrane. However, as it was already emphasized by Nernst, copper ferrocyanide membranes are permeable for several chemical substances, *e.g.* nitrates, hydrochloric acid, and many pigments [175]. Up to this time, only the semipermeable character of the copper-ferrocyanide precipitate has been shown. Our experimental results suggest that the bulk of a class of precipitates, among others the copper-ferricyanide, can have two kinds of borders, one of them selectively halting the passage of some ions, while the other border, as well as the bulk precipitate, does not prohibit diffusion. The microscopic structure of these borders, as well as that of the bulk precipitate, is the subject of intensive research.

### 3.3 Formation of Primary Patterns in Gel Columns

When the outer electrolyte is poured onto the top of a gel column, the diffusion front is expected to have the form of a disk, in contrast with previous cases, when it had a shape of a thin band. In this instance, the precipitation fronts involved in pattern formation can perform more complicated motion, leading to more complex patterns than in the previous case. A series of patterns were observed that depend on the outer and inner electrolyte concentrations (fig. 3.11). The experiments were carried out in glass test tubes of 14.2 *mm* inner diameter, and in plastic Petri dishes of 13 *mm* height and 87 *mm* inner diameter.

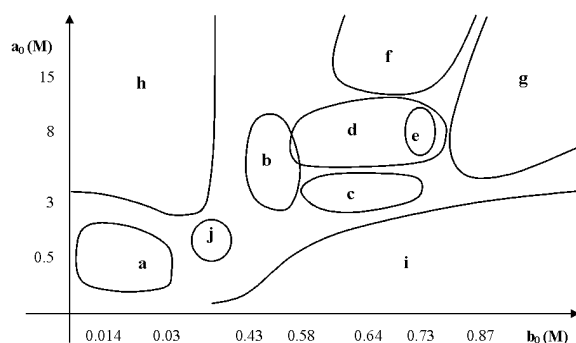


Figure 3.11: Concentration “phase”-space of the reagents for the patterns formed in test tubes. (a.) irregular Liesegang banding; (b.) homogeneous brown precipitate; (c.) helicoidal patterns having a decreasing pitch; (d.) helicoidal patterns; (e.) region where cardioid patterns may appear; (f.) randomized helicoidal patterns; (g.) cabbage-like patterns; (h.) homogeneous green or purple precipitate; (i.) the precipitation stops close to the top of the gel column because of the depletion of the outer electrolyte; (j.) crescent-like rhythmic patterns.

### 3.3.1 Rhythmic Banding

When the outer and inner electrolyte concentrations are in region “a” in fig. 3.11, a green-colored substance is formed behind the diffusion front that was found to be optically more dense in separate, but randomly spaced regions along the gel column (fig. 3.12 (a.)). This can be considered as an example of the irregular Liesegang banding. In this case, syneresis of the gel has not been observed, and the ripening process leading to the colloidal brown precipitate did not take place at all.

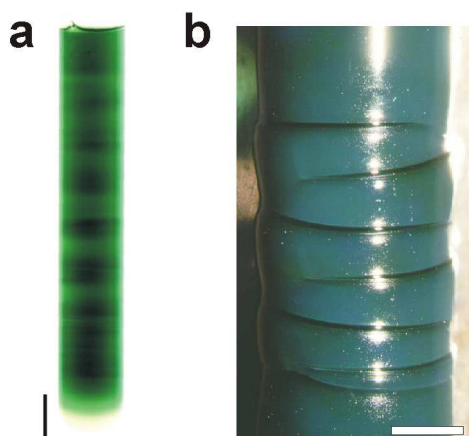


Figure 3.12: (a.) Irregular Liesegang banding in a test tube.  $a_0 = 0.5 M$ ,  $b_0 = 0.0293 M$ , scale bar = 1 cm. (b.) Crescent-like rhythmic pattern in a test tube.  $a_0 = 1 M$ ,  $b_0 = 0.146 M$ , scale bar = 0.5 cm.

With electrolyte concentrations as in region “j” in fig. 3.11, an opaque green precipitate is formed that is periodically jagged by crescent-like dark regions, that might be a variant of the ‘blind bands’ (fig. 3.12 (b.)). These patterns have not been studied in detail [13].

### 3.3.2 Homogeneous Precipitation

At higher outer and inner electrolyte concentrations (regions “b”-“f” in fig. 3.11) the blue-green precipitate (that later decays into the brown, colloidal  $CuO$ ) will appear in the wake of the precipitation fronts. At the concentration values of region “b”, regressing edges cannot survive, even with special initial conditions that will be discussed below. A system lacking the possibility of forming regressing edges will be referred to as *not stimuable*. Note that this concept is different from “excitability”, where the medium is able to regenerate.

In order to establish the inner electrolyte value for which the system is no longer stimuable, special initial conditions have been created. The stimuability of a narrow top region of the gel column was raised by increasing the inner electrolyte concentration of that region. This was achieved by pouring 2.96 M  $CuCl_2$  solution on the gel for 10 min. Having removed the  $CuCl_2$  solution, the 8 M  $NaOH$  outer electrolyte was poured on the top. The precipitation front split while passing through the gel region with increased stimuability, and the resulting passive borders either survived or died out (*i.e.* the uncut front was reestablished) as the front left the top of the gel column. The lowest inner electrolyte values for which the passive borders survived, were about 0.58 M  $CuCl_2$ . Below this concentration, regressing edges ceased to exist in the system. Note that the spontaneous splitting of precipitation fronts requires a higher concentration of inner electrolyte than that for maintaining the already formed passive borders. Depending on the smoothness of the gel surface, for an outer electrolyte of 8 M  $NaOH$ , this concentration varies between 0.62 – 0.72 M  $CuCl_2$ .

### 3.3.3 Helicoids, Spirals

Rotating spiral-shaped precipitation fronts can form in the region “d” on the phase-space figure 3.11. At the higher inner electrolyte concentration limit of this region cardioid patterns may also form. At the lower limit the splitting of the precipitation front occurs only when the stimuability of the top of the gel column is enhanced, as described above. As the front leaves the top region, and enters a region where the concentration of the inner electrolyte is homogeneous, the passive borders survive.

After a short transient, the active borders took the form of spiral arms. As the diffusion front advanced, they swept through the gel while rotating around the axis of the gel column (figs. 3.13 (b.), (e.) and (f.)). Note that at first, the blue-green precipitate forms in the wake of the active borders, and this precipitate decays in about 7 – 8 min to the colloidal brown  $CuO$ . However, the  $CuO$  did not form in thin, blind regions below the passive borders of domains already filled with precipitate. These blind

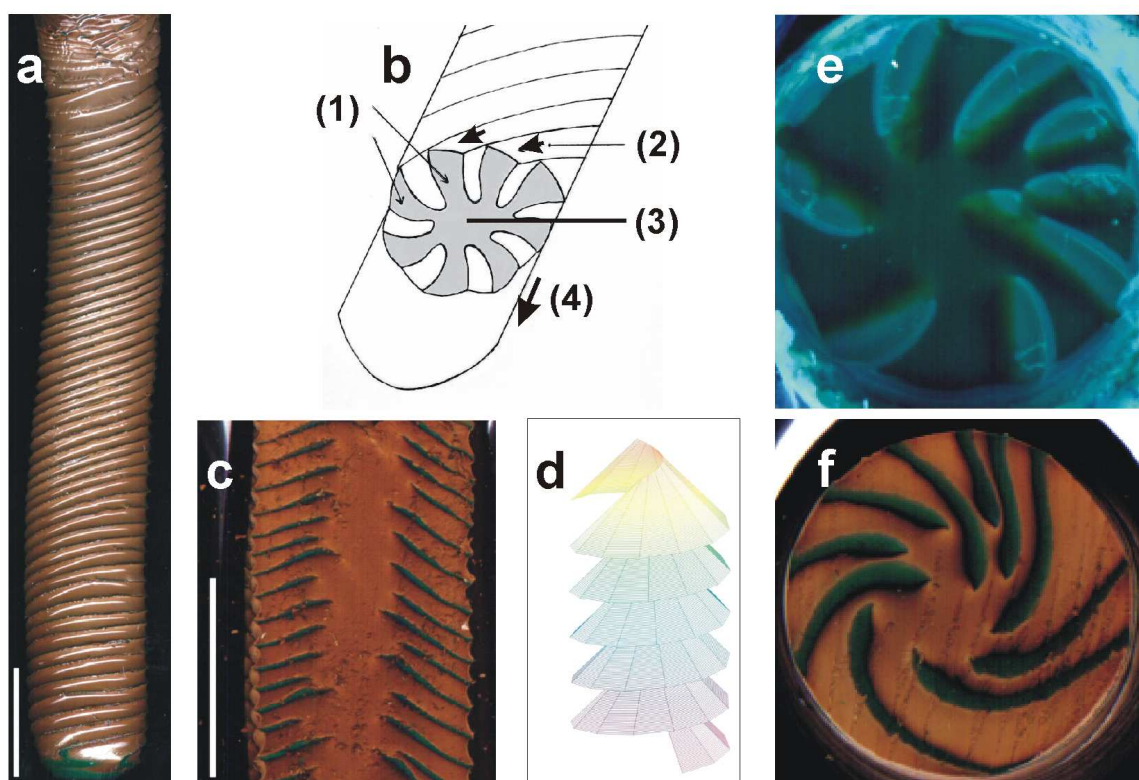


Figure 3.13: Patterns formed in a test tube by precipitation fronts shaped like spiral arms.  $a_0 = 7.5 M$ ,  $b_0 = 0.644 M$ . (a.), (c.) The gel column and its longitudinal section after the reactions finished. The “plastic” form is caused by the syneresis of the gel. Scale bar = 10 mm. (b.) The structure of the precipitation fronts: (1) the active border (the precipitation front), (2) arrows that mark the growing direction of the precipitation fronts, (3) core, (4) arrow that marks the advancing direction of the diffusion front. (d.) computer graphics of helicoids similar to the blind regions. (e.) “In vivo” figure of the front structure. The active borders have a dark shade, while the passive borders have an open shade. The diameter of the pattern is 14 mm. (f.) Cross-section of the gel column after the termination of the reactions. The black curves are the traces of the blind areas free of  $CuO$ . In the central region (core) no front splitting took place. Scale bar = 2.5 mm.

bands are the dark curves on figs. 3.13 (c.) and (f.).

In a central region called the *core*, the precipitation front did not split. The diameter of the core was approximately 4 mm, this value being larger for the experiments in which the inner electrolyte concentration was lower. Note that the spiral-shaped trigger waves in the Belousov-Zhabotinsky reaction also have a well-defined core [168, 169].

The oblique motion of the spiral-arm-shaped precipitation fronts leads to telescoped helicoid-like regions filled with colloidal  $CuO$ , separated by the thin, dark blind areas (fig. 3.13 (d.)). The handedness of the helicoids was determined by random splitting and



annihilation of the precipitation fronts at the upper end of the gel column. The pitch of the helicoids was constant during the experiments when 6 mL of 8 M NaOH was layered on the gel column having an initial volume of about 18 – 20 mL and a diameter of 14,7 mm. Observing that the angle of the passive borders and thus the pitch is determined by the ratio of the precipitation front's vertical and the regressing edge's horizontal velocities, this ratio had to be unchanged during the experiment. The reason why the velocity of the regressing edges is correlated with that of the precipitation fronts, is presently unknown. Note that the vertical speed of the active borders is determined by the diffusion front, and decreases with time.

However, when the concentration of the outer electrolyte having a volume of 6 mL was only of 3 M, the pitch of the helicoids was not constant any more. As the reaction proceeded, the outer electrolyte depleted, and the speed of the diffusion front decreased markedly before the front finally came to a halt. The speed of the regressing edges did not decrease in the same manner, and this led to the gradual decrease of the pitch (fig. 3.14). At the present stage of research the reason for this effect is unknown [13].



Figure 3.14: Spiral with decreasing pitch.  $a_0 = 3 M$ ,  $b_0 = 0.586 M$ . Scale bar = 5 mm.

### 3.3.4 Cardioid-like Patterns

In region “e” of fig. 3.11 the types of patterns that formed were unpredictable: in 70 % of the experiments rotating spiral-like precipitation fronts were formed similar to those presented above, and in 30 % of the cases, cardioid-shaped patterns emerged. The development of the latter passed through various stages as the diffusion front swept through the gel column (fig. 3.15). At a certain point in the central part of the precipitation front, a small, arch-shaped split occurred, in which precipitation did not take place (fig. 3.15 (b.)). The external border of the arch was a regressing edge, leaving behind an

empty area subsequently filled with precipitate. In the next stage the arch grew, and its ends turned against each other. When they met, the pattern took the form of a closed cardioid (fig. 3.15 (c.)). At that moment, the precipitation front (formerly a connected region) was split into two parts. In between, an empty, “blind” region is present, having cardioid cross-section. As the diffusion front advanced, the outer precipitation front, which had a cardioid-shaped regressing edge, became smaller, while the inner front was getting larger. When the diameter of the inner front reached about  $6\text{ mm}$ , a new split occurred (fig. 3.15 (d.)).

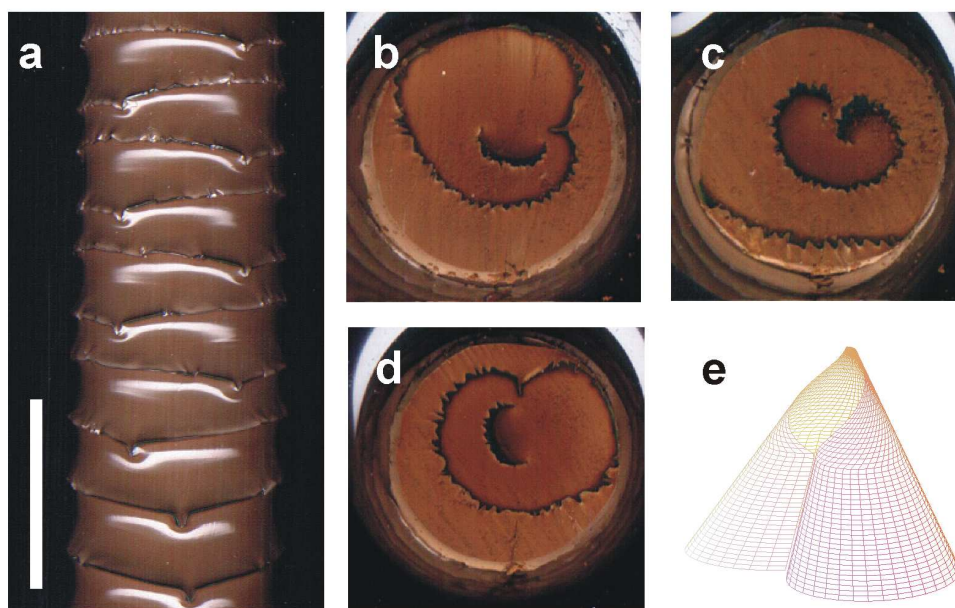


Figure 3.15: Cardioid-like patterns in test tubes.  $a_0 = 8\text{ M}$ ,  $b_0 = 0.732\text{ M}$ . (a.) Close-up of the gel column, scale bar =  $10\text{ mm}$ . (b.)-(d.) Cross sections of the gel column after the reaction took place, located one below the other, representing consecutive stages of the pattern development. (b.) A new split emerges while an old, cardioid-shaped regressing edge reaches the border of the gel. (c.) A closed cardioid forms (d.) The cardioid is getting larger, and another split emerges (e.) Computer graphics of a cardioid-based cone resembling the structure of the black blind regions.

A few minutes after the active borders produced the blue-green precipitate, the ripening process began to generate the colloidal brown precipitate. Only the thin, blind bands below the passive borders of the regions precipitated by different fronts remained empty of the brown precipitate.

### 3.3.5 Target-like Patterns

In order to test whether the formation of spiral and cardioid-shaped fronts is an inherent property of the chemical system, or is due to the geometry of the test tubes or the

syneresis of the gel, experiments have been performed in Petri dishes also. The inner diameter of the Petri dish (87 mm) is much larger than the characteristic size of the patterns, and thus, they cannot “feel” the border of the dish. The effects of the syneresis are negligible except at the margins of the gel. Observing that spirals and cardioids appeared in these experiments also, they could not be generated by border effects (fig. 3.16 (a.)).

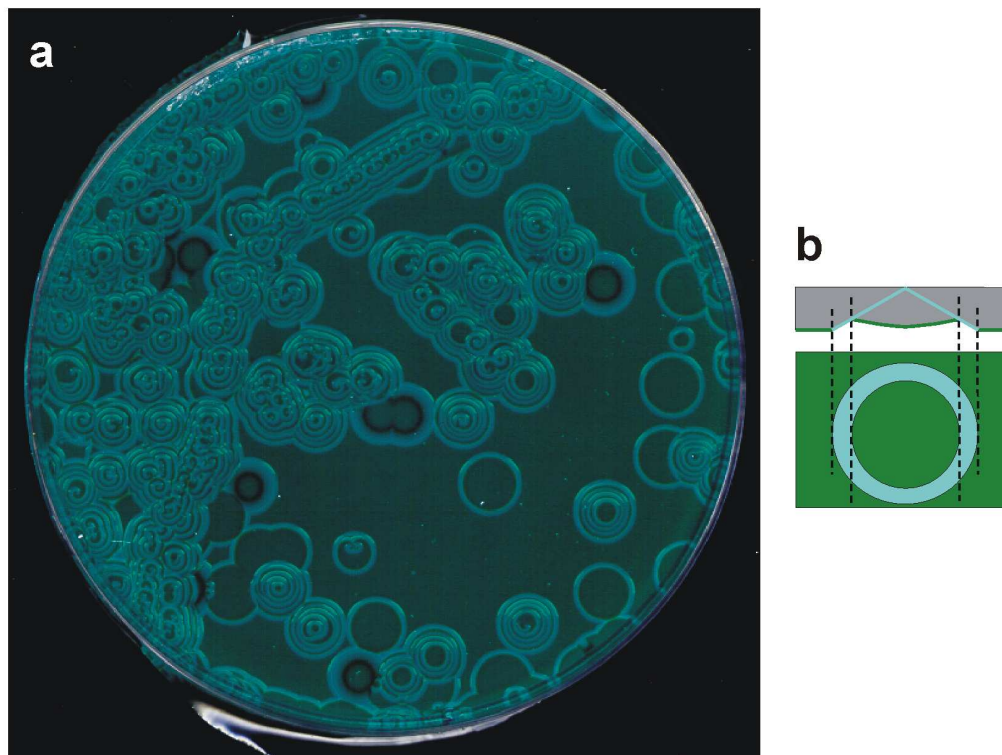


Figure 3.16: (a.) Target patterns, spirals and cardioids in a Petri dish of 87 mm inner diameter.  $a_0 = 8 M$ ,  $b_0 = 0.732 M$ . The dish was put on a scanner while the reactions take place, and the picture was taken from below. The light curves are the passive borders of the precipitate, while dark surfaces are the active borders. (b.) Sketch on the formation of the target patterns.

Beside the above mentioned formations, *target-like patterns* often emerged in Petri dishes. These patterns have almost never been observed in test tubes. The development of a target-like pattern proceeds as follows.

At a certain point of the active border the formation of the precipitate stops. As the active border progresses, these points expand into a cone-like region free of precipitate, while the front, having a circle-shaped regressing edge, decreases in surface. The wall of the cone is a passive border. Because the passive borders are more pale than the active ones, a disk-shaped light spot (the projection of the cone) in a dark background (the precipitation front, *i.e.* the border that is still active) will be observed if the Petri dish is looked at from below.

However, the precipitation in the empty region restarts very soon, usually in the top of the empty cone. Since the new active border has the same dark shade as the older active borders, and the new precipitate covers the central region of the cone, a light ring (the uncovered part of the passive border) in a dark background (the inner new, and outer old active borders), as sketched in fig. 3.16 (b.), will be observed if the Petri dish is looked at from below. Some time later another passive cone arises in the newly formed precipitate, and the process repeats itself. Target patterns having 6 – 8 “rings” have also been observed (fig. 3.16 (a.)).

### 3.3.6 Cabbage-like Patterns

At very high outer and inner concentration values, regular, ordered patterns no longer form. The traveling precipitation fronts frequently emerge and annihilate. The precipitation fronts frequently split at the same time. All of these phenomena resulted in the “cabbage-like” pattern shown in fig. 2.15.

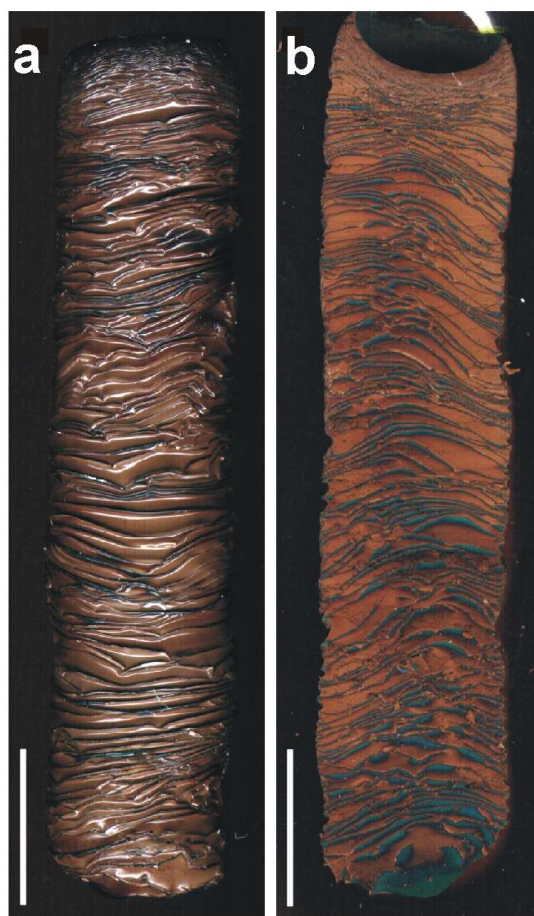


Figure 3.17: Cabbage-like disordered patterns formed in gel columns. The electrolyte concentrations were very high ( $a_0 = 15 M$ ,  $b_0 = 0.879 M$ .) Scale bar = 1 cm. (a.) The gel column after the reaction takes place. (b.) Longitudinal section of the gel column. Frequent birth and annihilation of precipitation fronts can be observed.

## 3.4 Voronoi Diagrams

Patterns in  $NaOH + AgNO_3$  and  $CuCl_2 + K_3[Fe(CN)_6]$  -like chemical systems are not so various: the reactions stop after the formation of a complete layer of passive border [159]<sup>1</sup>. However, when the reactions are running in Petri dishes, the dynamics of regressing edges can lead to the formation of an interesting type of patterns, resembling *Voronoi diagrams*.

### 3.4.1 Concept and Generation of Voronoi Diagrams

Problems related to spatial tessellations arise in almost all fields of science, where a space should be partitioned into "spheres of influence". Finding the best facility location [176, 178, 179], description of aggregation territories of slime mold cultures [180], investigating the geometry and growth of cells [181] and modeling some animal coat patterns [182, 183] requires tasks of tessellations to be solved. These can usually be achieved by constructing the *Voronoi diagram* of the problem [176, 178]. The Voronoi diagram (in plane) is the nearest-neighbor map for a set of initially given points. Each region contains those points that are nearer to one input point than any other input point, while edges of regions are equidistant to them. A Voronoi diagram is sometimes also known as a Dirichlet tessellation. The cells are called Dirichlet regions, Thiessen polytopes, or Voronoi cells and the boundaries of the cells are termed the medial axes.

Several kinds of simple reaction-diffusion systems in gels are found to be able to generate Voronoi diagrams [159, 177, 184]. In the reaction-diffusion system presented in [159] some droplets of an appropriate outer electrolyte ( e.g. ferric (III) chloride and potassium iodide) were put at distinct points on the surface of a thin gel sheet containing the inner electrolyte (e.g. potassium ferrocyanide or palladium chloride). Thus a precipitation reaction is initiated around the droplets. Because the process is diffusion limited, ahead of the reaction fronts there is a thin region, where the inner electrolyte is depleted. Just before the reaction fronts started from different droplets meet, the depleted regions overlap, and the precipitation ceases or is significantly reduced. Since the speed of the fronts started from different points varies (decreases) with time in an identical manner, then the resulting pattern, consisting of precipitate regions and empty bands, represents the Voronoi diagram of the droplets. Chemical reactions of this type have been used as experimental chemical processors for solving shortest path problems [185], and in the construction of experimental XOR logic gates [186].

---

<sup>1</sup>Note that the  $NaOH + AgNO_3$  reaction, running in a thin gel sheet located between a microscope slide and a cover glass, does not cease after the formation of the first layer of passive border, and thus it can yield a great variety of patterns [158].



### 3.4.2 Voronoi Diagrams Generated by Regressing Edges of Precipitation Fronts

Ability of building Voronoi diagrams of the  $NaOH + AgNO_3$  or  $CuCl_2 + K_3[Fe(CN)_6]$  processes in a "Liesegang setup" has been investigated. The inner electrolyte was homogenized in agarose gel. The gel layer, having a height of about 6 mm, was located into Petri dishes of 87 mm internal diameter and 13 mm height.

The reactions were started by pouring a layer of about 5 mm of outer electrolyte onto the gel. Having a concentrated outer electrolyte (8 M  $NaOH$  or 2.93 M  $CuCl_2$ , respectively), three types of behavior have been observed as the inner electrolyte concentration was varied.

At low inner electrolyte concentrations (below 0.3 M  $AgNO_3$  or 0.03 M  $K_3[Fe(CN)_6]$ ) a homogeneous precipitate forms in the regions reached by the outer electrolyte, irrespectively of the condition of the gel surface.

When the concentrations were approximately 0.64 M  $AgNO_3$  or 0.09 M  $K_3[Fe(CN)_6]$ , Voronoi diagrams could be formed in a controlled way: in this case the centers of the induced Voronoi cells were the points at which the gel surface had been deliberately marked *e.g.* by gently touching the gel surface with a pipette tip or thin glass stick. At these concentrations no natural Voronoi cells would be formed, and if the gel had not been marked, then a homogeneous precipitate would have resulted from the addition of the outer electrolyte.

At even higher inner electrolyte concentrations, (*e.g.* 0.88 M  $AgNO_3$  or 0.15 M  $K_3[Fe(CN)_6]$ ) minor defects of the gel surface become the natural centers of the Voronoi cells. Thus, the pattern becomes uncontrollable.

The precipitate patterns resembling Voronoi diagrams are built up via the following sequence of events. The precipitation does not begin on the whole surface of the gel: in some points, where the surface is damaged, the reaction does not start at all (fig. 3.18 a). As time evolves, and the diffusion front followed by the precipitation front sweeps through the gel, these points expand into empty cones, free of precipitate (fig. 3.18 b). The precipitation continues only on the leaky-disk-like active border. Since the base of the empty cones grows as the front progresses, the disk-shaped holes in the front will also grow in size. The circular margins of the holes are the regressing edges of the active border. The reaction does not proceed on the mantle of the cones that separate the already formed precipitate from the empty regions, being the passive borders of the precipitate region.

At the points where the regressing edges of the fronts meet, the precipitation stops (fig. 3.18 c). Seeing that the horizontal speed of the regressing edges changes in time in the same way, the locus of their meeting will draw the Voronoi diagram of the points where the precipitation did not start. The Voronoi polygon appears as a local minimum of the precipitate region's lower surface (the passive border). All of these stages can be observed on the figures 3.19 and 3.20 representing the formation of controlled and spontaneous patterns in the  $CuCl_2 + K_3[Fe(CN)_6]$  and  $NaOH + AgNO_3$  experimental systems, respectively. Note that in rare cases the precipitation may restart and a small

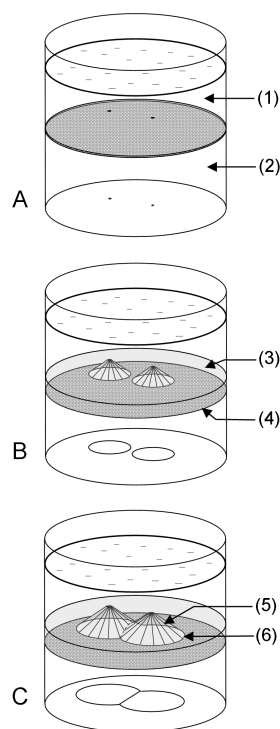


Figure 3.18: Schematic representation of Voronoi diagram formation through “regressing edge mechanism”. (1) outer electrolyte, (2) agarose gel containing the inner electrolyte, (3) precipitate, (4) precipitation front (active border, represented by a dotted surface), (5) passive border, (6) regressing edge. The contours of the patterns are drawn on the bottom of the vessel. (a.) The precipitation does not start at some points of the gel surface. (b.) These points expand into precipitate-free cones as the front progresses. (c.) The regressing edges meet on the line that is an equal distance from the tip of the empty cones.

amount of precipitate can form even after a connected layer of passive border is formed.

It should be noted that the precipitation may stop not only at the gel surface just after the reactions have been started, but at a later stage of the progression of the leaky-disk-like precipitation front. If some of the cones start to develop at this later stage, the resulting polygon will not be a Voronoi-like one, since the “belated” cones will be able to expand only in a smaller area. The tessellation generated in this way can be regarded as a generalization of a Voronoi diagram, and it may also be related to some practical problems.

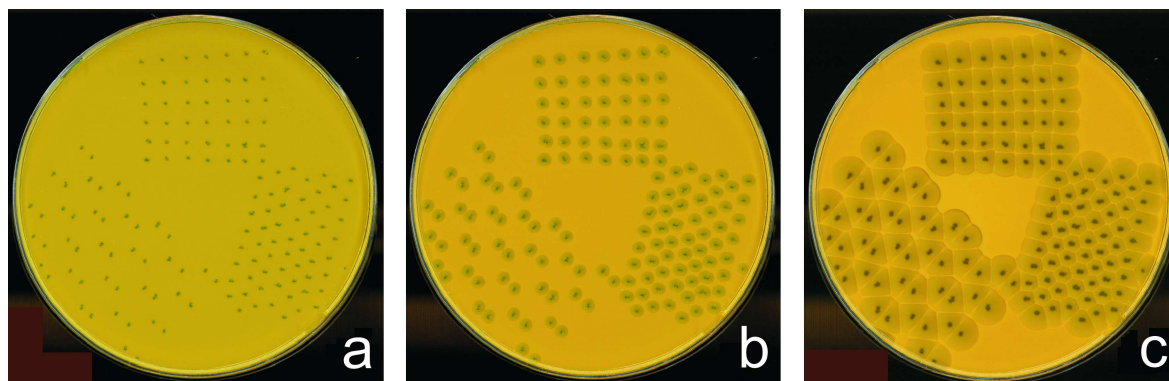


Figure 3.19: Consecutive stages of development of a controlled Voronoi diagram, representing triangular, rectangular and hexagonal arrangements. The centers of the cells were put by hand, therefore the pattern is not “true to type”. The outer electrolyte was of  $2.93\text{ M CuCl}_2$ , while the inner electrolyte of  $0.09\text{ M K}_3[\text{Fe}(\text{CN})_6]$ . Time elapsed from the start of the experiment was  $43\text{ s}$ ,  $198\text{ s}$  and  $878\text{ s}$  at panels (a.), (b.) and (c.), respectively. The diameter of the Petri dishes is  $87\text{ mm}$ .

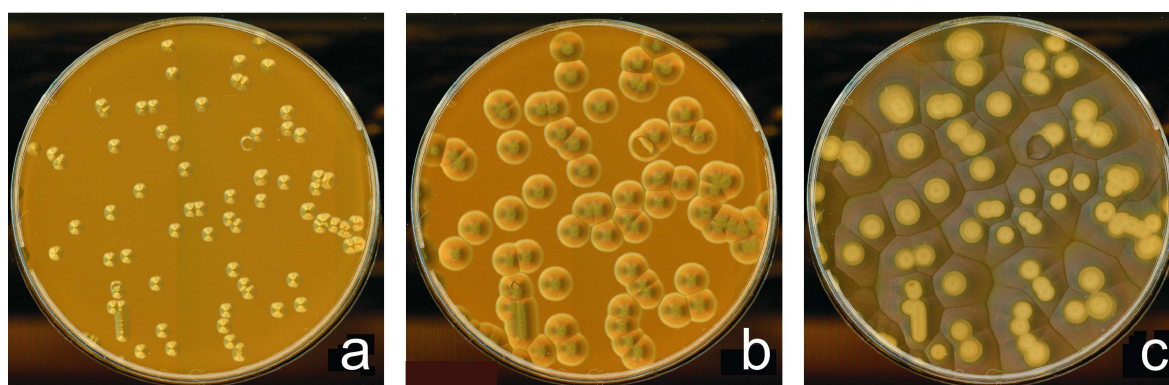


Figure 3.20: Consecutive stages of development of a spontaneous Voronoi diagram. The outer electrolyte was of  $8\text{ M NaOH}$ , while the inner electrolyte  $0.882\text{ M AgNO}_3$ . Time elapsed from the start of the experiment was  $35\text{ s}$  and  $138\text{ s}$  at panels (a.) and (b.). The figure represented at panel (c.) was taken after the termination of the reactions. The diameter of the Petri dishes is  $87\text{ mm}$ .



# Chapter 4

## Primary Patterns: Theory and Computer Simulations

### 4.1 The Mathematical Model

The mathematical model is based on the most relevant experimental results presented in [157, 158, 161]. It consists of coupled reaction-diffusion equations and a cellular automata [187, 188, 190]. The latter were included in the model in order to handle the precipitate regions, which have sharp bordering surfaces.

First version of the model has been published in [158]. Similar cellular automata–reaction-diffusion approach has recently been used to model chemical systems involving a long (macroscopic) and a short (atomic) length scale [189].

Most elements of the model are straightforwardly derived from the experiments (existence of the DC, as well as that of active(permeable) and passive (restraining) stages of the precipitate), some others represent classical results of colloid science (nucleation and growth thresholds). The assumed mechanisms of passivization are deduced from indirect observations. However, they represent the simplest assumptions that led to the patterns observed in the experiments.

Equations and cellular automata rules of the dimensionless model are the following:

$$\frac{\partial a(x, y, t)}{\partial t} = D_a(x, y) \cdot \Delta a(x, y, t) - r \cdot a(x, y, t) \cdot b(x, y, t) \quad (4.1)$$

$$\frac{\partial b(x, y, t)}{\partial t} = D_b(x, y) \cdot \Delta b(x, y, t) - r \cdot a(x, y, t) \cdot b(x, y, t) \quad (4.2)$$

$$\frac{\partial c(x, y, t)}{\partial t} = D_c(x, y) \cdot \Delta c(x, y, t) + r \cdot a(x, y, t) \cdot b(x, y, t) - [R] \quad (4.3)$$

- R0:  $[c(x, y, t) > c^{**}] \wedge [d(x, y, t) = \text{empty}] \rightarrow d(x, y, t + \Delta t) = \text{active border}$
- R1:  $[c(x, y, t) > c^*] \wedge [d(x, y, t) = \text{active border}] \wedge [d(x_{nn}, y_{nn}, t) = \text{empty}] \rightarrow$   
 $\rightarrow [d(x_{nn}, y_{nn}, t + \Delta t) = \text{active border}] \wedge [d(x, y, t + \Delta t) = \text{bulk precipitate}] \wedge$   
 $[c(x, y, t + \Delta t) = 0]$
- R2:  $[c(x, y, t) < c^*] \wedge [d(x, y, t) = \text{active border}] \wedge [T(x, y, t) \leq \tau(v)] \rightarrow$   
 $\rightarrow T(x, y, t + \Delta t) = T(x, y, t) + \Delta t$
- R3:  $[c(x, y, t) < c^*] \wedge [d(x, y, t) = \text{active border}] \wedge [T(x, y, t) > \tau(v)] \rightarrow$   
 $\rightarrow d(x, y, t + \Delta t) = \text{passive border}$
- R4:  $[d(x, y, t) = \text{active border}] \wedge [d(x_{nn}, y_{nn}, t) = \text{non empty} \forall (x_{nn}, y_{nn})] \rightarrow$   
 $\rightarrow d(x, y, t + \Delta t) = \text{bulk precipitate}$

$$D_a(x, y) = \begin{cases} 0, & \text{if } d(x, y) = \text{passive border or obstacle} \\ D_a & \text{otherwise} \end{cases}$$

$$D_{b,c}(x, y) = \begin{cases} 0, & \text{if } d(x, y) = \text{non empty} \\ D_{b,c} & \text{otherwise} \end{cases}$$

Coordinates of the reaction field, that correspond to a gel sheet, are denoted by  $x$  and  $y$ , while  $t$  denotes time and  $\Delta t$  the time step. Terms  $a(x, y, t)$  and  $b(x, y, t)$  represent the reacting ions of the outer and inner electrolytes,  $c(x, y, t)$  the diffusive intermediary compound DC,  $c^{**}$  the nucleation threshold and  $c^*$  the growth threshold.  $[R]$  symbolises the coupling with the cellular automata rules.

The term  $d(x, y, t)$ , denoting the precipitate, is not related to concentrations. It can take just a few (arbitrary) values, denoting the bulk precipitate, the active borders, the passive borders, as well as the ‘‘empty’’ regions free of precipitate. The obstacles are inert cells, where none of the compounds can penetrate by diffusion.

$T(x, y, t)$  represents the age, while  $\tau(v)$  the maximal lifetime of the cells, where  $v$  denotes the speed of the precipitation front. In general, the maximal lifetime is assumed to depend on the front speed  $v$ . Nearest neighbors of the cell at the lattice point  $(x, y)$  are denoted by  $(x_{nn}, y_{nn})$ . The symbol ‘ $\wedge$ ’ represents the logical ‘and’.

Initially, the reaction field contains only the compound  $b$  having a uniform concentration  $b_0$ , as well as some inert and impermeable obstacles. Reagent  $a$  has the concentration  $a_0$  along the  $x = 0$  edge, and zero-flux boundary conditions on the other edges of the reaction field. All the other compounds have zero-flux boundary conditions on the entire edge of the reaction field.

The Laplace operator in the diffusion term is denoted by  $\Delta$ . Diffusion coefficients of the reagents in the regions free of precipitate are  $D_a$  and  $D_b$ , that of the DC is  $D_c$ . In our model, the diffusion coefficient of the outer electrolyte is zero on the passive borders, that is, it cannot cross these surfaces. The inner electrolyte is unable to diffuse in the precipitate. However, alterations of  $D_b$  on the passive borders as well as in the bulk precipitate do not change the character of the simulation results. The precipitate cannot

diffuse at all. The reaction, having rate constant  $r$ , is supposed to be proportional to the reagent concentrations.

The meaning of the cellular automata rules are as follows:

The appearance of new precipitation fronts is encoded by Rule 0. If in a point of the reaction field there is no precipitate or obstacle (“empty” point), and concentration of  $c$  exceeds the nucleation threshold  $c^{**}$ , new front segments (active cells) appear.

Rule 1 describes the progress of an active border. If the concentration of the DC exceeds the growth threshold  $c^*$  at a cell of the active border, all the nearest neighbors of the cell which are “empty”, become active. On a square lattice these are the first Neumann-type neighbors. The DC is assumed to be consumed during the activation process, and therefore it is eliminated from a cell that activated its surrounding.

The model assumes that only the surface of the precipitate can act as a region where precipitation can happen. Therefore, the cell that has activated its surrounding has to become passive. This consequence is also included in rule 1.

Rules 2 and 3 implement the assumption that the concentration of the DC has to reach the growth threshold  $c^*$  within time  $\tau(v)$  measured from the emergence of the active cell, otherwise the element will be passivized. Aging of the cell is described by rule 2, and passivization at the end of its lifetime is governed by rule 3. Investigated forms of the function  $\tau(v)$  are discussed in the Simulations section.

Rule 4 describes the second way of passivization, which is an extension of the passivization algorithm of rule 1. Cells of the active border are passivized in any configuration, when they become surrounded by either active or passive cells. Note that an active cell surrounded by precipitated cells and portions of the obstacle also gets passivized.

In the computational implementation of the model, the differential equations are applied first, the cellular automata rules afterwards. The rules act in the order R0-R1-R2-R3-R4.

Progression of the active borders proceeds in the following way: The reaction produces the DC, while reagents  $a$  and  $b$  are depleted in the surrounding. Since the outer electrolyte cannot cross the passive borders, the reaction is taking place mainly ahead of the active borders. Due to the reaction, the concentration of DC will rise at the active border, while the age  $T$  of the cells at the front is also increasing. Let us assume that the growth threshold  $c^*$  is reached before the age of the cells exceeds the lifetime  $\tau(v)$ . Usually this happens at the same time in a larger front segment. At this moment, the first neighbors of the active cells (which in this configuration are the next row of cells) become active, while the “mother-cells” get passivized. At the same time the DC gets depleted in the passivized cells, but while its diffusion rate for the passivized cells is zero, the magnitude of the DC in these cells has no influence on the simulation results.

Splitting of an active border in segments may happen when it overtakes an obstacle. During this event, the front can behave in two different ways: Either an active-passive transition occurs, and the front, having just overtaken the obstacle, splits and the resulting front segments shrink, or passivization does not occur, and the front reconnects behind the obstacle. In order for the splitting to occur, the concentration of DC around the endpoints of the active border segments has to be lower than the constant value

in the middle of them. In this case, the active cells around the endpoints will not be able to activate their surrounding when the central segment of the front does. However, these cells remain permeable for the outer electrolyte, but at appropriate parameter values the growth threshold  $c^*$  will not be reached along them in their lifetime  $\tau(v)$ . As a consequence, they will be passivized when their age  $T$  reaches  $\tau(v)$ .

In order for the shrinking of active border segments to occur, the concentration of DC around their end points has to be permanently lower than the constant value in the middle. Computer simulations showed that this situation is typical for a wide range of parameters. Due to the mechanism presented above, the cells around the end points are getting passivized, the active border segments are shortened and finally disappear, leaving behind precipitate triangles.

In order to increase numerical precision, decreasing the mesh size of the space discretization may appear desirable. However, if physical parameters have to be kept constant, rules 1 and 4 need to be changed. Several rows of active cells have to emerge at the same time, and not only the border cells can be active. Such extensions of the model have not been investigated. Decreasing of the time step does not cause similar problems.

## 4.2 Simulation Results

Computer simulations were performed on a rectangular grid using the finite volume method [162]. The boundary conditions are described in the previous section. The size of the time step was 0.05 while that of the mesh size of 1.0. Since the detailed chemical mechanism of the reactions is unknown at the moment, the parameters are not experimentally measured values.

Two versions of the model were investigated, namely when  $\tau(v)$  is constant or has a simple dependence on the front speed  $v$ . In both cases, the active border arised at the  $x = 0$  edge just after the simulations were started. In order to initiate front splitting, two obstacles were placed at equal distances from the  $x = 0$  edge. When the precipitation front overtakes the obstacles, an active-passive transition can occur: the active border splits and begins to shrink, leaving behind a trapezoid-shaped precipitate region, that finally evolves into a triangle. Although the version when  $\tau(v)$  is constant is able to reproduce formation of precipitate triangles (Fig. 4.1), it has a major disadvantage. Except some transients, position  $x$  of the precipitation front increases with time as  $x \propto \sqrt{t}$ , and the speed  $v$  of the front is proportional to  $1/\sqrt{t}$ . The age  $T$  at which the active cells are passivized is inversely proportional to  $v$ , consequently  $T \propto x$ . Therefore at some distance  $x$  the age  $T$  reaches  $\tau$ , a passive border forms and the front stops. Thus, when  $\tau$  is constant, the front is unable to travel to an arbitrary distance, while experimental findings indicate the contrary. Moreover, the parameter range where formation of triangle-like patterns occurs, is thin.

This problem can be avoided in the simplest way by setting the lifetime  $\tau(v)$  of an active cell to  $T_{\text{previous}} + \tau_0$ , where  $T_{\text{previous}}$  is the age of the “mother cell” cell that

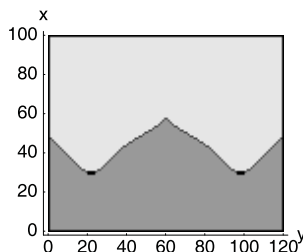


Figure 4.1: Precipitate triangle formed when  $\tau(v)$  is constant. The simulation was performed on a rectangular grid of  $120 \times 100$  units. Dark gray represents the bulk precipitate, and light gray the regions free of precipitate. Passive borders and obstacles are drawn in black, while the active borders in white. The parameters are the following:  $D_a = 3.0$ ,  $D_b = 1.0$ ,  $D_c = 0.3$ ,  $r = 0.1$ ,  $c^{**} = 11.0$ ,  $c^* = 10.0$ ,  $\tau = 8.0$ ,  $a_0 = 40.0$ ,  $b_0 = 10.0$ . The obstacles are rectangles of  $4 \times 2$  units, placed at  $x = 30$ ,  $y = 22$  and  $y = 98$ , respectively. Note that a small cusp, referred to as the “Meinhardt-peak” is formed at the top of the precipitate triangle. The mechanism of cusp formation has not been investigated in detail.

activated it, and  $\tau_0$  is a positive constant. The addition of  $\tau_0$  is necessary because the newly activated cells need more time to reach  $c^*$  than their “mother cells” did. This kind of  $\tau(v)$  is capable of producing triangles of an arbitrary size, in a wide range of parameters (Fig. 4.2). Note that bending of precipitation front when facing a small obstacle has also been observed. The results do not change significantly if diffusion of the inner electrolyte is allowed in the precipitate with a reduced, but nonzero rate.

Finally we mention that similar patterns can be obtained using an alternative model in which the outer and inner electrolytes react to form a precipitate. In this model, the precipitate can have different concentrations, and at appropriate parameter values, it will have an increased value around the end points of the active border. By assuming that above a concentration threshold the precipitate is impermeable, formation of the triangular patterns has also been achieved.

### 4.2.1 Digression: The Chemical Needle Effect

In a previous version of the mathematical model it was assumed that the sweeping active border acts as a catalytic surface where the DC is formed, while both kinds of bordering surfaces of the precipitate are permeable for all of the reagents [158]. At the beginning of the research a simplified system had been studied, where the reactions are catalysed by a stationary segment, having a constant length. The investigations performed on this system led to a surprising result: under ideal, diffusion-limited conditions, the amount of the product formed in unit time tends to infinity as we approach the end points of the catalytic segment. This scenario shows a similarity with the needle effect in electrostatics, and thus, it was referred to as the “chemical needle effect”.

Computer simulations were performed on a rectangular grid, using the finite difference, as well as the finite volume scheme. Reagents  $a$  and  $b$ , having initially constant

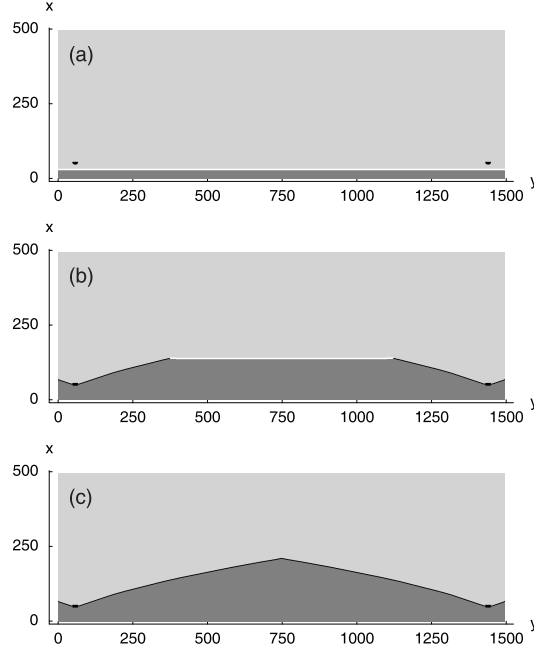


Figure 4.2: Precipitate triangle formed when  $\tau(v) = T_{\text{previous}} + \tau_0$ . The simulation was performed on a rectangular grid of  $1500 \times 500$  units. Meaning of the colors is the same as in Fig. 4.1. The obstacles are semicircles with radii of 10 units, placed at  $x = 60$ ,  $y = 60$  and  $y = 1440$ , respectively. The parameters are the following:  $D_a = 3.0$ ,  $D_b = 1.0$ ,  $D_c = 0.8$ ,  $r = 0.1$ ,  $c^{**} = 9.0$ ,  $c^* = 7.0$ ,  $\tau_0 = 2.0$ ,  $a_0 = 40.0$ ,  $b_0 = 10.0$ . The thickness of active and passive borders has been enhanced on this figure. (a.) Traveling precipitation front shortly after it appeared. The time elapsed from the beginning of the simulation is  $t = 90$ . (b.) A trapezoid-shaped precipitate region is growing in the central area, having a shrinking active border. Note the short transient (the passive border is slightly bent) in the vicinity of the obstacles that caused the active-passive transition. The time elapsed is  $t = 1480$ . (c.) The reactions are over, the precipitate triangle has been completed.

concentrations  $a_0$  and  $b_0$ , were allowed to react and form the compound  $c$  only on a stationary, straight segment  $s$  located in the middle of the grid. The reagents could reach the catalytic segment by diffusion. Equations of the simplified system presented above are the following:

$$\frac{\partial a(x, y, t)}{\partial t} = D_a \cdot \Delta a(x, y, t) - ra(x, y, t)b(x, y, t) \cdot \delta(s) \quad (4.4)$$

$$\frac{\partial b(x, y, t)}{\partial t} = D_b \cdot \Delta b(x, y, t) - ra(x, y, t)b(x, y, t) \cdot \delta(s) \quad (4.5)$$

$$\frac{\partial c(x, y, t)}{\partial t} = D_c \cdot \Delta c(x, y, t) + ra(x, y, t)b(x, y, t) \cdot \delta(s) \quad (4.6)$$

Here  $D_{a,b,c}$  denoted the diffusion coefficients,  $r$  the reaction rate, and  $\delta(s) = 1$  only on the catalytic segment, being zero elsewhere.

The distribution of the compound  $c$  that appears in march time step  $\Delta t = 0.01$  is represented in fig. 4.3 (a.). This shows a singularity at the end points of the reactive segment. This can be explained as follows. The local production rate of  $c$  at a certain point of the reactive segment is proportional to the influx of the reagents to that point, while the influx rates depend on the local concentration gradients of the reagents. The latter are found to be maximal at the end points of the segment.

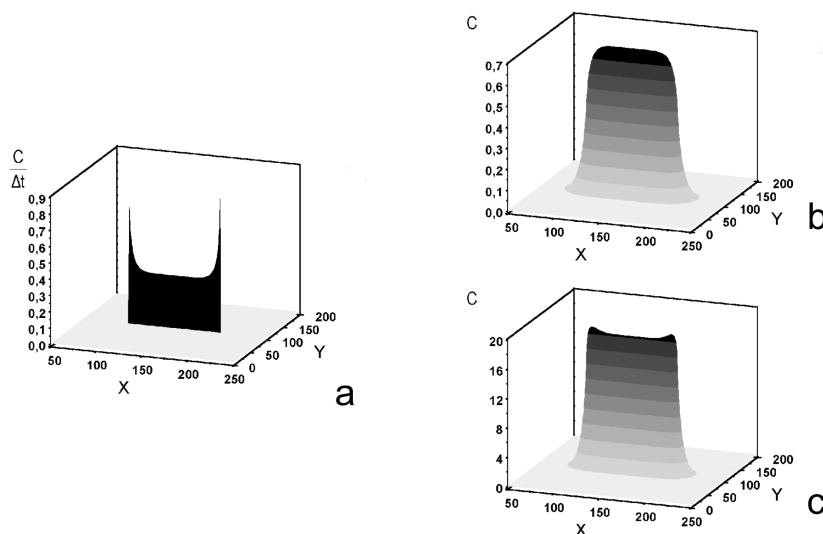


Figure 4.3: Computer simulation of concentration profiles of the compound  $c$  around a stationary reactive segment. All units are dimensionless. The simulations were performed with the finite difference scheme, on a rectangular grid of  $300 \times 200$  units. The reaction  $a + b \rightarrow c$  runs on a band of unit width and 100 units of length, located in the middle of the grid ( $x = 100..199$ ,  $y = 100$ ).  $t = 5$  time units elapsed from the start of the reaction. (a.) Chemical needle effect: the reaction product formed in  $\Delta t = 0.01$  drastically increases by approaching the end points of the reactive segment.  $r = 1$ ,  $D_a = 23$ ,  $D_b = 20$ ,  $D_c = 10$ ,  $a_0 = 30$ ,  $b_0 = 15$ . (b.) Bumps are not present at the ends of the reactive segment.  $r = 1$ ,  $D_a = 23$ ,  $D_b = 20$ ,  $D_c = 18$ ,  $a_0 = 3$ ,  $b_0 = 1.5$ . (c.) Bumps are formed near the end points of the reactive segment. Note that before the end points the concentration of  $c$  falls below the constant value that was reached in the middle of the segment. The parameters are the same as in (a.).

Depending on the parameters, distributions of the total amount of compound  $c$  can be classified into two important categories. The concentration either decreases monotonically as we approach the end points of the reactive segment (fig. 4.3 (b.)), or it will have two “bumps” before the end points (fig. 4.3 (c.)). According to the simulation results, bumps appear when the diffusion coefficient of  $c$  is smaller than the diffusion coefficient of each of the reagents. This condition is not a sufficient, but only a necessary requirement. An analytical explanation of the overall distribution of  $c$  is under investigation.

The previous version of the mathematical model designed to reproduce the formation of the triangular precipitate patterns, was able to show, due to the chemical needle effect, formation of Meinhardt peaks at the top of the triangles. A necessary requirement for the Meinhardt peaks to form is the presence of significantly high bumps on the concentration profile of the diffusive intermediary compound. When the precipitation front becomes so short that the two bumps of the DC touch each other, the time necessary for the production of the critical concentration of the DC is shortened, and the front propagation speed increases. As a result, at the top of the precipitate triangle the Meinhardt peak appears.

### 4.3 Discussion and Open Questions

Computer implementations of the mathematical models presented above are able to reproduce the main features of the formation of primary patterns: front initiation at the beginning of the experiments, front splitting, as well as the development of trapezoid-shaped regions that finally evolve to triangles of precipitate. Thus, it is shown that the existence of the passive (impermeable) borders can naturally lead to a special distribution of the DC, its concentration being smaller around the end points of the active borders, and, as a consequence, to the formation of the triangular precipitate patterns observed in the experiments.

A previous model was also able to reproduce the formation of precipitate triangles, but only in special circumstances, namely in the case when both reagents are present in the reaction field [158]. Moreover, it was assumed that the reaction is taking place only on the active border, having catalytic properties. The present models have more simple assumptions. However, the formation of Meinhardt peaks has been understood only in the previous model.

The experiments performed up to this time could not explore the whole reaction mechanism. Beside others, the nature of passive border formation is unclear. Regarding the hypothesis of 'aging', its microscopic explanation is unknown, as well as the dependence of the lifetime  $\tau(v)$  on the front speed. The molecular mechanism of the ion-selectivity of the passive borders has not been revealed. The passive borders may only restrain the diffusion of the outer electrolyte's reacting ion, or may prohibit the crossing of some other species of ions as well. The dependence of the diffusion coefficients on the concentrations [191] is also not included in the model. The parameters of the model are estimates, and not experimentally measured values.

As mentioned earlier, slightly different versions of the model led to the same ability of reproducing the front initiation and pattern formation. This shows that the model has a remarkable robustness.



# Chapter 5

## Secondary Patterns: Experiments and a Hypothesis

A large number of chemical systems have been tested to find out whether they can yield fine patterns, which can be useful in several technological processes. Up to now, the characteristic size of the finest regular structures produced by chemical reaction-diffusion systems was of the order of millimeters [119]. These patterns were produced by the Liesegang phenomenon. However, diffusion-controlled reactions in solids can lead to periodic banding having a wavelength of the order of  $10\mu m$ . These bands of particles are located in a continuous intermetallic matrix phase [6, 192].

The reactions  $NaOH + CuCl_2$  and  $NaOH + AgNO_3$  are also capable of producing regular microscopic structures: a more careful look at the precipitate formed in these processes reveals that under certain circumstances it may be composed of parallel sheets of colloidal precipitate. These microscopic structures are referred to as *secondary patterns* [160].

### 5.1 The Scenario of the Formation of Secondary Patterns

In order to study the details of the formation of secondary patterns, the reaction was started in thin gel sheets and followed with an optical microscope. PVA gel containing  $0.732 M CuCl_2$  was located between a slide and a cover glass, and  $8.0 M NaOH$  solution was allowed to diffuse into the gel from the edge of the gel sheet. In this way a reaction-diffusion front forms, that sweeps through the gel.

The reaction-diffusion front of the  $NaOH$  is assumed be the source of a compound that phase separates into high-density ( $CuO$  precipitate) and low-density (free of precipitate) stripes. Although the source front is not visible, it is followed by a sharp precipitation front, where a blue-green compound is formed that shows no structure when investigated with an optical microscope [160]. This is referred to as the 'active border' of the blue-green precipitate, it can easily be observed even by the naked eye,

and is likely to follow the shape and the speed of the source front.

The velocity of the precipitation front is mainly determined by the speed of the diffusion front and the shape of the precipitation front itself. The velocity of the diffusion front decreases in time, roughly by a square-root law. As mentioned earlier, the syneresis of the PVA gel influences the progression of the outer electrolyte's diffusion front. However, this effect is not so significant for thin gel sheets between a slide and a cover glass. When a new precipitation front emerges, after a transient period of greater velocity, its speed becomes diffusion-limited. The shape of the front is also important. A convex segment of a precipitation front is slower than a straight segment, which is in turn slower than a concave segment. This behavior is in agreement with the predictions of the kinematical theory of chemical waves. However, quantitative measurements establishing a connection with the *eikonal equation* have not been performed yet.

Velocity plays an essential role in determining which kinds of secondary, microscopic patterns are formed as the front advances. The main characteristics of the precipitation that emerge at various front speeds are as follows [160]:

(a) If the velocity of the front is higher than  $2.1 (\pm 0.6) \mu\text{m}/\text{s}$ , colloidal precipitate does not appear, either ahead the active border, or behind it. The density of the blue-green precipitate that forms behind the active border is also much reduced.

This happens, for example, at the meeting point of two precipitation fronts (figs. 5.1 (a.)-(b.)). If two precipitation fronts moving towards each other meet, they form a single, fused front. In the proximity of the meeting point the front speed is significantly higher, and a region free of brown precipitate remains after the reaction is complete (fig. 5.1 (b.)). The highest front velocity measured was  $12.5 \mu\text{m}/\text{s}$ . Note that the blue-green precipitate shows no structure when investigated with optical microscopy.

(b) At slower velocities of the active border, in general between  $0.9$  and  $1.8 \mu\text{m}/\text{s}$ , a brown colloidal precipitate emerges in the blue-green precipitate,  $7 - 8 \text{ min}$  after the front has swept through a gel region (fig. 5.1 (a.)). The uniformly distributed brown colloid, that turned out to be  $\text{CuO}$ , fills the space where the blue-green precipitate was present, except for the blind regions near the previous passive borders (fig. 5.1 (b.)). Note that in this case no grainy colloidal precipitate forms in the immediate proximity of the active border.

(c) If the velocity decreases further, a remarkable new phenomenon takes place. A homogeneously distributed colloidal precipitate, referred to as the *A-type colloidal precipitate*, emerges just ahead of the active border (fig. 5.1 (c.)). The site where the A-type colloids form will be referred to as the *colloidal front*. Thus, the colloidal front precedes the active border (precipitation front).

The uniformly distributed A-type colloidal precipitate forms in the majority of cases at front velocities between  $0.6$  and  $0.9 \mu\text{m}/\text{s}$ . A few minutes later it converts to the brown  $\text{CuO}$  colloid (fig. 5.1 (d.)). Note that in dark-field microscopic investigations the A-type colloids shine in white, while the  $\text{CuO}$  precipitate appears brown (fig. 5.1 (e.)). A detailed investigation of the process of the formation of the A-type colloids showed that this occurs in two steps. First, very small colloidal particles, referred to as A-type dust, are formed, and these then undergo a ripening process giving rise to

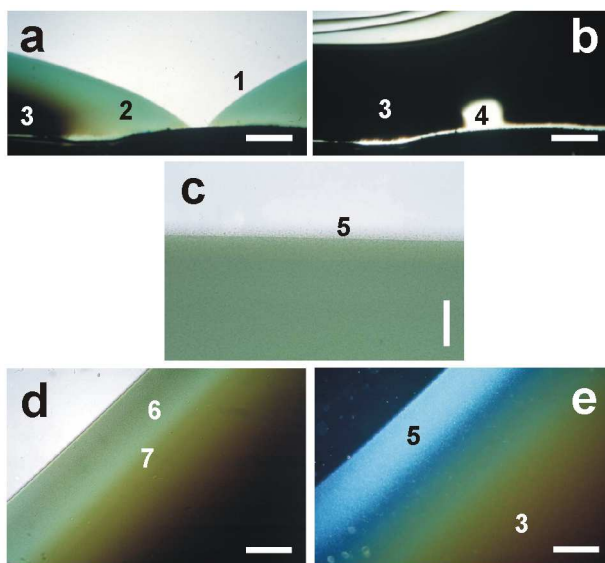


Figure 5.1: (a.) Two approaching active borders (1) before they meet. The green precipitate (2) can be observed behind the active borders. Note that the picture was taken in transmitted light, which is the reason for the green color of the “blue-green” precipitate. No A-type colloids are present ahead of the active borders. The brown *CuO* colloid (3) emerged in the regions where the active border swept through 7–8 min earlier. Thicker layers of the brown precipitate absorb the light, and look black. Scale bar = 800  $\mu\text{m}$ . (b.) The same scenario after the termination of the reactions. The place where an active border swept through is thickly filled with the brown precipitate (3), except in region (4) next to the meeting point, where the front velocity was higher by about 2.1  $\mu\text{/s}$ . Scale bar = 800  $\mu\text{m}$ . (c.) Homogeneously distributed A-type colloids (5) emerged just before the active border. Scale bar = 50  $\mu\text{m}$ . (d.) Decay of the A-type (6) and emergence of the brown (7) colloidal precipitate. Scale bar = 200  $\mu\text{m}$ . (e.) The same patterns in dark-field investigation. The A-type colloids shine in white (5), while the brown precipitate appears brown (3). Scale bar = 200  $\mu\text{m}$ . The outer electrolyte was  $a_0 = 8.0 \text{ M NaOH}$ , while that of the inner electrolyte was  $b_0 = 0.732 \text{ M CuCl}_2$ .

particles having a greater diameter, referred to as A-type grains.

(d) When the front velocity slows further, usually to 10–40 % below the value where the uniformly distributed A-type colloids first appear, the precipitate starts to show pattern (fig. 5.2 (a.)): a regular structure of parallel stripes of A-type colloidal precipitate appears approximately one wavelength distance ahead of the active border. At this stage, the dark-field investigations show clearly the A-type dust that is undergoing a ripening process (fig. 5.2 (d.)). Later the particles making up these stripes are converted into brown *CuO* (figs. 5.2 (b.) and (c.)). Note that this kind of patterning is strikingly different from the mechanism of the Liesegang phenomena.

The wavelength of the secondary patterns is correlated with the velocity of the active border. Larger front velocity leads to smaller wavelength. The smallest wavelength

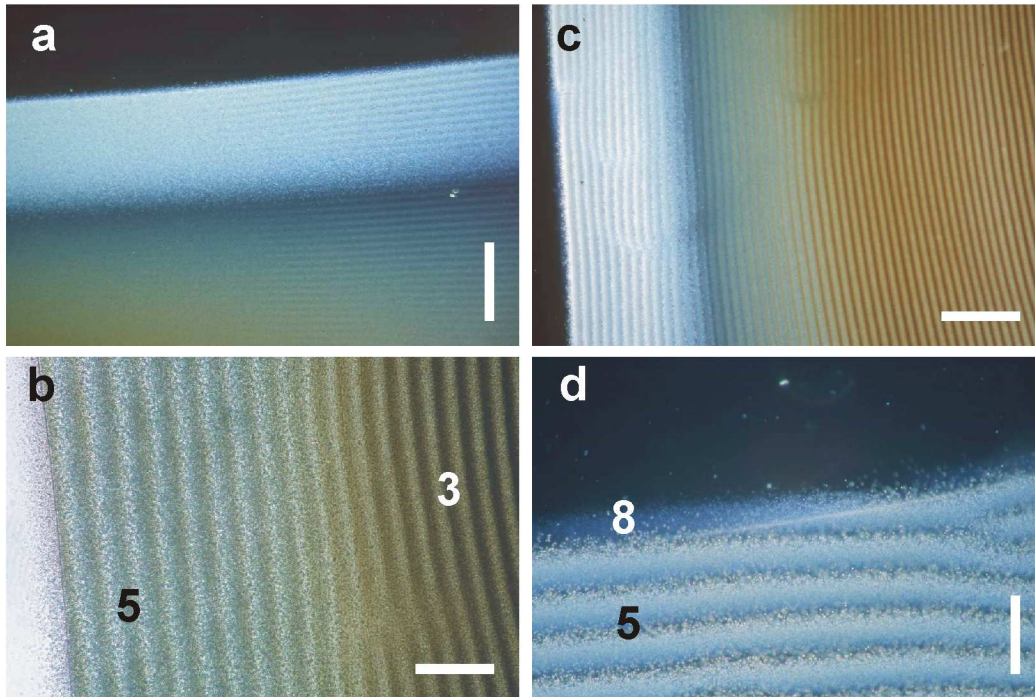


Figure 5.2: (a.) Dark-field investigation just when the A-type colloidal precipitate starts to show patterns. Scale bar =  $200 \mu\text{m}$ . (b.) Two main stages of the formation of the stripes of precipitate. The A-type colloidal precipitate (5) forms ahead of the active border and transforms into a brown (3) precipitate. Scale bar =  $100 \mu\text{m}$ . (c.) Similar patterns in dark-field investigation. Scale bar =  $200 \mu\text{m}$ . (d.) Dark-field investigation of the formation of a stripe. First the small sized A-type dust is formed at the colloidal front (8), which then ripens to form larger A-type grains (5). Scale bar =  $100 \mu\text{m}$ .  $a_0 = 8.0 \text{ M NaOH}$ ,  $b_0 = 0.732 \text{ M CuCl}_2$ .

observed in the  $\text{NaOH} + \text{CuCl}_2$  system was  $15 \mu\text{m}$ , while the largest was  $150 \mu\text{m}$ . The  $\text{CuO}$  precipitate stripes are mostly parallel to the reaction-diffusion front (*lamellar morphology*, LM), but in some cases they form an angle with the front. This latter kind of pattern is referred to as an *oblique morphology* (OM).

All the above effects can be seen in (fig. 5.3 (a.)): from the upper to the lower part of the figure, the speed of the diffusion front decreases. The regions are initially free of colloidal precipitate, then have homogeneous brown colloidal precipitate, and finally precipitate stripes with slightly growing wavelength appear. Note that at the present time the functional form of the connection between the front velocity and the wavelength of the patterns is unknown.

Regular secondary patterns are not specific to a single chemical system. Their formation has also been observed in PVA gels without cross-linking. Emergence of similar regular grids has been observed in the  $\text{NaOH} + \text{AgNO}_3$  reaction-diffusion system in PVA gel also. Note that in this reaction the minimal wavelength of the pattern was



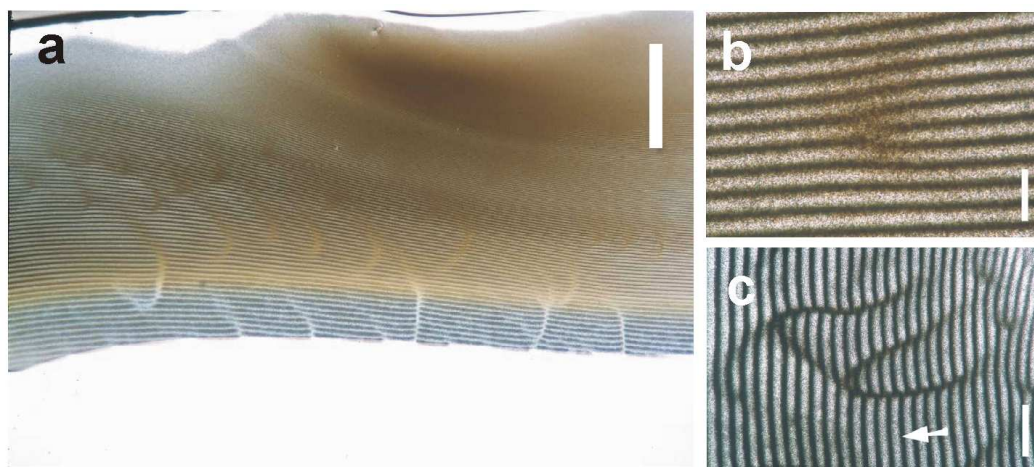


Figure 5.3: (a.) Development of secondary patterns where several defects are also present. Scale bar =  $800 \mu m$ . (b.) Fork-like defect in a gel sheet. Scale bar =  $50 \mu m$ . (c.) Interactions of elongated defects: two defects forming successively closer to each other are annihilated, or only one of them survives. The arrow indicates the direction of propagation of the active border which yields this pattern. Scale bar =  $200 \mu m$ .  $a_0 = 8.0 M NaOH$ ,  $b_0 = 0.732 M CuCl_2$ .

only  $4 \mu m$  (fig. 5.4).

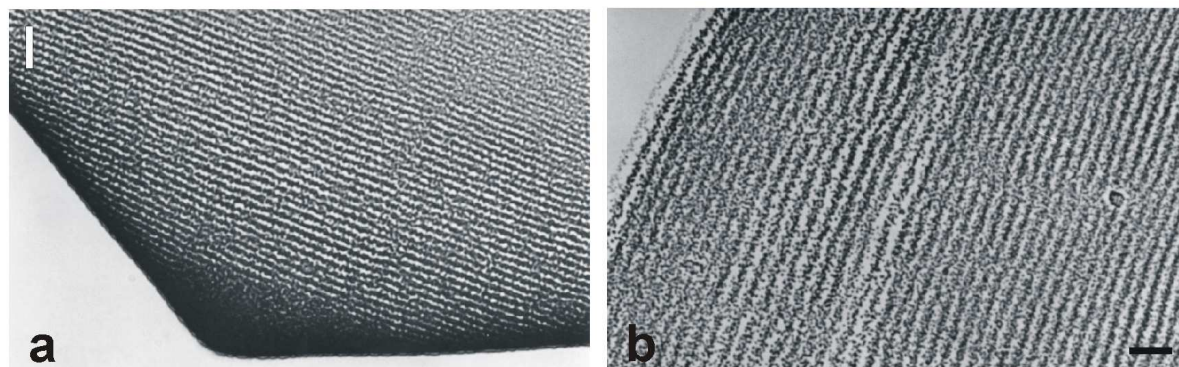


Figure 5.4: Secondary patterns formed in the  $NaOH + AgNO_3$  reaction in PVA gel. The reaction takes place between a microscope slide and a cover glass.  $a_0 = 8 M NaOH$ ,  $b_0 = 0.56 M AgNO_3$ , scale bar =  $25 \mu m$ . (a.) Precipitate grid that is part of a primary pattern as well. The reactions have finished. (b.) A new stripe of colloidal precipitate is just forming.

## 5.2 Defects in the Secondary Patterns

The secondary patterns, that are stripes consisting of colloidal particles, are not free of defects (fig. 5.3 (a.)). An interesting dynamical feature of the reaction is the emergence and interaction of defects. They usually appear when there are slight differences in the velocity between some parts of the active border. In most cases, the differences are not high enough to cause significant changes in the wavelength of the grid, but the front segment, having greater velocity, yields more precipitate stripes than segments with a smaller velocity. If the wavelength is approximately constant, all the stripes cannot be continuous along the active border. At the part of the front with higher speed, new stripes are inserted, and interstitial fork-like defects are formed (fig. 5.3 (b.)). Although several types of defects have been observed in chemical and physical systems, the fork-like errors show most of the common features of defects present on the patterns of some sea shells, like those of *Nautilus pompilius* [46]. This animal bears a spiral-shaped shell, that results from much faster growth on the periphery of the growing edge. The number of pigmented lines on the peripheral region is higher than along the inner side, and the interconnections of the pigmentation lines are similar to the fork-like errors presented above.

Another common type of error is the so-called elongated defect (fig. 5.3 (c.)). If the distance between two elongated defects growing towards each other decreases by about 2-3 wavelength, an effective attractive interaction appears between them. After they meet, one or both of them will disappear. A possible explanation of this behavior is given in section 4.4.

## 5.3 Oblique Striping

In the case of the lamellar morphology, the stripes appear one by one along the source front, that is, their growth does not proceed via the elongation of their end points. In contrast, in the case of the oblique morphology, the stripes have growing endpoints in the wake of the source front, and they form an angle with the envelope of their terminal points<sup>1</sup>.

The first emerging stripes will be parallel to the active border. When the source front does not change its shape and orientation, the subsequent stripes will form parallel to the previous stripes and the front as well, giving rise to a lamellar morphology. According to video microscope observations, a possible scenario for the formation of the oblique stripes is the following [202]: When the source front suddenly changes its shape or orientation, *e.g.* as a result of an influx of the outer electrolyte from a new direction, the newly formed stripes cannot follow the front's altered orientation, but form more or less parallel to the previous ones. The newly formed stripes elongate only up to the limit of the region already visited by the source front, with the envelope of their growing

---

<sup>1</sup>The spiral patterns in the classical two-dimensional Liesegang experiments [119] can also be considered as a special case of the oblique morphology.

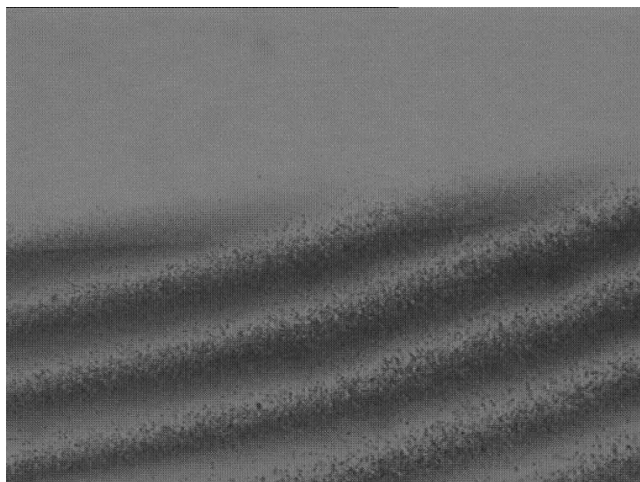


Figure 5.5: Stripes of colloidal  $CuO$  grains of oblique morphology. The precipitate structures form as a result of  $8\text{ M NaOH} + 0.586\text{ M CuCl}_2$  reaction in a thin PVA gel sheet of about  $0.2\text{ mm}$  thickness, located between a microscope slide and a cover glass. The width of the figure is  $0.58\text{ mm}$ . The sharp straight line shortly below the endpoints of the stripes represents the active border of the system.

endpoints being parallel to the actual position of the front (fig. 5.5).

## 5.4 Experiments in Gel Columns

The formation of regular sheets of colloidal precipitate instead of stripes can also be achieved by having the reactions run in gel columns instead of gel sheets. In order to obtain several hundred consecutive thin layers consisting of colloidal particles, it is necessary to avoid the formation of the primary patterns that split and distort the secondary patterns. The main advantage of doing the experiments in gel columns is that the formation of primary patterns can be easily repressed. Moreover, the most regular grids consisting of colloidal precipitate can be obtained by sectioning a gel column containing only secondary patterns.

The formation of secondary patterns depend on the speed of the precipitation front. However, the latter depends on the experimental setup as well as on the reactant concentrations. Using  $6.00\text{ mL}$  of  $8\text{ M NaOH}$  solution as the outer electrolyte and gel columns of  $14.2\text{ mm}$  inner diameter and  $100 - 120\text{ mm}$  height, the secondary patterns (layers consisting of colloidal precipitate) appear only if the concentration of the  $CuCl_2$  inner electrolyte is higher than about  $0.7\text{ M}$ , because it has to be high enough to slow the active border to the speed where the formation of the secondary patterns can occur. Unfortunately at these concentrations primary patterns are also present, so the sheets of the secondary, microscopic patterns are split by the primary ones.

A method of generating primary patterns at concentrations at which, under normal initial conditions, they do not normally appear has been discussed in section 2.3.3: When

the  $CuCl_2$  concentration is in a range underneath a certain threshold, the formation of primary patterns could be achieved only by increasing the  $CuCl_2$  concentration at the top of the gel. If the reverse phenomenon would work, it would be possible to inhibit the formation of primary patterns at concentration ranges where secondary patterns are forming. Detailed experimental investigations show that this is possible<sup>2</sup>: if the concentration of the  $CuCl_2$  is lower than  $1.11 (\pm 0.05) M$ , the formation of primary patterns can be suppressed. The suppression of the primary patterns can be achieved by decreasing the inner electrolyte concentration at the top region of the gel column by pouring an aqueous solution of  $HCl$  with  $pH = 1.2$  onto the gel, and keeping it there for  $24 h$  before the reaction is started.

Thus, when  $NaOH$  solution is poured on the top of the gel column, the precipitation front penetrates first into the gel region that is not stimuable, *i.e.* where the  $CuCl_2$  concentration is not high enough for the regressing edges to appear, and primary patterns will not form. After the front reaches  $3 - 4 cm$  below the top of the gel column, where the concentration of  $CuCl_2$  is unchanged and high enough to generate primary patterns, primary patterns will in fact not appear. This method of suppressing primary patterns does not work if the original inner electrolyte concentration is higher than  $1.11 (\pm 0.05) M$ . Above this value, primary patterns emerge when the front passes through the gel region with decreased  $CuCl_2$  concentration.

When the formation of primary patterns is suppressed, in the above experimental setup the secondary patterns appear when the concentration of the inner electrolyte is greater than about  $0.8 M$ . The most regular sheets of colloidal precipitate are obtained with  $CuCl_2$  concentrations between  $0.87 M$  and  $0.96 M$  (figs. 5.6 (a.) and (b.)).

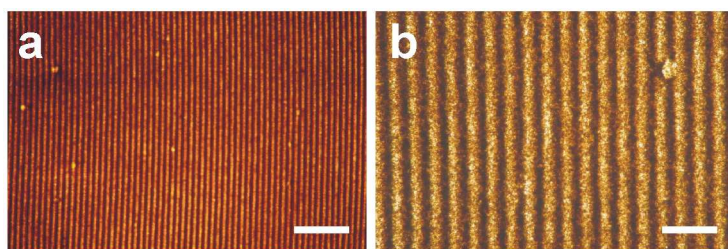


Figure 5.6: Cross-sections of systems of equidistant precipitate sheets at different magnifications. The difference in the shade of colors is due to the different thickness of the samples. (a.)  $a_0 = 8 M NaOH$ ,  $b_0 = 0.966 M CuCl_2$ . Scale bar=  $200 \mu m$ . (b.)  $a_0 = 8 M NaOH$ ,  $b_0 = 0.879 M CuCl_2$ . Scale bar=  $50 \mu m$ .

Although the wavelength of the patterns increases slightly as the velocity of the active border decreases, in this experimental setup this effect can be neglected for lengths of  $1 - 2 cm$ , containing several hundred sheets of precipitate. Note that due to the syneresis, the gel column does not adhere to the wall of the test tube approximately  $2 mm$  behind the active border. As a consequence, the outer electrolyte is carried by diffusion only in

<sup>2</sup>Thus, a hysteresis-like behavior is present in the system.



the last few millimeters, and the speed of the active border, and thus the wavelength, can be kept constant if the outer electrolyte is continuously refreshed.

The secondary patterns have got large regions free of defects only inside a cylinder of 3 – 4 mm diameter in the center of the gel column. Outside this region the wavelength decreases slightly as the radius increases, and therefore fork-like errors, sometimes in an ordered hexagonal or cubic lattice, appear. This is probably caused by the syneresis of the gel. Syneresis is also responsible for the nonplanar shape of the active border, that is slightly concave, causing a slight distortion of the precipitate sheets. These errors can be reduced by using larger test tubes.

## 5.5 Hypothesis and Computer Simulations

At the present stage of research the mechanism of secondary pattern formation is unknown, and thus, possible mathematical models can be deduced only by phenomenological assumptions. A promising way to model the formation of the secondary patterns is phase separation, shown by various chemical and physical processes [193–198]. Most of the studies on phase separation are concerned with initially homogeneous systems, where pattern formation starts after a temperature quench shifts the system into an unstable state. However, a new stream of research is being defined by studies where this process takes place in the wake of moving fronts.

Two mechanisms are known to yield spinodal phase separation behind traveling fronts. In the first, the concentration of the phase-separating compound is initially in the stable regime, and a source front shifting it in between the spinodal points can switch the system into the unstable, pattern-forming range. Alternatively, when the concentration lies between the spinodal points, the temperature should only drop below the critical value, required for the instability to occur, behind a quenching front. Some important aspects on these mechanisms are listed below.

Computational studies on phase separation under directional quenching are presented in [199] and [200]. The phase separation was studied in the framework of the Cahn-Hilliard equation. At high velocities of the cooling front, irregular morphology (IM) emerged. At decreasing front velocities, stripes parallel to the quenching front, that is, lamellar morphology (LM), and stripes perpendicular to the front, termed columnar morphology (CM) were found. Although little attention has been paid to the systematic investigation of the textures when the stripes were oblique to the front (OM), we will put a special emphasis on these kinds of patterns.

The examination of phase separation in the wake of source fronts has been motivated by the desire to set up a minimal model of the Liesegang phenomenon. Modeling the formation of the one-dimensional Liesegang patterns has been achieved by assuming that the reaction of the electrolytes yields an intermediary compound first, that separates into high and low density regions according to the Cahn-Hilliard equation [152, 154].

As follows, we investigate the formation of the microscopic, striped (“secondary”) patterns emerging in the  $NaOH + CuCl_2$  reaction running in PVA hydrogel sheets. The

main characteristics of the parallel and oblique morphologies observed in the experiments have been reproduced by computer simulations based on phase separation described by the Cahn-Hilliard equation [202].

### 5.5.1 Modeling the pattern formation in the wake of source fronts

The process of phase separation, occurring in the wake of the  $NaOH + CuCl_2$  reaction-diffusion front, has been modeled by the Cahn-Hilliard equation with a Ginzburg-Landau free energy [198]. Although one of the equilibrium densities of this free energy is negative, and therefore, in our case unphysical, the equation can easily be rescaled to a form where both equilibrium densities are positive. However, for the sake of simplicity and without offending the physical content, we have used the free energy with minima at  $-1$  and  $+1$ .

In order to focus our attention to the pattern formation, the reaction-diffusion system that produces the phase separating chemical has not been included in our model. In order to describe the source front, a Gaussian-type source term  $S(x, y, t; v)$  has been added to the Cahn-Hilliard Equation. The model represents the conserved order parameter dynamics (often referred as Model B dynamics) with an extra source term:

$$\frac{\partial c(x, y, t)}{\partial t} = -\Delta[c(x, y, t) - c(x, y, t)^3 + \epsilon \Delta c(x, y, t)] + S(x, y, t; v) \quad (5.1)$$

where

$$S(x, y, t; v) = A \cdot \exp[-\alpha(x + \beta - vt)^2]; \quad (5.2)$$

Initially, the concentration of the compound  $c$  is set to the stable magnitude  $c_0(x, y, 0) = -1 + \eta$  in the whole rectangular simulation area, where  $\eta$  is a random uniform deviate distributed between  $\pm 0.001$  [200]. This deviate has been added to the model in order to make it more realistic.

The value  $c_0$  is increased by the source, moving with constant speed  $v$ , to the constant value  $c_f$  [142]. The speed  $v$  of the source, as well as the concentration  $c_f$  next to the source front, are considered as independent simulation parameters. Having the speed  $v$  fixed, the value of  $c_f$  is determined by the amplitude  $A$  and the width  $\alpha$  of the Gaussian source. If  $c_f$  lies in between the spinodal points, that is,  $-1/\sqrt{3} < c_f < 1/\sqrt{3}$ , the system will be unstable against linear perturbations, and phase separation will take place in the wake of the front. As time goes on, the concentration profile  $c(x, y, t)$  tends to reach the equilibrium values, and a “ripening” of the regions with the stable concentrations will take place as well. However, the initial conditions, as well as the movement of the Gaussian-type source front will strongly affect the emerging patterns. These features will be our primary concern.

The equation (5.1) was solved on a rectangular grid using the finite difference

method<sup>3</sup>. Periodic boundary conditions have been used in both directions.

The time evolution of the system was computed by explicit simple time marching on a rectangular grid. The mesh size was  $\Delta x = \Delta y = 1$ , while the time step was  $\Delta t = 0.01$ . A negligible change in some selected simulation results was only observed when the mesh size was halved and the time step was diminished 10 times. It is also important to mention that the effect of the grid anisotropy on the simulation results was also of minor importance. This has been checked by comparing pattern formation in the wake of source fronts with different orientations.

### 5.5.2 Simulation results: source fronts traveling with constant speed

The speed of the source front, as well as the initial conditions, play a decisive role in determining the character of the pattern formation. Similar effects have been observed in other chemical systems as well [201]. In this section, our concern will be to investigate their influence.

Initially, the concentration was set to  $c_0(x, y, 0) = -1 + \eta$  in the simulation area. This was increased by the front to  $c_f$ , a value being in between the spinodal points. In the following, the results for the case  $c_f = 0$  will be presented, and major differences for  $c_f \neq 0$  will be mentioned.

In our investigations, the source fronts were traveling with different constant speed values. Although in the experiments the front speed varies in time, this change is usually not significant for 5–10 stripe wavelength, and the front speed can be considered locally constant.

Different pre-patterns with  $c(x, y, 0) = 0$  introduced in the  $x \in (5, 30)$  space units region of the simulation area highly affected the character of the patterns emerging even after the front sweeps through this region. Note that the source was started at  $x = 10$  space units from the  $Y$ -axis of the simulation area.

In the following, patterning at three different initial conditions are presented. The effects of the front speeds are also discussed within these cases (fig. 5.7).

a.) In the simplest scenario, the front is started parallel to the  $Y$ -axis of the rectangular grid, and sweeps with constant speed and orientation toward the opposite edge. The concentration is  $c_0(x, y, 0) = -1 + \eta$  all over the simulation area, that is, no initial patterning is introduced in the system. Depending on the front speed, two characteristic morphologies were observed.

If the front speed is higher than  $v \approx 5$ , an irregular morphology builds up in the wake of the front. The explanation is straightforward: the relatively slow phase separation drops behind the rapidly progressing front. As a consequence, there will be a

---

<sup>3</sup>We used the nine-point Laplacian  $\Delta c(x_i, y_j) = \frac{1}{6}[4c(x_{i-1}, y_j) + 4c(x_{i+1}, y_j) + 4c(x_i, y_{j+1}) + 4c(x_i, y_{j-1}) + c(x_{i-1}, y_{i-1}) + c(x_{i-1}, y_{j+1}) + c(x_{i+1}, y_{j-1}) + c(x_{i+1}, y_{j+1}) - 20c(x_i, y_j)]$  and the fourth order term was approximated by  $\Delta^2 = c(x_{i-2}, y_j) + c(x_{i+2}, y_j) + c(x_i, y_{j+2}) + c(x_i, y_{j-2}) + 2[c(x_{i-1}, y_{j-1}) + c(x_{i-1}, y_{j+1}) + c(x_{i+1}, y_{j-1}) + c(x_{i+1}, y_{j+1})] - 8[c(x_{i-1}, y_j) + c(x_{i+1}, y_j) + c(x_i, y_{j+1}) + c(x_i, y_{j-1})] + 20c(x_i, y_j)$

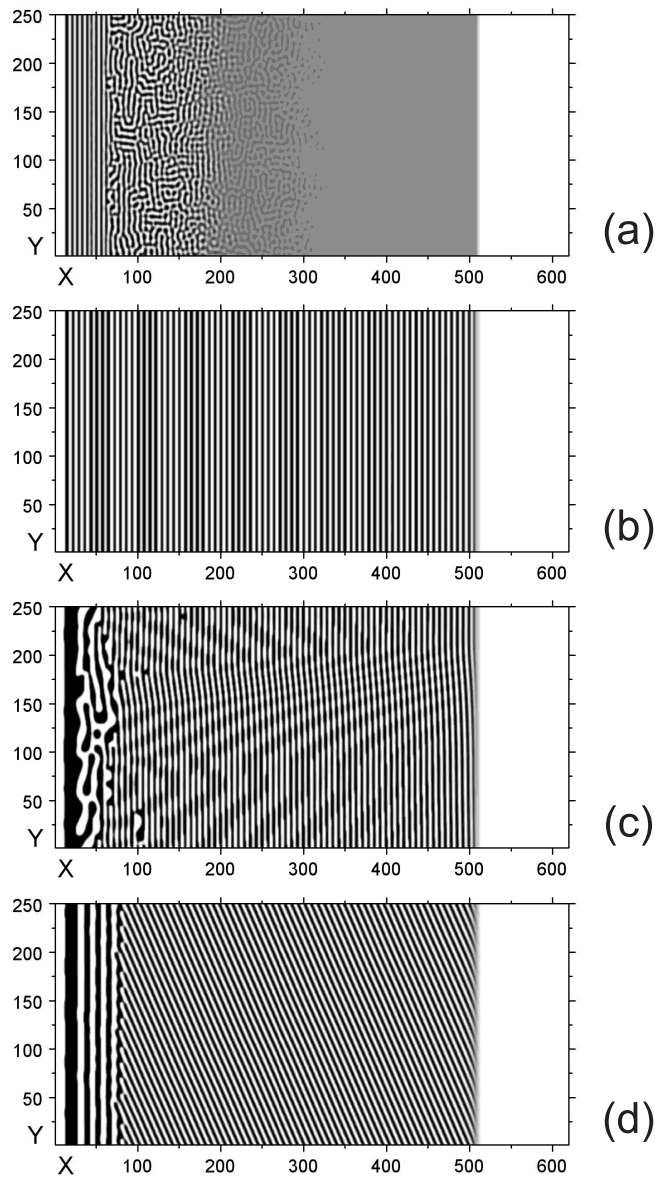


Figure 5.7: Pattern formation in the wake of source fronts traveling with constant speed. The dimensions of the simulation area are 250x620 space units.  $\epsilon = 0.5$ ,  $\alpha = 0.1$ ,  $\beta = 10$  in all the sub-figures. A gray scale has been used, with white as  $c = -1$  and black as  $c = +1$ . (a.) Random patterns formed far behind the front. Note the parallel striping that turns out in the wake of the random morphology.  $v = 10$ ,  $A = 1.78$  ( $c_f = 0$ ),  $t = 50$ . (b.) Regular lamellar patterns.  $v = 1$ ,  $A = 0.178$  ( $c_f = 0$ ),  $t = 500$ . (c.) Slightly disturbed lamellar morphology and oblique morphology with a small tilting angle formed when the first stripes were destroyed by random spots located in the  $x \in (5, 30)$  space units region.  $v = 1$ ,  $A = 0.178$  ( $c_f = 0$ ),  $t = 500$ . (d.) Oblique morphology formed when the  $x \in (5, 30)$  space units region was “pre-patterned” with tilted stripes forming an angle of about 30 degrees with the  $Y$ -axis and having a wavelength of about 8 space units. Note the parallel striping that turns out in the wake of the oblique morphology.  $v = 1$ ,  $A = 0.178$  ( $c_f = 0$ ),  $t = 500$ .

large unstable domain between the front and the region where phase separation occurs, and the scenario will essentially be the same as the phase separation in a field with a homogeneous concentration in the unstable regime.

At front speeds below  $v \approx 2$ , stripes parallel to the front are formed. This pattern is referred to as a lamellar morphology. In the vicinity of the limit velocity, the stripes are staggered and coarse, but below  $v \approx 1$ , they become smooth and straight. Regular lamellar morphology appears at much lower front speeds as well, but the wavelength of the stripes is increased. This effect is reminiscent of the results encountered in modeling the Liesegang phenomenon by the terms of a spinodal phase separation, namely the growing wavelength of the stripes in the wake of a source front with decreasing speed [152]. Note that the character of the patterns does not change when  $c_f = \pm 0.12$ .

b.) In order to examine the stability of the lamellar morphology, the simulations have been performed such that randomly distributed spots with  $c(x, y, 0) = 0$  were introduced in the  $x \in (5, 30)$  space units region of the simulation area. Despite the above random initial conditions, which disturb the first stripes that build up in the wake of the front, lamellar morphology, or oblique morphology, with a small angle, appears at  $v \in (0.5, 2)$ . At  $v > 5$  irregular morphology, and at  $v \approx 0.1$  spotty irregular morphology appears in a 250x620 simulation area. The tendency to form the lamellar morphology slightly diminishes when  $c_f = -0.12$ .

c.) In certain parameter regions, the form and orientation of the preceding stripes will strongly influence the location of the subsequent stripes. Since the growth of a stripe depletes its surrounding, the source front will recover in concentration necessary for the emergence of a new stripe only above a certain distance from the old one. In order to simulate this scenario, in the  $x \in (5, 30)$  space units region of the simulation area a regular structure of tilted stripes with  $c(x, y, 0) = 0$  were introduced. The angle between the edge of the simulation area (the  $Y$ -axis) and the stripes was about 30 degrees, and the wavelength of the structure was about 8 space units. When the front sweeps through this "pre-patterned" region, its contribution will accumulate on the stripes with the unstable concentration  $c = 0$ , leading to a fast phase separation. In this way, a stable striped structure, oblique to the front, will develop. However, an oblique striped structure survives only around  $v \approx 1$ . At  $v \approx 2$ , slightly disturbed lamellar morphology formed. When  $v > 5$  and  $v < 0.1$ , irregular morphology and spotty irregular morphology emerged in a 250x620 simulation area. No significant change was observed when  $c_f = \pm 0.12$ .

### 5.5.3 Rotating source fronts

The oblique morphology in the  $NaOH + CuCl_2$  reactions in PVA gel sheets usually appears when the traveling reaction-diffusion front changes its direction, while the newly forming stripes keep the orientation of previous stripes. This process was computationally modeled by a rotating source front segment in a simulation area of 1200x600 space units, having a length of 570 space units. The initial concentration in the whole simulation area was set to  $c_0(x, y, 0) = -1 + \eta$ . The source term added to the Cahn-Hilliard

equation takes the form

$$S(x, y, t; \omega) = A\sqrt{(x - x_0)^2 + (y - y_0)^2} \exp \left\{ -\alpha [(x - x_0)\sin(\omega t + \theta_0) + (y - y_0)\cos(\omega t + \theta_0)]^2 \right\} \quad (5.3)$$

The character of the pattern formation is a function of the front speed, that depends on the angular velocity, as well as the position along the radius. In our simulations, having a front length of 570 space units, striped patterns just behind the front appeared around the angular velocity interval  $\omega \in (0.002 - 0.02)$ . The dynamics of the pattern formation was as follows: The first stripe forms roughly along the initial position of the front. Although the orientation of the front is continuously altered, the newly formed stripes will “try” to form along the old ones, parallel with them. Since the front changes its orientation in the meanwhile, the above scenario will lead to an oblique morphology.

However, the simulations showed that the stripes cannot grow perpendicular to the front (fig. 5.8). Their elongation becomes unstable when the angle of the stripes formed to the front supplying the phase separating material reaches about 70 – 90 degrees. At this stage, in some domains just behind the front oblique stripes with a small angle appear. In some other domains irregular morphology appears. Later, the above scenario may repeat itself.

Note that in the vicinity of the outer endpoint of the rotating front, where the speed is relatively high, the source front may not immediately be followed by the phase separation. The outer core of the circular region may be patterned by a different mechanism, namely the striping initiated by the arc-like edge where the concentration changes from  $c = 0$  to  $c = -1$ . This striping will start along the edge, and will spread inside the unstable region, until it meets the straight striping initiated by the front itself.

Finally we review the pattern formation at much higher and lower angular velocities. When the angular velocity is higher than  $\omega = 0.05$ , the overwhelming majority of the phase separation takes place far behind the front. Two mechanisms play an important role in the pattern formation. As mentioned previously, a striping will be initiated by the arc-like edge, where the concentration changes from  $c = 0$  to  $c = -1$ . However, in the inner regions, mostly irregular patterns will form. In the case of low angular velocities, when  $\omega < 0.001$ , spotty irregular morphology appears in the wake of the front with a length of 570 space units.

#### 5.5.4 Studies on Quenching Fronts

An alternative way to start the spinodal decomposition in the wake of a traveling front is to set the concentration of the phase separating compound  $c$  in between the spinodal points, while the temperature is dropped below the critical value only behind the front. The quenching in our simulations has been realized by changing the sign of the second-order term in the Cahn-Hilliard equation.

Pattern formation in the wake of quenching fronts has been studied by computational analyzes similar to those performed in the case of source fronts. The main difference

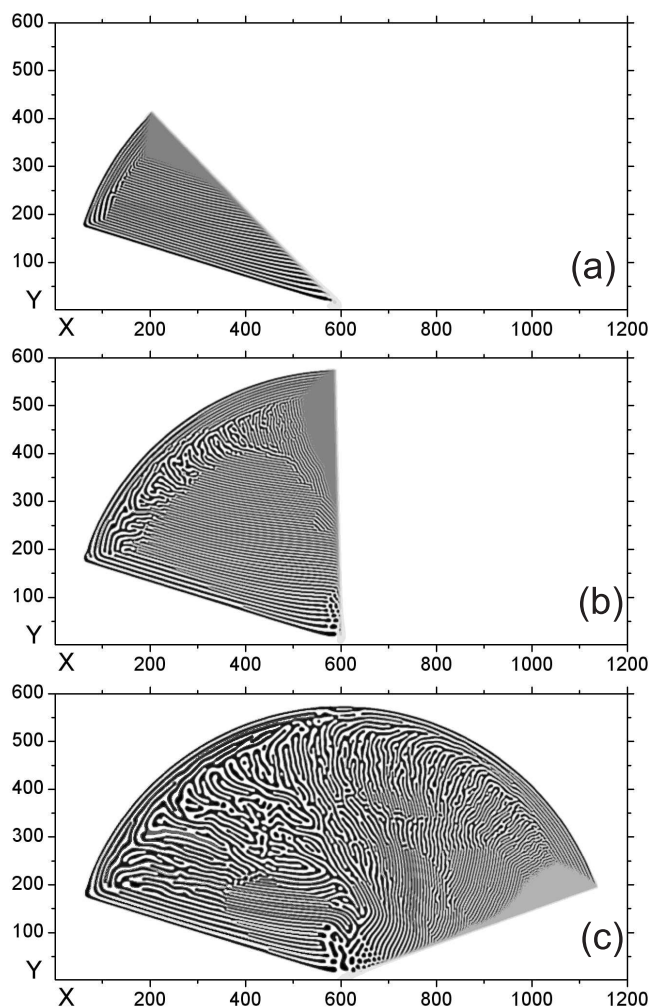


Figure 5.8: Pattern formation in the wake of rotating source fronts. The angular velocity is  $\omega = 0.005$ , the dimensions of the simulation area are  $1200 \times 600$  space units. The parameter  $\theta_0 = 0.3$  was introduced to prevent the first stripes being parallel to one of the grid lines.  $\epsilon = 0.5$ ,  $x_0 = 600$ ,  $y_0 = 5$ ,  $A = 0.00089$ ,  $\alpha = 0.1$  ( $c_f = 1$ ),  $c_0 = -1 + \eta$ . Attention should be paid to the regions just behind the wake of the fronts; after this, coarsening will restructure the patterns. (a.) Oblique striping at  $t = 100$ . (b.) The critical angle is reached, the growth of the stripes becomes unstable.  $t = 250$ . (c.) Oblique morphology with a new angle builds up in the wake of the front.  $t = 500$ .

with respect to the pattern formation in the wake of the source fronts is the appearance of the columnar morphology at low front speeds, in agreement with Furukawa's results [199]. With the concentration of the phase separating compound set to  $c_0(x, y, 0) = 0$ , the columnar morphology appears below  $v \approx 0.85$ . At  $v \approx 0.9 - 2$ , more or less coarse lamellar morphology forms. Above  $v \approx 10$  irregular morphology appears. When  $c_0(x, y, 0) = \pm 0.1$ , this limit where the columnar morphology appears, shifts toward lower velocities.

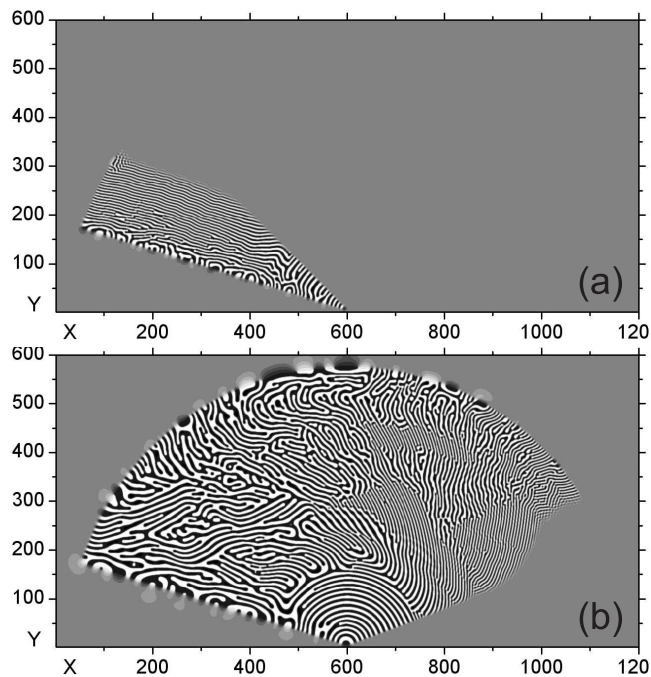


Figure 5.9: Pattern formation in the wake of a rotating quenching front. The dimensions of the simulation area are 600x1200 space units. The parameter  $\theta_0 = 0.3$  was introduced to prevent the stripes being parallel to the grid lines.  $\omega = 0.005$ ,  $\epsilon = 0.5$ ,  $x_0 = 600$ ,  $y_0 = 5$ ,  $c_0 = 0$ ;  $t = 100$  (a.) and  $t = 500$  (b.). Note the continuous arc-shaped stripes in the vicinity of the rotation center, where the local velocity is small. The growing endpoints of these stripes are always perpendicular to the radial quenching front. Attention should be paid to the regions just behind the front; after this, coarsening will restructure the patterns, except for the arcs “pulled” by the front.

The formation of oblique morphologies has also been observed. The most extensive OM-s appeared around the velocity  $v \approx 1$ , when oblique stripes with  $c(x, y, 0) = 0.2$  and geometric parameters as above were initially introduced in the  $x \in (5, 30)$  space units region of the simulation area.

The most interesting characteristics of the pattern formation in a growing quenched area was found in the computational investigation of rotating fronts. Moving outwards along the radius, that is, reaching front segments with higher velocities, bent columnar structures, oblique patterns forming different angles to the front, and, near the border of the quenched region, lamellar morphologies have been observed.

It is remarkable that the growing ends of the bent stripes always remain perpendicular to the rotating radial front (fig. 5.9). As a consequence, in the case of a front rotating with an appropriate speed, bent columnar structures build up, which develop into regular arcs. This result can be of major importance in various nanotechnological processes, since it makes possible the “wiring” of a surface upon a previously given curve. By moving a quenching front, having an appropriate speed, along an arbitrary



non-intersecting path, a columnar structure of high and low density regions builds up behind it.

## 5.6 Conclusions

The most important new property of the experimental systems presented here is their ability to yield regular patterns, even under  $20\ \mu m$ , despite the simplicity of the reagents. A promising application of the gels containing periodic sheets of precipitate would be in the manufacture of optical gratings [203, 204]. Gratings prepared by the sectioning of gel columns that contain equidistant sheets of precipitate have been tested experimentally. Another possibility is an alternative method of production for layered materials or composite structures [205].

The scenario of the pattern formation was modeled by the terms of phase separation described by the Cahn-Hilliard Equation. The formation of the stripes, being parallel or oblique to the reaction-diffusion front, has been reproduced by computer simulations. Other classes of models, based on reaction-diffusion equations, also reproducing the main features of the formation of stripes of precipitates, have been studied by computer simulations [160]. Thus, further experiments are required in order to find out the real pattern forming mechanism. Note, that the substrate which is assumed in the model presented above is probably not the DC proposed in the explanation of the primary patterns, since the formation of stripes of colloidal precipitate does not seem to affect the dynamics and shape of the active border.

The results have been compared to the pattern formation in the case of directional quenching. At low front velocities, the formation of striped patterns perpendicular to the quenching front have been observed, these patterns being absent in the case of the source fronts. In the wake of a slowly progressing front that simultaneously changes its direction, the growing endpoints of the stripes will always be perpendicular to the front. This effect enables one to “draw” on a surface regular stripes following an arbitrary curve. Such a patterning could be of major importance in nanotechnology.



# Chapter 6

## Afterword

### 6.1 Publications

The following papers have been published in internationally refereed scientific journals:

1. Péter Hantz, *Pattern Formation in the NaOH + CuCl<sub>2</sub> Reaction* J. Phys. Chem. B **104**, 4266 (2000)
2. Péter Hantz, *Regular Microscopic Patterns produced by simple reaction-diffusion systems* Phys. Chem. Chem. Phys. **4**, 1262 (2002)
3. Péter Hantz, *Germinating Surfaces in Reaction-Diffusion systems? Experiments and a hypothesis* J. Chem. Phys. **117**, 6646 (2002)
4. Benjamin de Lacy Costello, Péter Hantz and Norman Ratcliffe, *Voronoi Diagrams Generated by Regressing Edges of Precipitation Fronts* J. Chem. Phys. **120**, 2413-2416 (2004)
5. Péter Hantz, Julian Partridge, Győző Láng, Szabolcs Horvát and Mária Ujvári, *Ion-Selective Membranes Involved in Pattern-Forming Processes*, J. Phys. Chem. B. **108**, 18135-18139 (2004)
6. Szabolcs Horvát and Péter Hantz, *Pattern Formation Induced by Ion-selective Surfaces: Models and Simulations*, J. Chem. Phys. **121**, 034707 (2005)
7. Péter Hantz and István Biró, *Phase Separation in the Wake of Moving Fronts: Experiments and Simulations*, Phys. Rev. Letters **96**, 088305 (2006)

### 6.2 Perspectives for Further Research

The elucidation of the reaction mechanism makes necessary further experimental and theoretical investigations. Of central importance seems to be the study of the passive border and the origin of its ion-selective properties. Performing some detailed chemical analyses should also be relevant. In possession of new experimental data, better mathematical models and computer simulations should be performed.

Regarding the secondary patterns, exploring the mechanism of the formation of the colloidal precipitate would be the most important. If the wavelength of the secondary

patterns could be decreased, several technological applications may follow.

# Bibliography

- [1] M. C. Cross and P. C. Hohenberg, *Pattern Formation Outside of Equilibrium*, Rev. Mod. Phys. **65**, 851-1112 (1993)
- [2] Daniel Walgraef, *Spatio-Temporal Pattern Formation*, Springer, New York (1997)
- [3] P. E. Cladis and P. Palffy-Muhoray, *Spatio-Temporal Patterns in Nonequilibrium Complex Systems*, Proceedings Volume XXI, Santa Fe Institute, Addison-Vesely, Reading (1995)
- [4] Yukio Saito, *Statistical Physics of Crystal Growth*, World Scientific, Singapore (1996)
- [5] A. S. Mikhailov, *Foundations of Synergetics*, Springer, Berlin (1990)
- [6] Marco Raymond Rijnders, *Periodic Layer Formation During Solid State Reactions*, PhD Thesis, Eindhoven University of Technology, the Netherlands (1996)
- [7] Irving R. Epstein and John A. Pojman, *An Introduction to Nonlinear Chemical Dynamics*, Oxford University Press, New York (1998)
- [8] Póta György, *Kémiai hullámok és térbeli szerkezetek reakció-diffúzió rendszerekben*, Kossuth Egyetemi Kiadó, Debrecen (1996)
- [9] Peter Gray and Stephen K. Scott, *Chemical Oscillations and Instabilities*, Oxford University Press, Oxford (1994)
- [10] Richard J. Field and Mária Burger, *Oscillations and Traveling Waves in Chemical Systems*, Wiley, New York (1985)
- [11] Friedmann W. Schneider, *Nichtlineare Dynamik in der Chemie*, Spektrum Akademischer Verlag, Heidelberg (1996)
- [12] Bazsa György, *Nemlineáris dinamika és egzotikus kinetikai jelenségek kémiai rendszerekben*, Egyetemi jegyzet-KLTE, Debrecen-Budapest-Gödöllő (1992)
- [13] Hantz Péter, *Mintázatképződés reakció-diffúzió rendszerekben*, Diploma Thesis, Eötvös Loránd University, Budapest, Hungary (1998)

- 
- [14] Lewis Wolpert, *Principles of Development*, Oxford University Press, Oxford (2002)
- [15] James D. Murray, *Mathematical Biology*, Springer, Berlin (1993)
- [16] Miklós Farkas, *Dynamical Models in Biology*, Academic Press, London (2001)
- [17] A. J. Koch and H. Meinhardt, *Biological pattern formation: from basic mechanisms to complex structures*, Rev. Mod. Phys. **66**, 1481-1507 (1994)
- [18] Sass Miklós, *Fejlődéstan*, Eötvös kiadó, Budapest (1995)
- [19] Peter Grindrod, *The Theory and Applications of Reaction-diffusion Equations. Patterns and Waves*, Clarendon Press, Oxford (1996)
- [20] Paul C. Fife, *Mathematical Aspects of Reacting and Diffusing Systems*, Lecture Notes in Biomathematics **28**, Springer, Berlin (1979)
- [21] Mads Ipsen, Lorenz Kramer and Preben Graae Sorensen, *Amplitude equations for description of chemical reaction-diffusion systems*, Physics Reports **337**, 193-235 (2000)
- [22] Stephen Wolfram, *Cellular automata as models of complexity*, Nature **311**, 419-242 (1994)
- [23] N. F. Britton, *Reaction-Diffusion Equations and Their Applications to Biology*, Academic Press, London (1986)
- [24] John J. Tyson and Paul C. Fife, *Target patterns in a realistic model of the Belousov-Zhabotinskii reaction*, J. Chem. Phys. **73**, 2224-2237 (1980)
- [25] John J. Tyson and James P. Keener, *Singular perturbation theory of traveling waves in excitable media (a review)*, Physica D **32**, 327-361 (1988)
- [26] G. Nicolis, *Introduction to Nonlinear Science*, Cambridge University Press, Cambridge (1995)
- [27] Lingfa Yang and Irving R. Epstein, *Chemical Wave Packet Propagation, Reflection, and Spreading*, J. Phys. Chem. A **106**, 11676-11682 (2002)
- [28] Razvan A. Satnoianu, Michael Menzinger and Philip K. Maini, *Turing instabilities in General Systems*, J. Math. Biol. **41**, 493-512 (2000)
- [29] A. M. Turing, *The Chemical Basis of Morphogenesis*, Phil. Trans. Roy. Soc. Lond. **237**, 37-72 (1952)
- [30] Vladimir K. Vanag and Irving R. Epstein, *Packet Waves in a Reaction-Diffusion system*, Phys. Rev. Lett. **88**, 088303 1-4 (2002)

- [31] Vladimir K. Vanag and Irving R. Epstein, *Comparative Analysis of Packet and Trigger Waves Originating from a Finite Wavelength Instability*, J. Phys. Chem. A **106**, 11394-11399 (2002)
- [32] Orbán Miklós, *Oscilláló kémiai reakciók: véletlen felfedezéstől a tervezésig*, Lom-bik és reaktor 1996/2, 37-41 (1996)
- [33] Stephen K. Scott, *Oscillations, waves and chaos in chemical kinetics*, Oxford Uni-versity Press, Oxford (1994)
- [34] Orbán Miklós, *Kémiai periodicitás időben és térben*, Kémiai Közlemények **105**, 109-121 (1999)
- [35] L. Hegedűs, M. Wittmann, Z. Noszticziusz, S. Yan, A. Sirimugkala, H.-D. Försterling and R. J. Field, *HPLC analysis of complete BZ systems. Evolution of the chemical composition in cerium and ferroin catalysed batch oscillators: ex-periments and model calculations*, Faraday Discuss. **120**, 21-38 (2002)
- [36] Richard M. Noyes, Richard J. Field and Endre Körös, *Oscillations in Chemical Systems I. Detailed Mechanism in a System Showing Temporal Oscillations*, J. Am. Chem. Soc. **94**, 1394-1395 (1972)
- [37] Vilmos Gáspár and Kenneth Showalter, *Period lengthening and associated bifur-cations in a two-variable, flow Oregonator*, J. Chem. Phys. **88**, 778-791 (1988)
- [38] Gáspár Vilmos, *Nemlineáris kémiai dinamika*,  
<http://www.kfki.hu/chemonet/hun/eloado/gaspar/kemdin.html>
- [39] L. Györgyi, T. Turányi and R. J. Field, *Analysis and simplification of the GTF model of the Belousov-Zhabotinsky reaction*, J. Phys. Chem. **97**, 1931-1941 (1993)
- [40] [http://osiris.sunderland.ac.uk/~cs0dcu/Dynamical\\_Systems/](http://osiris.sunderland.ac.uk/~cs0dcu/Dynamical_Systems/)
- [41] Zoltán Noszticziusz, Mária Wittmann and Peter Stirling, *Bifurcation from ex-citability to limit cycle oscillations at the end of the induction period in the clas-sical Belousov-Zhabotinsky reaction*, J. Chem. Phys. **86**, 1922-1926 (1987)
- [42] M. Hazewinkel (editor), *Encyclopaedia of Mathematics*, Kluwer, Dordrecht (1995-1997)
- [43] Richard A. B. Bond, Bice S. Martincigh, Janusz R. Mika and Reuben H. Simoyi, *The Quasi-Steady-State Approximation: Numerical Validation*, J. Chem. Educ. **75**, 1158-1165 (1998)
- [44] Mads Kaern, *Biochemical Reaction Systems*, PhD Thesis, University of Copen-hagen (1997) [http://theochem.ki.ku.dk/thesis/mads\\_kaern\\_thesis.ps.gz](http://theochem.ki.ku.dk/thesis/mads_kaern_thesis.ps.gz)

- 
- [45] T. Turányi, A. S. Tomlin and M. J. Pilling, *On the Error of the Quasi-Steady-State Approximation*, J. Phys. Chem. **97**, 163-172 (1993)
- [46] Hans Meinhardt, *The Algorithmic Beauty of Sea Shells*, Springer, Berlin (1995)
- [47] Hans Meinhardt and Alfred Gierer, *Pattern formation by local self-activation and lateral inhibition*, BioEssays **22**, 753-760 (2000)
- [48] P. Borockmans, G. Dewel, A. de Wit, E. Dulos, J. Boissonade, F. Gauffre and P. de Kepper, *Diffusive instabilities and chemical reactions*, Int. J. Bifurcations and Chaos **12**, 2307-2332 (2002)
- [49] Shigeru Kondo and Rihito Asai, *A reaction-diffusion wave on the skin of the marine angelfish Pomacanthus*, Nature **376**, 765-768 (1995)
- [50] K. J. Painter, *Models for pigment pattern formation in the skin of fishes*, in: Mathematical Models for Biological Pattern Formation, by: Philip K. Maini and Hans G. Othmer (eds.), Springer, New York, (2001) pp.: 59-81, /The IMA Volumes in Mathematics and its Applications **121**/
- [51] <http://www.livingreefimages.com>
- [52] Eörs Szathmári, *Developmental circuits rewired*, Nature **411**, 143-145 (2001)
- [53] V. Castets, E. Dulos, J. Boissonade and P. De Kepper *Experimental evidence of a sustained standing Turing-type nonequilibrium chemical pattern* Phys. Rev. Lett. **64**, 2953-2956 (1990)
- [54] István Lengyel and Irving R. Epstein, *Modeling of Turing Structures in the Chlorite-Iodide-Malonic Acid-Starch Reaction System*, Science **251**, 650-652 (1991)
- [55] Vladimir K. Vanag and Irving R. Epstein, *Pattern Formation in a Tunable Medium: The Belousov-Zhabotinsky Reaction in an Aerosol OT Microemulsion*, Phys. Rev. Lett. **87**, 228301 1-4 (2001)
- [56] M.L. Krasnov, A.I. Kiselyor, G.I. Makarenko, *A book of problems in ordinary differential equations*, Mir Publisher, Moscow (1981)
- [57] Raymond M. Redheffer, *Differential Equations: Theory and Applications*, Jones and Bartlett Publishers, Boston, MA (1991)
- [58] Anatol M. Zhabotinsky, Milos Dolnik, and Irving R. Epstein, *Pattern Formation arising from wave instability in a simple reaction-diffusion system*, J. Chem. Phys. **103**, 10306-10314 (1995)



- [59] P. Blanchedeau, J. Boissonade, P. De Kepper, *Theoretical and experimental studies of spatial bistability in the chlorine-dioxide-iodide reaction*, Physica D **147**, 283-299 (2000)
- [60] Janet Webb, *Bilateral extinction?*, Mycologist **4**, 40 (1990)
- [61] F.A. Davidson, B.D. Rayner, A.D.M. Crawford, K. Ritz, *Travelling waves and pattern formation in a model for fungal development*, J. Math. Biol. **35**, 589-608 (1997)
- [62] John Ross, Stefan C. Müller, Christian Vidal, *Chemical Waves*, Science **240**, 460-465 (1988)
- [63] Tatsunari Sakurai, Eugene Mihaliuk, Florin Chirila, Kenneth Showalter, *Design and Control of Wave Propagation in Excitable Media*, Science **296**, 2009-2012 (2002)
- [64] Douglas Ridgway, Herbert Levine and Yuhai Tu, *Front stability in mean-field models of diffusion-limited growth*, Phys. Rev. E **53**, 861-870 (1996)
- [65] Ute Herbert and Wim van Saarloos, *Breakdown of the standard perturbation theory and moving boundary approximation for "pulled" fronts*, Phys. Rep. **337**, 139-156 (2000)
- [66] Thomas A. Gribschaw, Kenneth Showalter, Debra L. Banville, and Irving R. Epstein, *Chemical Waves in the Acidic Iodate Oxidation of Arsenite*, J. Phys. Chem. **85**, 2152-2155 (1981)
- [67] K. Showalter and J.J. Tyson, *Luther's 1906 discovery and analysis of chemical waves*, J. Chem. Educ. **64**, 742-744 (1987)
- [68] P. A. Epik and N. S. Shub, *Frontalnoe Tetsenie Reaktii Okislenia Arsenita Iodatom*, Dokladi Akademii Nauk SSSR **100**, 503-506 (1955)
- [69] Dezső Horváth, Valery Petrov, Stephen K. Scott, Kenneth Showalter, *Instabilities in propagating reaction-diffusion fronts*, J. Chem. Phys. **98**, 6332-6343 (1993)
- [70] Pavel K. Brazhnik and John J. Tyson, *On traveling wave solutions of Fisher's equation in two spatial dimensions*, SIAM J. Appl. Math. **60**, 371-391 (1999)
- [71] Ronald Imbihl and Gerhard Ertl, *Oscillatory Kinetics in Heterogeneous Catalysis*, Chem. Rev. **95**, 697-733 (1995)
- [72] K. Krischer, M. Eiswirth, and G. Ertl, *Oscillatory CO oxidation on Pt(110): Modeling of temporal self-organization*, J. Chem. Phys. **96**, 9161-9172 (1992)

- [73] M. Bär, Ch. Zülicke, M. Eiswirth, and G. Ertl, *Theoretical modeling of spatiotemporal self-organization in a surface catalyzed reaction exhibiting bistable kinetics*, J. Chem. Phys. **96**, 8595-8604 (1992)
- [74] M. Falcke, M. Bär, H. Engel, and M. Eiswirth, *Traveling waves in the CO oxidation on Pt(110): Theory*, J. Chem. Phys. **97**, 4555-4563 (1992)
- [75] Alexander von Oertzen, Alexander S. Mikhailov, Harm H. Rotermund, and Gerhard Ertl, *Subsurface Oxygen in the CO Oxidation Reaction on Pt(100): Experiments and Modeling Pattern Formation*, J. Phys. Chem. B **102**, 4966-4981 (1998)
- [76] Janpeter Wolff, Athanasios G. Papathanasiou, Ioannis G. Kerkvedis, Harm Heinrich Rotermund, G. Ertl, *Spatiotemporal Addressing of Surface Activity*, Science **294**, 134-137 (2001)
- [77] Katharina Krischer, *Spontaneous formation of spatiotemporal patterns at the electrode/electrolyte interface*, J. Electroanal. Chem. **501**, 1-21 (2001)
- [78] Katharina Krischer, Nadia Mazouz, and Peter Grauel, *Fronts, Waves, and Stationary Patterns in Electrochemical Systems*, Angew. Chem. Int. Ed. **40**, 850-869 (2001)
- [79] K. Agladze and O. Steinbock, *Waves and Vortices of Rust on the Surface of Corroding Steel*, J. Phys. Chem. A **104**, 9816-9819 (2000)
- [80] Ralph D. Otterstedt, Peter J. Plath, Nils I. Jaeger and John L. Hudson, *Rotating waves on disk and ring electrodes*, J. Chem.Soc. Faraday Trans. **92**, 2933-2939 (1996)
- [81] Anette F. Taylor, Vilmos Gáspár, Barry R. Johnson and Stephen K. Scott, *Analysis of Reaction-Diffusion Waves in the Ferrocene-Catalysed Belousov-Zhabotinsky Reaction*, Phys. Chem. Chem. Phys. **1**, 4595-4599 (1999)
- [82] Jean-Marc Flesselles, Andrew Belmonte and Vilmos Gáspár, *Dispersion relation for waves in the Belousov-Zhabotinsky reaction*, Phys. Chem. Chem. Phys. **94**, 851-855 (1998)
- [83] Ágota Tóth, Vilmos Gáspár, and Kenneth Showalter, *Signal Transduction in Chemical Systems: Propagation of Chemical Waves through Capillary Tubes*, J. Phys. Chem. **98**, 522-531 (1994)
- [84] <http://chemweb.chem.fsu.edu/editors/STEINBOCK/projects/chdbz/chdbz.htm>
- [85] J. M. Bodet and J. Ross, *Experiments on phase diffusion waves*, J. Chem. Phys. **86**, 4418-4424 (1987)

- 
- [86] Anna L. Lin, Matthias Bertram, Karl Martinez, and Harry L. Swinney, *Resonant Phase Patterns in a Reaction-Diffusion System*, Phys. Rev. Lett. **84**, 4240-4243 (2000)
- [87] Alberto Pimpinelli and Jaques Villain, *Physics of Crystal Growth*, Cambridge University Press, Cambridge (1998)
- [88] Jürg Hulliger, *Chemistry and Crystal Growth*, Angew. Chem. Int. Ed. Engl. **33**, 143-162 (1994)
- [89] M. E. Glicksman and S. P. Marsh *The Dendrite*, in: Handbook of Crystal Growth, vol. 1, by D. T. J. Hurle (editor), North-Holland, Amsterdam (1993), pp. 1075-1121
- [90] James S. Langer, *Issues and Opportunities in Materials Research*, Physics Today **45**, 24-31 (1992)
- [91] V. Fleury, J.-F. Gouyet, M. Leonetti (editors), *Branching in Nature*, Springer, Berlin (2001)
- [92] <http://www.its.caltech.edu/~atomic/snowcrystals/>
- [93] Kenneth G. Libbrecht, *Morphogenesis on Ice: The Physics of Snow Crystals*, [http://pr.caltech.edu/periodicals/EandS/archives/LXIV\\_1.html](http://pr.caltech.edu/periodicals/EandS/archives/LXIV_1.html)
- [94] Makoto Ohara and Robert C. Reid, *Modeling crystal growth rates from solution*, Prentice-Hall, Englewood Cliffs, New Jersey, (1973)
- [95] Xiang-Yang Liu and P. Bennema, *Morphology of crystals: Internal and external controlling factors*, Phys. Rev. B **49**, 765-775 (1994)
- [96] Xiang-Yang Liu and P. Bennema, *Theoretical consideration of growth morphology of crystals*, Phys. Rev. B **53**, 2314-2325 (1996)
- [97] E. van Veenendaal, P. J. C. M. van Hoof, J. van Suchtelen, W. J. P. van Enckevort, P. Bennema, *Kinetic roughening of the Kossel (100) surface: comparison of classical criteria with Monte Carlo results*, Surf. Sci. **417**, 121-138 (1998)
- [98] Xiang-Yang Liu, P. Bennema and J. P. van der Eerden, *Rough-flat-rough transition of crystal surfaces*, Nature **356**, 778-782 (1992)
- [99] <http://www.dur.ac.uk/sharon.cooper/lectures/cryskinetics/handoutsallb.html>
- [100] E. A. Brener and V. I. Melnikov, *2-Dimensional dendritic growth at arbitrary Peclet number*, Adv. Phys. **40**, 53-97
- [101] J. S. Langer, *Dendrites, Viscous Fingers, and the Theory of Pattern Formation*, Science **243**, 1150-1156 (1989)

- 
- [102] T. Ihle, *Competition between kinetic and surface tension anisotropy in dendritic growth*, Eur. Phys. J. B **16**, 337-344 (2000)
- [103] W. J. Boettinger, S. R. Coriell, A. L. Greer, A. Karma, W. Kurz, M. Rappaz and R. Trivedi, *Solidification Microstructures: Recent Developments, Future Directions*, Acta Mater. **48**, 43-70 (2000)
- [104] T. Ihle and H. Müller-Krumbhaar, *Fractal and compact growth morphologies in phase transitions with diffusive transport*, Phys. Rev. E **49**, 2972-2991 (1994)
- [105] E. Brener, H. Müller-Krumbhaar, and D. Temkin, *Structure formation and the morphology diagram of possible structures in two-dimensional diffusional growth*, Phys. Rev. E **54**, 2714-2722 (1996)
- [106] Silvére Akamatsu, Gabriel Faivre and Thomas Ihle, *Symmetry-broken double-fingers and seaweed patterns in thin-film directional solidification of a nonfaceted cubic crystal*, Phys. Rev. E **51**, 4751-4773 (1995)
- [107] Andrew Harrison, *Fractals in Chemistry*, Oxford University Press, Oxford (1995)
- [108] Y. Couder, F. Argoul, A. Arnédo, J. Maurer and M. Rabaud, *Statistical properties of fractal dendrites and anisotropic diffusion-limited aggregates*, Phys. Rev. A **42**, 3499-3503 (1990)
- [109] U. Bisang and J. H. Bilgram, *Shape of the tip and the formation of sidebranches of Xenon dendrites*, Phys. Rev. E **54**, 5309-5326 (1996)
- [110] Henry Chou and Herman Z. Cummins, *Evolution of Dendritic Instability in Solidifying Succinonitrile*, Phys. Rev. Lett. **61**, 173-176 (1988)
- [111] T. Ihle and H. Müller-Krumbhaar, *Discontinuous transition between seaweed and chaotic growth morphology* J. Phys. I **6**, 949-967 (1996)
- [112] Tamás Vicsek, *Fractal Growth Phenomena*, World Scientific, Singapore (1992)
- [113] David Avnir (editor), *The Fractal Approach to Heterogeneous Chemistry: Surfaces, Colloids, Polymers*, Wiley, Chichester (1989)
- [114] Vincent Fleury, *Branching morphogenesis in a reaction-diffusion model*, Phys. Rev. E **61**, 4156-4160 (2000)
- [115] Thomas C. Halsey, *Diffusion-Limited Aggregation: A Model for Pattern Formation*, Physics Today **53**, 36-41 (2000)
- [116] Tamás Vicsek, *Pattern-Formation in Diffusion-Limited Aggregation*, Phys. Rev. Lett. **53**, 2281-2284 (1984)

- [117] R. Ed. Liesegang, *Ueber einige Eigenschaften von Gallerten*, Naturwissenschaftliche Wochenschrift, **XI**, 353-362 (1896)
- [118] T. Antal, M. Droz, J. Magnin, Z. Rácz and M. Zrínyi, *Derivation of the Matalon-Packter law for Liesegang patterns*, J. Chem. Phys. **109**, 9479-9486 (1998)
- [119] Heinz K. Henish, *Crystals in Gels and Liesegang Rings*, Cambridge University Press, Cambridge (1988)
- [120] M. Fialkowski, A. Bitner and B.A. Grzybowski, *Wave Optics of Liesegang Rings*, Phys. Rev. Lett. **94**, 018303 (2005)
- [121] I.T. Bensemam, M. Fialkowski and B.A. Grzybowski, *Wet stamping of microscale periodic precipitation patterns* J. Phys. Chem. B **109**, 2774-2778 (2005)
- [122] F. Lefauchaux and M. C. Robert, *Crystal Growth in Gels*, in: Handbook of Crystal Growth, vol. 2, by: D. T. J. Hurle, North-Holland, Amsterdam (1993), pp.: 1271-1303
- [123] N. Kanniah, F. D. Gnanam, P. Ramasamy and G. S. Laddha, *Revert and Direct Type Liesegang Phenomenon of Silver Iodide*, J. Coll. and Int. Sci. **80**, 369-375 (1980)
- [124] Prem Mathur and Satyeshwar Ghosh, *Liesegang Rings - Part I. Revert Systems of Liesegang Rings*, Kolloid-Z. **159**, 143-146 (1957)
- [125] Harold S. Davis, *The Rhythmic Precipitation of Colloidal Mercury*, The Journal of the American Chemical Society **39**, 1312-1314 (1917)
- [126] Wilhelm Ostwald, *Lehrbuch der Allgemeinen Chemie II/2*, W. Engelmann, Leipzig (1896-1902)
- [127] C. Wagner, *Mathematical Analysis of the Formation of Periodic Precipitates*, J. Colloid Sci. **5**, 85-97 (1950)
- [128] S. Prager, *Periodic Precipitation*, J. Chem. Phys. **25**, 279-283 (1956)
- [129] R. Matalon and A. Packter, *The Liesegang Phenomenon. I. Sol Protection and Diffusion*, J. Colloid Sci. **10**, 46-61 (1955)
- [130] A. Packter *The Liesegang Phenomenon. IV. Reprecipitation from ammonia peptised sols*, Kolloid-Zeitschrift **142**, 109-117 (1955)
- [131] M. C. K. Jablinczki: *La formation rythmique des précipités. Les anneaux Liesegang*, Bulletin de la Societé Chimique de France, **33**, 4<sup>e</sup> série, 1592-1603 (1923)

- [132] Harry W. Morse and George W. Pierce: *Diffusion and Supersaturation in Gelatine* Proceedings of the American Academy of Arts and Sciences **38**, 625-647 (1903)
- [133] M. Droz, J. Magnin and M. Zrínyi, *Liesegang patterns: Studies on the width law*, J. Chem. Phys. **110**, 9618-9622 (1999)
- [134] B. Chopard, P. Luthi and M. Droz, *Reaction-Diffusion Cellular Automata Model for the Formation of Liesegang Patterns*, Phys. Rev. Lett. **72**, 1384-1387 (1994)
- [135] E. Hatschek, *Zur Theorie der Liesegang'schen Schichtungen*, Zeitschrift für Chemie und Industrie der Kolloide (Kolloid-Zeitschrift) **10**, 124-126 (1912)
- [136] D. N. Gosh, *Studies on Phythmic Formations*, Journal of the Indian Chemical Society **7**, 509-513 (1930)
- [137] M. E. LeVan and J. Ross, *Measurements and Hypothesis on Perioic Precipitation Processes*, J. Phys. Chem. **91**, 6300-6308 (1987)
- [138] G. T. Dee, *Patterns Produced by Precipitation at a Moving Reaction Front*, Phys. Rev. Lett. **57**, 275-278 (1986)
- [139] A. Büki, É. Kárpáti-Smidróczki, and M. Zrínyi, *Computer simulation of regular Liesegang structures*, J. Chem. Phys. **103**, 10387-10392 (1995)
- [140] Büki András, *A Liesegang jelenség lehetséges mechanizmusainak vizsgálata számítógépes szimulációval*, PhD Thesis, Technical University of Budapest, Hungary (1994)
- [141] Stefan C. Müller, Shoichi Kai and John Ross, *Periodic Precipitation Patterns in the Presence of Concentration Gradients 1.*, J. Phys. Chem. **86**, 4078-4087 (1982)
- [142] L. Gálfi and Z. Rácz, *Properties of the reaction front in an  $A + B \rightarrow C$  type reaction-diffusion process*, Phys. Rev. A **38**, 3151-3154 (1988)
- [143] Jérôme Magnin, *Pattern Formation in Reaction-Diffusion Systems: the Liesegang Structures*, PhD Thesis, Université de Genève, Genève, Suisse (2000)
- [144] Ernest S. Hedges and Rosalind V. Henley, *The Formation of Liesegang Rings as a Periodic Coagulation Phenomenon*, Journal of the Chemical Society **1928/II**, 2714-2727 (1928)
- [145] Michael Flicker and John Ross, *Mechanism of chemical instability for periodic precipitation phenomena*, J. Chem. Phys. **60**, 3458-3465 (1974)
- [146] N. R. Dhar and A. C. Chatterji: *Theorien der Liesegangringbildung*, Kolloid-Zeitschrift **37**, 2-9 (1925)

- [147] N. R. Dhar and A. C. Chatterji: *Studies on the Formation of Periodic Precipitates*, The Journal of Physical Chemistry, **28**, 41-50 (1924)
- [148] Hiroshige Higuchi and Ryohei Matura, *The Concentration Distribution in the Gel before the Periodic Precipitation*, Memoirs of the Faculty of Science, Kyushu University, Series C Chemistry, **5**, 33-42 (1962)
- [149] Vladislav Holba and Frederic Fusek, *Gravity Effect on the Formation of Periodic Precipitation Patterns*, Collect. Czeh. Chem. Commun. **65**, 1438-1442 (2000)
- [150] L. Gránásy, *Nucleation and Spinodal Decomposition*, Solid State Phenomena **56**, 67-106 (1997)
- [151] C. Domb and J. L. Lebowitz (editors), *Phase Transitions and Critical Phenomena*, vol. 8, Academic Press, London (1989)
- [152] T. Antal, M. Droz, J. Magnin, and Z. Rácz, *Formation of Liesegang Patterns: A Spinodal Decomposition Scenario*, Phys. Rev. Lett. **83**, 2880-2883 (1999)
- [153] Zoltán Rácz, *Formation of Liesegang Patterns*, Physica A **274**, 50-59 (1999)
- [154] T. Antal, M. Droz, J. Magnin, A. Pekalski, and Z. Rácz, *Formation of Liesegang Patterns: Simulations using a kinetic Ising model*, J. Chem. Phys. **114**, 3370-3375 (2001)
- [155] B. Ermentrout, J. Campbell, G. Oster, *A model for shell patterns based on neural activity*, The Veliger **28**, 369-388 (1986)
- [156] Hans Meinhardt and Martin Klinger, *A model for pattern generation on the shells of molluscs*, J. Theor. Biol. **126**, 63-89 (1987)
- [157] Péter Hantz, *Pattern Formation in the NaOH + CuCl<sub>2</sub> Reaction*, J. Phys. Chem. B **104**, 4266-4272 (2000)
- [158] Péter Hantz, *Germinating surfaces in reaction-diffusion systems? Experiments and a hypothesis*, J. Chem. Phys. **117**, 6646-6654 (2002)
- [159] Benjamin de Lacy Costello, Péter Hantz and Norman Ratcliffe, *Voronoi Diagrams Generated by Regressing Edges of Precipitation Fronts* J. Chem. Phys. **120**, 2413-2416 (2004)
- [160] Péter Hantz, *Regular microscopic patterns produced by simple reaction-diffusion systems*, Phys. Chem. Chem. Phys. **4**, 1262-1267 (2002)
- [161] Péter Hantz, Julian Partridge, Győző Láng, Szabolcs Horvát and Mária Ujvári, *Ion-Selective Membranes Involved in Pattern-Forming Processes*, J. Phys. Chem. B. **108**, 18135-18139 (2004)

- [162] Szabolcs Horvát and Peter Hantz, *Pattern Formation Induced by Ion-selective Surfaces: Models and Simulations*, submitted
- [163] Y. Cudennec, A. Lecerf and Y. Gérard, *Synthesis of  $\text{Cu}(\text{OH})_2$  and  $\text{CuO}$  by soft chemistry*, Eur. J. Solid State Inorg. Chem. **32**, 1013-1022 (1995)
- [164] Yannick Cudennec, Amédée Riou, Yves Gérard, André Lecerf, *Hypothèse cristallographique des Mécanismes de formation de  $\text{CuO}_{(s)}$  et de  $\text{Cu}(\text{OH})_{2(2)}$  à partir de  $\text{Na}_2\text{Cu}(\text{OH})_{4(s)}$* , C. R. Acad. Sci. Paris, Série Chimie **3**, 661-666 (2000)
- [165] Y. Cudennec, A. Riou, Y. Gérard, and A. Lecerf, *Synthesis and Crystal Structures of  $\text{Cd}(\text{OH})\text{Cl}$  and  $\text{Cu}(\text{OH})\text{Cl}$  and Relationship to Brucite Type*, J. Solid State Chem. **151**, 308-312 (2000)
- [166] Robert J. Hunter, *Introduction to Modern Colloid Science*, Oxford University Press, Oxford (1993)
- [167] Zsuzsanna Nagy-Ungvárai, Arkad M. Pertsov, Benno Hess and Stefan C. Müller, *Lateral instabilities of a wave front in the Ce-catalyzed Belousov-Zhabotinsky Reaction*, Physica D **61**, 205-212 (1992)
- [168] Zsuzsanna Nagy-Ungvárai, János Ungvárai, and Stefan C. Müller, *Complexity in spiral wave dynamics*, Chaos **3**, 15-19 (1993)
- [169] K. I. Agladze and V. I. Krinsky, *Multi-armed vortices in an active chemical medium*, Nature **296**, 424-426 (1982)
- [170] Gy. Láng, Gy. Inzelt, *An advanced model of the impedance of polymer film electrodes* Electrochim. Acta **44**, 2037-2051 (1999)
- [171] Gy. Láng, M. Ujvári, Gy. Inzelt, *Possible origin of the deviation from the expected impedance response of polymer film electrodes* Electrochim. Acta **46**, 4159-4175 (2001)
- [172] L. Sommer, *Analytical Absorbance Spectrophotometry in Visible and Ultraviolet*, Akadémiai, Budapest (1989)
- [173] M. Traube, Arch. Anat. Physiol. u. Wiss. Med, 87-129 (1867)
- [174] M. F. Pfeffer, *Osmotische Untersuchungen: Studien zur Zell-Mechanik*, 1<sup>st</sup> ed., Engelmann, Leipzig (1877)
- [175] W. Nernst, *Theoretisch Chemie*, 7<sup>th</sup> ed., Ferdinand Encke, Stuttgart (1913)
- [176] Atsuyuki Okabe, Barry Boots, Kokichi Sugihara, Sung Nok Chiu, *Spatial Tessellations: Concepts and Applications of Voronoi Diagrams*, Wiley, Chichester, (1992)



- [177] Ben de Lacy Costello, Andrew Adamatzky, Norman Ratcliffe, Alexey L. Zanin, Andreas W. Liehr, and Hans-Georg Purwins, *The Formation of Voronoi Diagrams in Chemical and Physical Systems: Experimental Findings and Theoretical Models*, Int. J. Bif. Chaos, **14**, 2187-2210 (2004)
- [178] F. Aurenhammer, *Voronoi diagrams – a survey of a fundamental geometric data structure*. Comput. Surv. **23**, 345-405 (1991)
- [179] A. Okabe and A. Suzuki, *Locational optimization problems solved through Voronoi diagrams* Eur. J. Oper. Res. **98**, 445-456 (1997)
- [180] S.C. Müller, T. Mair, O. Steinbock, *Traveling waves in yeast extract and in cultures of Dictyostelium discoideum* Biophys. Chem. **72**, 37-47 (1998)
- [181] M. Tanemura, H. Honda, A. Yoshida, *Distribution of differentiated cells in a cell sheet under the lateral inhibition rule of differentiation* J. Theor. Biol. **153**, 287-300 (1991)
- [182] K.J. Painter in *Mathematical Models for Biological Pattern Formation*, / The IMA Volumes in Mathematics and Applications **121**/ (Eds.: P. K. Maini and H. G. Othmer), Springer, New York **2001**, pp. 59-81.
- [183] D.C. Bottino in *Mathematical Models for Biological Pattern Formation*, / The IMA Volumes in Mathematics and Applications **121**/ (Eds.: P. K. Maini and H. G. Othmer), Springer, New York **2001**, pp. 295-314.
- [184] D. Tolmachiev, A. Adamatzky, *Chemical processor for computation of Voronoi diagram*, Adv. Mater. Opt. Electr. **6**, 191-196 (1996)
- [185] A. Adamatzky, B.P.J de Lacy Costello, *Reaction-diffusion path planning in a hybrid chemical and cellular-automaton processor*, Chaos Soliton Fract. **16**, 727-736 (2003)
- [186] A. Adamatzky, B de Lacy Costello, *Experimental logical gates in a reaction-diffusion medium: The XOR gate and beyond* Phys. Rev. E **66**, 046112 1-6 (2002)
- [187] J. H. Ferziger and M. Peric, *Computational Methods for Fluid Dynamics*, Springer, Berlin (1996)
- [188] Bastien Chopard and Michel Droz, *Cellular Automata Modeling of Physical Systems*, Cambridge University Press, Cambridge (1998)
- [189] L. M. Pismen, M. I. Monine, V. I. Tschernikov, *Patterns and localized structures in a hybrid non-equilibrium Ising model*, Phys. D. **199**, 82-90 (2004)
- [190] Jörg R. Weimar, *Simulation with Cellular Automata*, Logos, Berlin (1997)

- 
- [191] Tibor Erdey-Grúz, *Transport Phenomena in Aqueous Solutions*, Wiley-Akadémiai-Hilger, New York (1974)
- [192] A. A. Kodentsov, M. J. H. van Dal, C. Cserháti, A. M. Gusak and F. J. J. van Loo, *Patterning in Reactive Diffusion*, Defect and Diffusion Forum **194-199**, 1491-1502 (2001)
- [193] K. Binder, *Materials Science and Technology, vol. 5., Phase Transformations in Materials*, (Ed.: P. Haasen), Springer, New York (1990)
- [194] Gert R. Strobl, *The Physics of Polymers*, Springer, Berlin (1997)
- [195] U. Hecht, L. Gránásy, T. Pusztai, B. Böttger, M. Apel, V. Witusiewicz, L. Ratke, J. De Wilde, L. Froyen, D. Camel, B. Drevet, G. Faivre, S.G. Fries, B. Legendre and S. Rex, *Multiphase solidification in multicomponent alloys*, Mater. Sci. Eng. Rev. **46**, 1-49 (2004)
- [196] K. Dálnoki-Veress, J.A. Forrest, J.R. Stevens and J.R. Dutcher, *Morphology of Spincoated Polymer Blend Thin Films*, Physica A **239**, 87-94 (1997)
- [197] S.A. Newman and W.D. Comper, 'Generic' physical mechanisms of morphogenesis and pattern formation, Development **110**, 1-18 (1990)
- [198] P.C. Fife, *Models for phase separation and their mathematics*, Electron. J. Diff. Eqns. **2000**, 1-26 (2000)
- [199] H. Furukawa, *Phase separation by directional quenching and morphological transition*, Physica A **180**, 128-155 (1992)
- [200] B. Liu, H. Zhang and Y. Yang, *Surface enrichment effect on the morphological transitions induced by directional quenching for binary mixtures*, J. Chem. Phys. **113**, 719-727 (2000)
- [201] D. G. Miguez, A. P. Munuzuri, M. Dolnik and L. Kramer, Phys. Rev. Lett., in press
- [202] Péter Hantz and István Biro, *Phase Separation in the Wake of Moving Fronts: Experiments and Simulations*, submitted, cond-mat/0507639 (2005)
- [203] Juha Rantala, *Sol-gel materials for photonic applications*, VTT, Espoo (1998)
- [204] Evgeny Popov and Erwin G. Loewen, *Diffraction Gratings and Applications*, Marcel Dekker, New York (1997)
- [205] Younan Xia, Byron Gates, Yadong Yin, and Yu Lu, *Monodispersed Colloidal Spheres: Old Materials with New Applications*, Adv. Mater. **12**, 693-713 (2000)

The thesis can be found electronically at the website <http://hantz.web.elte.hu>

No part of this thesis may be reprinted or reproduced without permission from the author